Unitarity methods and on-shell particles in scattering amplitudes

ACADEMISCH PROEFSCHRIFT

ter verkrijging van de graad van doctor
aan de Universiteit van Amsterdam
op gezag van de Rector Magnificus
prof. dr. ir. K.I.J. Maex
ten overstaan van een door het College voor Promoties ingestelde
commissie, in het openbaar te verdedigen in de Agnietenkapel
op woensdag 19 oktober 2016, te 12:00 uur

door

Robbert Johannes Rietkerk

geboren te Almere

Promotiecomissie

Promotor	Dhr. Prof. dr. E.L.M.P. Laenen	*Universiteit van Amsterdam*
Copromotor	Dhr. dr. K.J. Larsen	*ETH Zürich*
Overige leden	Dhr. Prof. dr. J. de Boer	*Universiteit van Amsterdam*
	Dhr. dr. S. Frixione	*INFN Genoa*
	Dhr. Prof. dr. ir. P. de Jong	*Universiteit van Amsterdam*
	Dhr. Prof. dr. R.H.P. Kleiss	*Radboud Universiteit Nijmegen*
	Dhr. Prof. dr. B. Nienhuis	*Universiteit van Amsterdam*
	Dhr. dr. J.A.M. Vermaseren	*Nikhef*

Faculteit der Natuurwetenschappen, Wiskunde en Informatica

Titel: Unitarity methods and on-shell particles in scattering amplitudes
ISBN: 978-94-6233-400-7
NUR-code: 925 - Theoretische natuurkunde
Geprint door: Gildeprint Drukkerijen - Enschede
Omslag: Elisa Mariani

Dit werk maakt deel uit van het onderzoekprogramma van de Stichting voor Fundamenteel Onderzoek der Materie (FOM), die deel uitmaakt van de Nederlandse Organisatie voor Wetenschappelijk Onderzoek (NWO). Het promotieonderzoek beschreven in dit proefschrift werd verricht aan het Instituut voor Theoretische Fysica, onderdeel van de Faculteit der Natuurwetenschappen en Informatica aan de Universiteit van Amsterdam, alsmede aan het Nationaal Instituut voor Subatomaire Fysica (Nikhef).

FOM

NWO
Nederlandse Organisatie voor Wetenschappelijk Onderzoek

Nikhef

UNIVERSITEIT VAN AMSTERDAM

C

Contents

L

List of publications

[1] P. Artoisenet, R. Frederix, O. Mattelaer, and R. Rietkerk
Automatic spin-entangled decays of heavy resonances in Monte Carlo simulations
JHEP 03 (2013) 015; arXiv:1212.3460 [hep-ph]
(Chapter 3)

[2] LHC Higgs Cross Section Working Group Collaboration, J. R. Andersen *et al.*
Handbook of LHC Higgs Cross Sections: 3. Higgs Properties
arXiv:1307.1347 [hep-ph]
(Chapter 3)

[3] E. Laenen, K. J. Larsen, and R. Rietkerk
Imaginary parts and discontinuities of Wilson line correlators
Phys. Rev. Lett. 114 no. 18, (2015) 181602; arXiv:1410.5681 [hep-th]
(Chapter 4)

[4] E. Laenen, K. J. Larsen, and R. Rietkerk
Position-space cuts for Wilson line correlators
JHEP 07 (2015) 083; arXiv:1505.02555 [hep-th]
(Chapter 4)

[5] D. Bonocore, E. Laenen, and R. Rietkerk
Unitarity methods for Mellin moments of Drell-Yan cross sections
JHEP 05 (2016) 079; arXiv:1603.05252 [hep-ph]
(Chapter 5)

Chapter 1

Introduction

Research in physics during the last century has led to the remarkable insight that our world is made of a few building blocks, called elementary particles. All these particles are incorporated by the Standard Model of particle physics, along with their interactions through three fundamental forces of nature. Since its inception in the 1970s, the Standard Model has successfully provided accurate quantitative descriptions of many phenomena at particle accelerator experiments. It has also correctly predicted the existence of several particles, the most recent example being the Higgs boson that was discovered in 2012. For these reasons, the Standard Model is a well-established theory of elementary particle physics.

There is, however, evidence that the Standard Model is incomplete. Perhaps the strongest evidence comes from astrophysical and cosmological observations. The phenomenon of solar neutrino oscillations, which mixes their mass and flavour eigenstates, implies that neutrinos cannot be massless particles, as the Standard Model dictates. The observation of the accelerated expansion of the universe and of anomalous galaxy rotation curves furthermore point to the existence of dark energy and dark matter, which are intriguing manifestations of physics beyond the Standard Model (BSM). There are various proposals for extending the Standard Model to incorporate BSM physics, but unfortunately the current level of experimental knowledge is insufficient to draw decisive conclusions about their actual realization in nature.

One of the main purposes of the Large Hadron Collider (LHC) is to improve this situation by performing precision measurements of high-energy particle scattering processes, which may be sensitive to BSM physics. A large fraction of proton-proton scattering events at the LHC are mediated by Standard Model interactions, which constitute a large background to the experimentally indistinguishable signal processes that involve BSM physics. The inference of signal processes can nevertheless proceed on the basis of a statistical analysis, by measuring an excess of events with respect to the predicted frequency of occurrence. This means that a successful interpretation of precision measurements requires accurate predictions of Standard Model contributions to observable quantities in scattering processes, such as cross sections and decay rates.

Perturbative quantum field theory provides a framework for systematically improvable computations of such observables. In this framework observables are constructed from scattering amplitudes, which are expanded as a series in powers of small coupling constants, with the individual orders expressed in terms of increasingly complicated Feynman diagrams. For many processes the leading order and next-to-leading order (NLO) terms in this perturbative expansion have been the state-of-the-art, until more recently their corresponding next-to-next-to-leading order (NNLO) computations have been achieved, in order to reduce the theoretical uncertainty on related observables. Such higher-order amplitudes include the effect of many unobserved particles, whose degrees of freedom must be integrated out. This challenging task can be ameliorated by artificially imposing mass-shell conditions on intermediate particles, a powerful idea that derives from *unitarity*: the basic constraint of total probability conservation.

The role of unitarity in the computation of scattering amplitudes builds on a long history of theoretical developments. The early 1960s witnessed the emergence of a framework for describing strong nuclear interactions, called S-matrix theory. This theory relates initial state particles to final state particles through an abstract scattering matrix, thereby avoiding any reference to unphysical intermediate states [6]. It was hoped that a detailed study of the properties of the scattering matrix, such as analyticity and *unitarity*, would yield enough information to provide a complete description of scattering processes. But this attempt did not turn out to be successful and the theory was ultimately replaced with perturbative Quantum Chromodynamics (QCD). Nevertheless, some of the notions from the old theory could be recycled. In particular unitarity proved useful as a constraint on the analytic structure of amplitudes. Based on Landau's analysis of the singularity structure of Feynman integrals, Cutkosky derived a cutting equation for Feynman diagrams as a natural generalization of unitarity [7, 8]. His cutting equation states that the discontinuity of a Feynman diagram with respect to an external invariant is given by a sum of cut diagrams, which feature *on-shell intermediate particles* according to the Cutkosky cutting rules. A few years later, Veltman showed with a diagrammatic approach that the cutting equation can be derived from causality in the form of the largest-time equation [9]. Thereafter, modified versions of the cutting rules became available for eikonal Feynman diagrams and, more recently, for Feynman diagrams containing unstable particles [10, 11]. Until the late 1980s unitarity was used in conjunction with dispersion relations to obtain results for $2 \to 2$ scattering processes [12]. The first major step to higher particle multiplicities was taken in the 1990s with the computation of one-loop amplitudes for $2 \to n$ processes in supersymmetric Yang-Mills theories [13, 14], based on the requirement of consistency of an ansatz with collinear limits and unitarity.

After the turn of the century the number of applications of unitarity and the development of unitarity-based techniques increased dramatically. It was soon appreciated that replacing any number of intermediate states by on-shell particles probes deeper into the structure of scattering amplitudes. This so-called generalized unitarity approach allowed for the computation of one-loop amplitudes in $\mathcal{N} = 4$ super Yang-Mills theory [15], led to the BCFW-recursion relations for tree-level gluon amplitudes [16, 17], and caused a revolution

in the computation of one-loop QCD amplitudes [18, 19]. Spurred by this success, the attention shifted to the next order(s) in perturbation theory.

Much of the recent progress on multi-loop amplitudes has been made possible by integration-by-parts identities (IBPs) and differential equations for Feynman integrals, both of which received inspiration from unitarity for some part of their development. The IBPs provide linear recursion relations among Feynman integrals [20], which can be solved with the Laporta algorithm in terms of a basis of master integrals [21]. The IBP reduction of real-radiation diagrams (in addition to loop diagrams) is also possible thanks to reverse unitarity cutting rules, introduced in the computation of the NNLO cross section for Higgs boson production through gluon fusion [22]. The master integrals in the result of IBP reductions satisfy differential equations with respect to external invariants [23]. Solving such differential equations benefits greatly from an appropriate choice of master integral basis [24]; unitarity cutting rules play an important role in finding such a basis. Finally, a promising new technique for efficiently generating IBP reductions, based on unitarity cuts of a specific set of subgraphs, was introduced most recently [25]. To conclude, it is fair to say that the notions of unitarity and on-shell cut constraints have been instrumental to many developments in the computation of scattering amplitudes.

Outlook of this thesis

The research contained in this thesis is aimed at developing new applications of unitarity and on-shell particles in scattering amplitudes. The success of unitarity in many computations, as described above, suggests that these further developments can lead to new results for precise theoretical predictions, which are to be confronted with particle collider experiments in order to ascertain the range of validity of the Standard Model and to acquire further insights into BSM physics. I have studied topics for which the actual application of unitarity and related concepts requires the introduction of additional ideas, prescriptions and algorithms. The theoretical tools for scattering amplitudes that resulted are described in this thesis, which is structured as follows.

In the next chapter I provide some necessary background information, where unitarity and cutting equations are discussed in the context of perturbative QCD, with emphasis on their relation to on-shell intermediate particles.

On-shell particles play a key role straight away in chapter 3, which is concerned with the decays of long-lived unstable particles. In this chapter I describe the computer program MadSpin, which employs the narrow-width approximation to generate unstable particles initially on-shell and decays them afterwards in such a way that important spin-correlation effects are accurately described.

Chapter 4 focusses on infrared singularities in scattering amplitudes. This aspect is described by Wilson line correlators, which admit a perturbative expansion in terms of eikonal Feynman diagrams. I introduce the notion of cuts of eikonal diagrams in position space and thereby provide a practical method to extract information from Wilson line correlators.

Turning to scattering amplitudes for the Drell-Yan process in chapter 5, I show how cutting equations provide a tool for obtaining certain cut diagrams from the discontinuity of a forward amplitude. The non-inclusiveness of the Drell-Yan process forms an initial obstacle, which is addressed by two additional prescriptions that form an essential part of the resulting unitarity method.

The last chapter summarizes the results in this thesis and presents the final conclusions. Appendices A and B collect important properties of multiple polylogarithms and harmonic sums, which appear in the result of the calculations in this thesis, and describe a number of powerful tools for manipulating these two classes of functions.

Chapter 2

When particles go on-shell

In this chapter we introduce a number of concepts that play an important role in this thesis. The first concept to be discussed is unitarity, a fundamental property of the scattering matrix. Secondly, the optical theorem is derived from unitarity and it will be shown how this theorem imposes a constraint on scattering amplitudes. Finally, more restrictive relations for scattering amplitudes in perturbation theory are constructed. In particular we give an introduction to cutting equations for Feynman diagrams. This notion relates the discontinuity of a Feynman diagram in a certain variable, usually a Lorentz-invariant dot product of external momenta, to a sum of cut diagrams, which feature on-shell intermediate particles.

2.1. Unitarity of the scattering matrix

Particle scattering processes are defined by specific sets of incoming and outgoing particles (the initial and final states, respectively), and by the interactions among those particles. The interactions are described mathematically in terms of a scattering matrix. The scattering matrix is an operator that transforms a normalized initial state $|a\rangle$ into a final state $S|a\rangle$. The measurement of such a final state is said to yield the result $|b\rangle$ with a probability equal to the squared modulus of a quantum mechanical amplitude,

$$P(a \to b) = |\langle b|S|a\rangle|^2 \,. \tag{2.1}$$

Unitarity of the scattering matrix is a consequence of probability conservation. Taking the probability in eq. (2.1) for an arbitrary initial state $|a\rangle$ and a specific final state $|b\rangle$ and summing over all possible outcomes must give probability one:

$$1 = \sum_b P(a \to b) = \sum_b |\langle b|S|a\rangle|^2 = \sum_b \langle a|S^\dagger|b\rangle\langle b|S|a\rangle = \langle a|S^\dagger S|a\rangle \,. \tag{2.2}$$

Since this must hold for any (normalized) initial state $|a\rangle$, it follows that $S^\dagger S = 1$. Similarly, the condition that a generic final state arises from some particular initial state with unit total probability leads to the condition $SS^\dagger = 1$. Therefore the scattering matrix is unitary.

The great benefit of unitarity is that it constrains the form of particle interactions. After decomposing the scattering matrix into an interaction-free part and an interaction part, conventionally written as $S = 1 + iT$, unitarity of the scattering matrix implies that the transition matrix T obeys the non-linear equation

$$T - T^\dagger = iT^\dagger T \,. \tag{2.3}$$

Roughly speaking, this equation says that the imaginary part of the transition matrix is given by its square. The practical benefit of eq. (2.3) is best demonstrated in the context of scattering amplitudes.

Scattering amplitudes, denoted by $\mathscr{A}$, are proportional to matrix elements of the transition matrix T,

$$\langle b|T|a\rangle = (2\pi)^4\,\delta^4(p_a - p_b)\;\mathscr{A}(a \to b)\,, \tag{2.4}$$

where p_a is the total four-momentum of the initial momentum eigenstate $|a\rangle$ and p_b that of the final state $|b\rangle$. Owing to the extraction of the total momentum conserving delta function, the scattering amplitude $\mathscr{A}(a \to b)$ is a Lorentz invariant function of scalar products of external momenta. From scattering amplitudes one can construct important observables, such as cross sections and decay rates.

Example 2.1. The cross section for two-particle scattering is obtained by dividing the squared amplitude by a flux factor $\Phi_a = 4E_1E_2|v_1 - v_2|$, which depends on the four-momenta of the two particles in the initial state $|a\rangle$, and integrating over the phase space Π_b of the final state[1],

$$\begin{aligned}\sigma(a \to b) &= \frac{1}{\Phi_a}\int \mathrm{d}\Pi_b\;|\mathscr{A}(a \to b)|^2 \\ &\equiv \frac{1}{\Phi_a}\int \frac{\mathrm{d}^3p_1}{(2\pi)^3\,2p_1^0}\cdots\frac{\mathrm{d}^3p_n}{(2\pi)^3\,2p_n^0}\,(2\pi)^4\,\delta^4(p_a - p_b)\;|\mathscr{A}(a \to b)|^2\,,\end{aligned} \tag{2.5}$$

where final state $|b\rangle$ contains n on-shell particles with four-momenta p_i that add up to p_b.

In terms of scattering amplitudes, eq. (2.3) takes the form

$$\mathscr{A}(a \to b) - \mathscr{A}^*(b \to a) = i\sum_X \int \mathrm{d}\Pi_X\;\mathscr{A}^*(b \to X)\mathscr{A}(a \to X)\,, \tag{2.6}$$

where the sum on the right-hand side runs over all intermediate states that are allowed by total momentum conservation, each of which is integrated over the phase space Π_X of the corresponding particles. This equation is interpreted as follows. If the amplitude satisfies $\mathscr{A}(b \to a) = \mathscr{A}(a \to b)$, either due to Lorentz symmetry (e.g. in the case of spinless $2 \to 2$ scattering) or due to invariance under parity and time reversal, then the left-hand side of eq. (2.6) reads $2i\,\mathrm{Im}\,\mathscr{A}(a \to b)$. In general $\mathscr{A}(b \to a)$ is the analytic

[1] The n-particle phase space is a $(3n-1)$-dimensional space spanned by arbitrary four-momenta $p_1,\ldots,p_n$ subject to the constraint of n mass-shell conditions and one total momentum conserving delta function. This leads to the integration measure $\int \frac{d^4p}{(2\pi)^4}\theta(p^0)\,2\pi\,\delta(p^2 - m^2) = \int \frac{d^3p}{(2\pi)^3}\frac{1}{2p^0}$, where $p^0 = \sqrt{\vec{p}^2 + m^2} > 0$.

continuation of $\mathscr{A}(a \to b)$ to the other side of a physical branch cut and the left-hand side becomes $\mathrm{Disc}\,\mathscr{A}(a \to b)$, as explained in ref. [6]. For center-of-mass energies below the threshold for creation of intermediate states, the amplitude has no branch cut discontinuity and the sum over intermediate states X in eq. (2.6) vanishes accordingly. Intermediate states become kinematically allowed as the center-of-mass energy is increased, at which point the amplitude develops a branch cut, whose discontinuity is measured by the right-hand side of eq. (2.6).

Specializing eq. (2.6) to the case of forward scattering yields the optical theorem,

$$2\,\mathrm{Im}\,\mathscr{A}(a \to a) = \sum_X \int \mathrm{d}\Pi_X\, |\mathscr{A}(a \to X)|^2 = \Phi_a\, \sigma(a \to \text{anything})\,, \tag{2.7}$$

which states that the imaginary part of the forward amplitude is proportional to the total cross section for the scattering of an initial state $|a\rangle$. This theorem has been used successfully, for example, in higher-order calculations for deep inelastic scattering, as will be discussed in section 5.1. In general, it is only valid for fully inclusive processes, for which the final state is entirely unspecified (and can thus be anything). The cross section for a non-inclusive process would receive contributions from a subset of the terms in the sum over X in eq. (2.7), which renders the optical theorem inapplicable to a wide range of processes. Nevertheless, the optical theorem provides the inspiration for others tools to compute scattering amplitudes in perturbation theory, which we discuss next.

2.2. Cutting equation for Feynman diagrams

Scattering amplitudes are computed in perturbation theory by approximating them in their perturbative expansion. Each term in such a perturbation series is expressible in terms of Feynman diagrams with a fixed number of interaction vertices corresponding to a given order in perturbation theory. It turns out that any Feynman diagram satisfies a cutting equation, which expresses its discontinuity in terms of cut diagrams featuring on-shell intermediate particles. This statement provides a refinement to the formula in eq. (2.6) for the discontinuity of a scattering amplitude, since the cutting equation holds for individual Feynman diagrams that contribute to an amplitude.

The cutting equation was first obtained by Cutkosky [8] and was later given an elegant alternative derivation by Veltman [9]. Here we follow the latter derivation, which is based on the principle of causality. This principle cannot be incorporated in the momentum-space representation of Feynman diagrams, since the latter involves particles with specified momenta that are necessarily then not localized precisely in spacetime. On the other hand, a causality prescription *can* be formulated in position space, so the following discussion will make use of the position-space representation of Feynman diagrams.

The idea of the cutting equation is to describe the branch cut structure of Feynman diagrams. For the purpose of understanding the analytic structure of Feynman diagrams it will be sufficient to consider massive scalar fields in four spacetime dimensions. The corresponding position-space Feynman propagator is given by

$$\Delta_F(x-y) = \int \frac{\mathrm{d}^4k}{(2\pi)^4} \frac{i}{k^2 - m^2 + i\eta} e^{-ik\cdot(x-y)} , \tag{2.8}$$

which describes the propagation of a particle between spacetime points x and y. The Feynman $+i\eta$ prescription in the denominator of eq. (2.8) ensures that the pole of the integrand at negative (positive) energy is slightly displaced into the upper (lower) half complex k^0-plane. By closing the contour in the complex k^0-plane it can be shown that the Feynman propagator decomposes into positive and negative energy flow,

$$\Delta_F(x) = \theta(x_0)\Delta^+(x) + \theta(-x_0)\Delta^-(x) , \tag{2.9}$$

where x_0 denotes the time-component, $\theta(x)$ is the Heaviside step function and

$$\Delta^\pm(x) = \int \frac{\mathrm{d}^4k}{(2\pi)^3} \theta(\pm k^0)\delta(k^2 - m^2) e^{-ik\cdot x} \tag{2.10}$$

are on-shell propagators with definite energy flow, as indicated by the step functions.

The Feynman propagator decomposition in eq. (2.9) invites the introduction of Feynman rules that will be convenient for incorporating the principle of causality. The rules, which are designed to enforce a particular direction of energy flow, are the following:

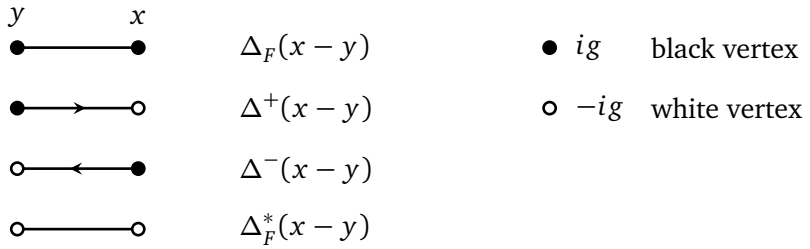

Figure 2.1: Position-space Feynman rules for massive scalar fields.

Ordinary position-space diagrams are described by the first line in fig. 2.1 and consist of black vertices connected by ordinary Feynman propagators. Additional diagrams are generated by changing the colour of (any number of) vertices from black to white, an operation that has the effect of forcing energy flow from black vertices to white vertices. Two white vertices are connected by the complex conjugate propagator, which is given by

$$\Delta_F^*(x) = \theta(x_0)\Delta^-(x) + \theta(-x_0)\Delta^+(x) , \tag{2.11}$$

as derived from the fact that $\Delta^+(x)$ and $\Delta^-(x)$ are each other's complex conjugate.

The Feynman rules in fig. 2.1 are, in a certain sense, degenerate when x and y are time-ordered spacetime points, since causality dictates that positive energy flows forward in time. Suppose that $x_0 > y_0$, then it follows immediately from eqs. (2.9) and (2.11) that $\Delta_F(x-y) = \Delta^+(x-y)$ and $\Delta_F^*(x-y) = \Delta^-(x-y)$. This can be represented diagrammatically in the following way

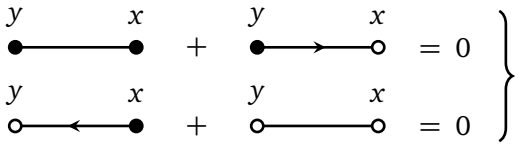

for $x_0 > y_0$, (2.12)

where in eq. (2.12) the vertices are included, so as to provide a relative minus sign that causes the terms to cancel.

The relations in eq. (2.12) immediately generalize to arbitrary graphs in position space: if two graphs differ only by the colour of the vertex with the largest time component, then their sum vanishes. This is called the largest-time equation.

Example 2.2. The largest-time equation for a double-box graph, whose top-left vertex has the largest time component, reads

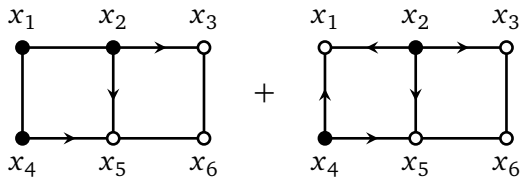

$= 0$ for $(x_1)_0 > (x_2)_0, \ldots, (x_6)_0$. (2.13)

The propagators $\Delta_F(x_1 - x_2)$ and $\Delta_F(x_1 - x_4)$ in the first graph are actually equal to the propagators $\Delta^+(x_1 - x_2)$ and $\Delta^+(x_1 - x_4)$ in the second graph due to the restriction on the time components. Therefore the two graphs are equal, except for a relative minus sign that comes from the difference in colour of the top-left vertex.

The arbitrary restriction in example 2.2, that x_1 has the largest time component, is not generally valid. This can be avoided by summing over all possible vertex colours, such that all terms cancel pairwise (regardless which vertex has the largest time component):

$$\sum_{2^6 \text{ vertex colours}}$$ 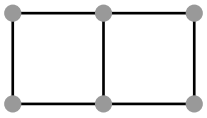 $= 0$, (2.14)

where each grey vertex becomes either black or white in individual terms of the sum. Since this identity places no requirement on the spacetime points, unlike the largest-time equation, it can be "Fourier transformed" to momentum space. After discussing this transformation, we will see how eq. (2.14) leads to the cutting equation.

Position-space graphs contribute to the S-matrix after attaching external sources to (some of) the vertices and integrating over all spacetime points. (Recall that the S-matrix acts on momentum eigenstates, not on position eigenstates.) More precisely, a given position-space graph, denoted by $G(x_1,\dots,x_m)$, contributes to the function

$$F(p_1,\dots,p_n) = \int \left(\prod_{k=1}^{m} d^4x_k\right) G(x_1,\dots,x_m)\, e^{-i\sum_{ij}\alpha_{ij}\, p_i\cdot x_j}\,, \tag{2.15}$$

where the $\alpha_{ij} \in \{-1,0,1\}$ are determined by the graph: $\alpha_{ij} = 1$ for incoming momentum p_i connected to vertex x_j, for outgoing momenta $\alpha_{ij} = -1$ and otherwise $\alpha_{ij} = 0$.

Example 2.3. Consider the position-space graph

$$G(x_1,\dots,x_4) = \Delta_{12}\Delta_{23}\Delta_{34}\Delta_{41} = \quad , \tag{2.16}$$

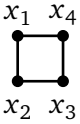

consisting of four spacetime points connected in a square by propagators $\Delta_{ij} \equiv \Delta_F(x_i - x_j)$. Attaching external sources with outgoing momenta $p_1,\dots,p_4$ to its four corners and integrating over all spacetime points $x_1,\dots,x_4$ yields the one-loop box diagram in momentum-space:

$$\int \left(\prod_{k=1}^{4} d^4x_k\right) G(x_1,\dots,x_4)\, e^{i\sum_j p_j\cdot x_j} = (2\pi)^4\,\delta^4\Big(\textstyle\sum_j p_j\Big) \quad . \tag{2.17}$$

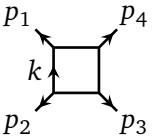

The box diagram on the right-hand side represents the following one-loop Feynman integral

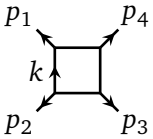

$$= g^4 \int \frac{\mathrm{d}^4k}{(2\pi)^4} \frac{1}{D(k)\,D(k+p_2)\,D(k+p_2+p_3)\,D(k+p_2+p_3+p_4)}\,, \tag{2.18}$$

where $D(k) = k^2 - m^2 + i\eta$.

While the function $F(p_1,\dots,p_n)$ defined in eq. (2.15) contributes directly to the S-matrix, a Feynman diagram (obtained by factoring out $i(2\pi)^4$ and a total momentum conserving delta function) contributes to the corresponding scattering amplitude, see eq. (2.4). A generic L-loop Feynman diagram with N propagators takes the form

$$\mathscr{F}(p_1,\dots,p_n) = g^m \int \left(\prod_{i=1}^{L} \mathrm{d}^4k_i\right) \frac{\mathscr{N}\big(\{p_i\},\{k_i\}\big)}{\prod_{j=1}^{N}\big(q_j^2 - m_j^2 + i\eta\big)}\,, \tag{2.19}$$

where the momenta q_j are particular linear combinations of loop momenta k_i and external momenta p_i depending on the graph. A numerator function $\mathscr{N}$ has also been included, which is always polynomial of scalar products of loop momenta and external momenta.

The identity for position-space graphs in eq. (2.14) can be transformed to momentum space, which thereby becomes an equation for Feynman diagrams. Inspection of eq. (2.14) reveals two particular terms in the sum: the original graph (only black vertices) and its complex

conjugate (only white vertices); their sum gives twice the real part of the original graph. All other graphs have at least one propagator with a forced direction of energy flow and some of them will vanish due to conflicting energy constraints. The remaining non-vanishing graphs are divided into two regions by the set of black vertices and the set of white vertices. This is illustrated in the following example.

Example 2.4. Consider the two individual graphs in example 2.2. If sources are attached to their four corners in such a way that energy comes in on the left and flows out on the right (as indicated by the arrows on the external lines), then the diagram with two connected regions of like-coloured vertices is (generally) non-vanishing, while the other diagram is immediately zero:

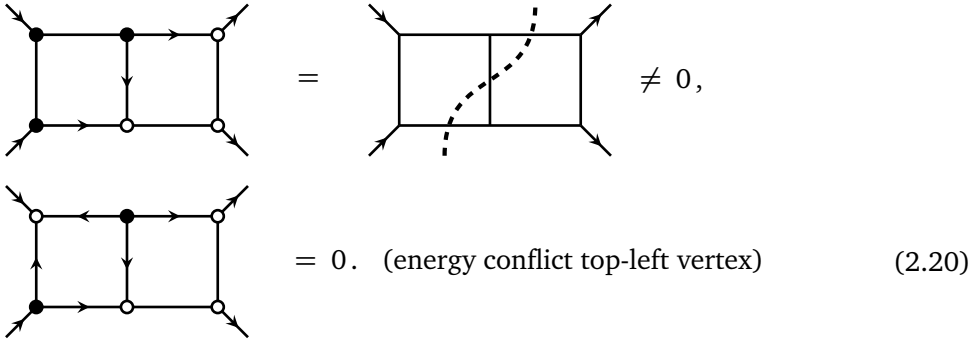

$$= \qquad \neq 0\,,$$

$$= 0\,. \quad \text{(energy conflict top-left vertex)} \tag{2.20}$$

The dashed line is a convenient diagrammatic notation for indicating the separation between the black and white vertices and turns the graph into a cut diagram.

From this example it is clear that cut diagrams are obtained from the original diagram by replacing cut Feynman propagators with $\Delta^{\pm}(x)$. Comparing the formulas for Δ_F and $\Delta^{\pm}$ in eqs. (2.8) and (2.10) it is evident that the cutting rule amounts to

$$\frac{i}{k^2 - m^2 + i\eta} \quad \longrightarrow \quad 2\pi\,\theta(\pm k_0)\,\delta(k^2 - m^2)\,, \tag{2.21}$$

where the sign on the right-hand side is chosen such that energy flows across the cut in the direction that is compatible with the external sources. The real part of the original position-space graph becomes the imaginary part, or more generally the discontinuity, of the Feynman diagram. We thus arrive at the cutting equation

$$\mathrm{Disc}\,\mathscr{F} = \sum_k \mathrm{Cut}_k\,\mathscr{F}\,, \tag{2.22}$$

where the operator Cut_k has the effect of setting a number of (suitably labeled) propagators on-shell, according to the Cutkosky cutting rule:

$$\mathrm{Cut}_k\,\mathscr{F} = \int \left(\prod_{i=1}^{L} \mathrm{d}^4 k_i\right) \frac{\mathscr{N}\big(\{p_i\},\{k_i\}\big) \prod_{j=1}^{r} (-2\pi i)\,\theta((q_j)_0)\,\delta\big(q_j^2 - m_j^2\big)}{\prod_{j=r+1}^{N} \big(q_j^2 - m_j^2 + i\eta\big)}\,. \tag{2.23}$$

The cutting equation shows exactly how the discontinuity of a Feynman diagram is the result when internal particles go on-shell.

The theory described in this chapter will come back in a number of places in this thesis. In chapter 3 we encounter on-shell intermediate particles, which factorize the decay of unstable, narrow resonances from their production. This is based on the narrow-width approximation,

$$\frac{1}{\left(p^2-m^2\right)^2+m^2\Gamma^2} \xrightarrow{\Gamma/m\to 0} \frac{\pi}{m\Gamma}\delta(p^2-m^2)\,, \tag{2.24}$$

which is applied to squared amplitudes in the computation of the cross section; hence the squared propagator on the left-hand side of eq. (2.24). In chapter 4, cutting equations are constructed for Feynman diagrams with soft gauge bosons (eikonal diagrams). And finally, in chapter 5 we study how the left-hand side of the cutting equation in eq. (5.11) can be modified in such a way that the corresponding subset of cut diagrams all contribute to a particular cross section.

Chapter 3

On-shell or off-shell? Decaying unstable particles

The study of unstable particles plays an important role in the analysis of scattering processes at the Large Hadron Collider (LHC). Many particles in the Standard Model are short-lived and decay into lighter particles before they can reach particle detectors. There are also various beyond the Standard Model (BSM) theories that propose the existence of new heavy particles, which ultimately decay into known ones and cannot themselves be detected directly. However, even though these unstable particles are not experimentally accessible, a great deal can be learned by studying their decay products.

The description of scattering processes in full detail, with inclusion of all decay products, is a formidable task for theorists due to the large number of particles in the final state. The latter increases the complexity of scattering amplitudes tremendously, both through the growth of the number of Feynman diagrams and through the large number of scales on which the results can depend. From the theoretical point of view one often describes reactions of undecayed particles and then treats decays separately.

In many cases such theoretical simplification is warranted. While stable particles are exactly on their mass-shell, unstable particles have the freedom to be off-shell, by an amount characterized by the decay width Γ. Unstable particles whose width is very small compared to their mass will typically be near their mass-shell. Putting such particles exactly on-shell, which is what unitarity cuts do, allows one to treat them as stable particles. This so-called narrow-width approximation, which dates back to the 1960s [26], greatly simplifies calculations of scattering amplitudes involving unstable particles.

Fixed order descriptions of scattering amplitudes often make use of the narrow-width approximation. Nowadays, theoretical descriptions take the form of fully automated Monte Carlo event generators, which serve as indispensable tools for comparing theory and experiment. Their high level of automation calls for an equally automated application of the narrow-width approximation, providing the opportunity to generate predictions for an unprecedented variety of processes. This is the main motivation for the work presented in

this chapter, which is implemented in the program MADSPIN for automated decays of narrow resonances (i.e. unstable particles with a small width-to-mass ratio) in a Monte Carlo generator.

3.1. The narrow-width approximation for unstable particles

In scattering processes involving unstable particles, the narrow-width approximation can provide a useful simplification in the calculation of corresponding cross sections. In a generic process, two initial-state particles i_1 and i_2 collide to produce a number of stable particles $s_1, \ldots, s_\ell$ and unstable particles $u_1, \ldots, u_p$. Each unstable particle u_k subsequently decays into several (n_k) decay products $d_{i,k}$. In this notation, the production and decay of unstable particles may be written as [27]

$$\begin{aligned} i_1 + i_2 \longrightarrow\ & s_1 + \cdots + s_l + Q_0 + u_1(\to d_{1,1} + \cdots + d_{1,n_1} + Q_1) \\ & + \cdots \\ & + u_p(\to d_{p,1} + \cdots + d_{p,n_p} + Q_p)\,, \end{aligned} \tag{3.1}$$

where the Q_i are sets of particles that represent (optional) radiation, which starts to appear at next-to-leading order (NLO) in perturbation theory.

This is an intuitive picture of processes with unstable particles, but it is incomplete. The reason is that eq. (3.1) only receives contributions from *resonant* Feynman diagrams, which are those diagrams that contain divergences at points in the final-state phase space where an unstable particle u_k goes on-shell. Restricting oneself to such a subset of resonant diagrams generally spoils gauge invariance, due to the missing interference with *non-resonant* diagrams [28,29]. The latter have the same final state as the resonant diagrams, but do not have the phase-space divergences related to the unstable particles. Instead, both resonant and non-resonant diagrams are included in the full process

$$i_1 + i_2 \longrightarrow s_1 + \cdots + s_l + (d_{1,1} + \cdots + d_{1,n_1}) + \cdots + (d_{p,1} + \cdots + d_{p,n_p}) + \bigcup_{i=0}^{p} Q_i\,, \tag{3.2}$$

But the total set of contributions to eq. (3.2) can be very large, so that computing QCD corrections to this full process is often beyond the reach of current capabilities. This is the case for many $2 \to 6, 7, 8, \ldots$ processes of interest [30], such as the fully decayed $t\bar{t}H$ process, for example (see section 3.4).

The narrow-width approximation provides a formal way out of this stand-off between feasibility and completeness. In the limit of vanishing width, $\Gamma_{u_k}/m_{u_k} \to 0$, the unstable particles do not decay rapidly but live longer than the timescale of the hard interaction. This means that the production and the decay of the unstable particles are well separated in spacetime, so that quantum interference between radiative corrections coming from the two regions

is strongly suppressed. Thus, the narrow-width approximation treats the production and decay separately,

$$i_1 + i_2 \longrightarrow s_1 + \cdots + s_l + Q_0 + u_1 + \cdots + u_p \,, \tag{3.3}$$

$$u_k \longrightarrow d_{k,1} + \cdots + d_{k,n_k} + Q_k \,, \quad \text{for } k = 1, \ldots p \,, \tag{3.4}$$

technically speaking, due to factorization at the level of squared amplitudes. The narrow-width approximation reduces the computational complexity of scattering cross sections at the modest expense of ignoring correction terms which are suppressed by a factor of order $\mathcal{O}(\Gamma/m)$. Gauge invariance is restored up to the same level of precision.

Example 3.1. The tree-level amplitude $\mathscr{A}_{\text{tree}}$ for a process involving the semileptonic decay of a top quark, $ij \to (t \to b\,\ell^+\nu_\ell)X$, may be written as

$$\mathscr{A}_{tree} = \mathscr{A}(ij \to tX)\, \frac{i(\not{p} + m_t)}{p^2 - m_t^2 + i m_t \Gamma_t}\, \mathscr{A}(t \to b\,\ell^+\nu_\ell) \,. \tag{3.5}$$

To compute the cross section, one needs to square the amplitude $|\mathscr{A}_{tree}|^2$ and integrate it over the phase space of the final-state particles. This computation is much easier in the limit $\Gamma_t/m_t \to 0$. In this approximation the squared amplitude can be simplified by making the replacement

$$\frac{1}{\left(p^2 - m_t^2\right)^2 + m_t^2\Gamma_t^2} \xrightarrow{\Gamma_t/m_t \to 0} \frac{\pi}{m_t \Gamma_t} \delta(p^2 - m_t^2) \,. \tag{3.6}$$

The Breit-Wigner distribution on the left-hand side (see fig. 3.1), which originates from the squared top quark propagator, is replaced by the on-shell Dirac delta distribution on the right-hand side. As a result of the replacement in eq. (3.6), the production of the top quark is separated from its decay.

The accuracy of the narrow-width approximation depends primarily on the properties of the unstable particles under consideration. The narrow-width approximation is well-suited to a number of particles in the Standard Model, including the Higgs boson, the top quark and

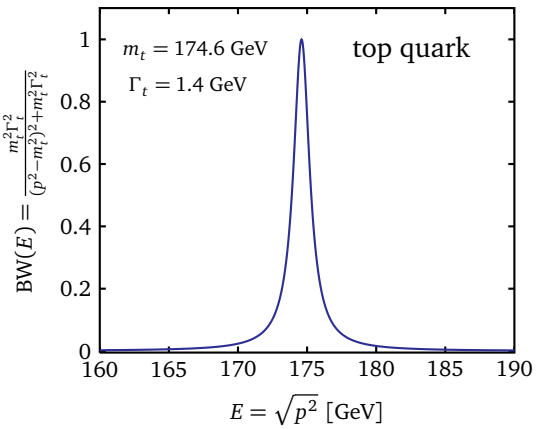

Figure 3.1: The top quark Breit-Wigner distribution, normalized to unit maximum value. In the narrow-width approximation, this distribution is replaced by a Dirac delta distribution.

Particle	Decay width Γ	Mass m	Γ/m
Higgs boson	3.7 MeV	125.09 ± 0.24 GeV	$3.2 \cdot 10^{-5}$
Top quark	$1.41^{+0.19}_{-0.15}$ GeV	174.6 ± 1.9 GeV	$8.1 \cdot 10^{-3}$
$W^{\pm}$ boson	2.085 ± 0.042 GeV	80.385 ± 0.015 GeV	$2.6 \cdot 10^{-2}$
Z boson	2.4952 ± 0.0023 GeV	91.1876 ± 0.0021 GeV	$2.7 \cdot 10^{-2}$

Table 3.1: Standard Model particles with a small width Γ compared to their mass m, so that they may be treated in the narrow-width approximation. Data taken from [32]. The quoted value for the Higgs boson width is the Standard Model prediction; the experimentally determined upper bound is about 2.6 GeV.

the electroweak vector bosons. For these particles, the ratio Γ/m is indeed a small parameter, see table 3.1. Extensions of the Standard Model may also feature narrow resonances, whose decay width can be calculated given some values for the parameters in a specific model. For benchmark parameters SPS1a [31], the Minimal Supersymmetric Standard Model (MSSM) contains several particles whose ratio Γ/m is below one percent, including the gluino, stops, neutralinos and heavy Higgs bosons. The narrow-width approximation is therefore a good approximation for a variety of particles.

However, the validity of the narrow-width approximation should not be taken for granted for all observables. In some cases there can be large contributions from phase-space regions where unstable particles are far off-shell [33,34]. The approximation may also break down for specific observables that are sensitive to non-resonant diagrams [34, 35]. But besides these relatively minor exceptions, there is a potentially more serious consequence for Monte Carlo events, depending on the way they are generated. An accurate method is to generate the decayed events at once, according to squared amplitudes which are first simplified in narrow-width approximation and then treated as spin-density matrix elements [36]. A less accurate, but very efficient, method is to generate the production events first and to decay the unstable particles in a separate stage. The latter method is already often implemented, but such that it loses information about the spin states of the unstable particles and thereby washes away so-called spin-correlation effects. How to remedy this is discussed in the next section.

3.2. Retaining spin-correlation effects in QCD processes

Spin is an important property of (B)SM particles and it should be taken into account as best as possible in theoretical descriptions. Indeed, spin correlations have an important impact on differential cross sections.

Example 3.2. The semileptonic decay of the top quark, $t \to \ell^+ \nu_\ell b$, features a prototypical example of a spin correlation. The angular distribution of the decay products are correlated with the top quark spin [37], according to

$$\frac{1}{\Gamma_t}\frac{d\Gamma}{d\cos\phi_i} = \frac{1+a_i\cos\phi_i}{2}\,, \tag{3.7}$$

where ϕ_i is the angle between the direction of flight of decay product $i = \ell^+, \nu_\ell, b$ and the top quark spin axis. The coefficients a_i describe the amount of spin correlation, with $|a_i| = 1$ indicating 100% correlation. To leading order these values are $a_{\ell^+} = 1.0$, $a_\nu = -0.31$ and $a_b = -0.41$ (with small QCD corrections [38]). Clearly, the direction of the lepton is particularly sensitive to the spin of the top quark.

For generic processes, represented by eq. (3.2), one may distinguish two types of spin correlation. A process is said to contain *decay spin correlations* if there are correlations among two decay products $d_{i,k}$ and $d_{j,k}$ coming from the same unstable particle u_k. This shows up as a non-trivial dependence of the scattering matrix on the dot product of their four-momenta $d_{i,k} \cdot d_{j,k}$, where the particle labels are also used to denote the corresponding four-momenta. In a similar fashion, *production spin correlations* connect a decay product $d_{i,k}$ to either the decay product $d_{j,k'}$ of another parent ($k' \neq k$), a stable particle s_j, an initial-state particle $i_{1,2}$, or QCD radiation Q_0.

Spin correlations can provide interesting insights into hard scattering processes. They can be used to study details of the top quark interactions and can sometimes help to distinguish different production mechanisms [39]. Spin correlations have also played a role in discriminating signal from background in the context of the Higgs boson discovery [40] and in searches for physics beyond the Standard Model [41], making it important to describe them accurately. However, in modern-day next-to-leading order Monte Carlo event generators which produce events first and perform the decays in a separate step, spin correlations are invariably ignored. The aim is to repair this.

The first step towards resolving this mismatch is the observation that spin correlations are already present at tree level, see example 3.2. An intermediate solution would be to generate first events at next-to-leading order accuracy without spin correlations and then to re-weight them in such a way as to include tree-level spin-correlation effects. In the re-weighting stage the tree-level differential cross section is evaluated for each final-state kinematical configuration both with and without spin correlations, yielding from the ratio of these two evaluations a re-weighting factor for each event that takes spin correlations into account. The resulting weighted events are not directly comparable with experiment,

because experimental events always have unit weight. So one must un-weight the generated events. If one knows the maximum weight, then a simple unweighting procedure can be performed: keep an event if its weight is larger than a random fraction of the maximum weight,

$$W_{\text{event}} > r \cdot W_{\text{max}} \quad \text{for } r \in [0,1] \,, \tag{3.8}$$

otherwise discard the event. This solution, resting on the standard Von Neumann acceptance-rejection method, was proposed in [42], where it was shown that the maximum weight is expressible as a product of the differential cross section for the production process multiplied by a constant factor that depends only on the decay,

$$W_{\text{max}} = \frac{d\sigma_{\text{prod}}}{d\Phi_{\text{prod}}} \times C_{\text{decay}} \,, \tag{3.9}$$

and where analytic formulae for the constants C_{decay} associated to the decay of the top quark and the electroweak vector bosons were provided. This approach has furthermore been implemented successfully in the programs MC@NLO [43, 44] and POWHEG [45, 46], about ten years ago.

Since then, fully automated next-to-leading order event generators [47–49] have been introduced, which are not limited to a specific set of processes. For example, MC@NLO has been upgraded to the automated version aMC@NLO [50] and further expanded into the framework MadGraph5_aMC@NLO [27]. This high level of automation has called for an equally automatic implementation of the narrow-width approximation and of spin correlations.

3.3. Implementation of spin-correlated decays in the program `MadSpin`

The decay of narrow resonances in Monte Carlo events can be performed by means of the highly automated program MadSpin, which we presented in ref. [1]. This program is embedded in the MadGraph5_aMC@NLO framework, such that it can be applied to processes in any theoretical model whose matrix elements can be evaluated with MadGraph [51, 52]. The implementation of MadSpin supersedes that of particle decays in MC@NLO and goes beyond the capabilities of other programs, such as BRIDGE [53] or the generic decay routines in PYTHIA [54, 55] and HERWIG [56].

The algorithm used in MadSpin is based on the solution proposed in ref. [42], as described in the previous section. Four steps are taken in MadSpin in order to decay narrow resonances and to retain spin-correlation effects.

Algorithm 3.3. *Spin-correlated decay of unstable particles with* MADSPIN.

1. Generate the production event. *An event for the production process in eq.* (3.3) *is generated at next-to-leading order accuracy with all particles on-shell, including the unstable ones.*

2. Decay the unstable particles. *Each unstable particle is put off-shell by choosing a random value for its invariant mass with a probability proportional to the Breit-Wigner distribution (see fig. 3.1). The decay products are generated according to a uniform distribution in the rest frame of their parent particle.*

3. Reshuffle momenta in production event. *The altered invariant mass of the unstable particles calls for modification of their four-momenta, which is done in such a way that energy and momentum remain conserved.*

4. Unweight the decayed event. *The tree-level differential cross section for the full process in eq.* (3.2) *is evaluated at the phase-space point corresponding to the decayed event. The unweighting procedure in eq.* (3.8) *is applied and if the event is discarded, then the decay is generated again (step 2).*

The reshuffling traditionally requires a bit of manual guidance in order to preserve the characteristics of production events, in particular when there are particles close to resonance. In MADSPIN this task is fully automated through the use of a so-called single-diagram-enhanced multichannel integration procedure in MADEVENT [57]. This procedure helps to identify variables that are in one-to-one correspondence with possible resonant propagators and to keep those variables unchanged during the reshuffling process.

The unweighting procedure requires the knowledge of the maximum weight in eq. (3.9), as a product of the differential production cross section and a decay-dependent constant. It is sheer impossible to derive formulae for the latter constants for arbitrary theories, so that an analytic approach to this is in conflict with the automation of the implementation. In MADSPIN these constants are therefore obtained numerically. How to do this in an efficient manner is described in more detail below.

3.3.1. Determination of maximum weight

The simplest way to obtain a numerical estimate of the constants C_{decay} in the maximum weight is to probe the phase space of the decay of the first production event, which is assumed to be representative for all events, at a large number of phase-space points. The largest value of the differential cross section for the decayed process at all these phase-space points, divided by the differential cross section for the production process, provides an (under)estimate of C_{decay}. However, such a simple estimate has several drawbacks. It fails to account for finite width corrections to the formula in eq. (3.9), which depend on the phase space of the production event. It also suffers from large statistical uncertainties between different runs of MADSPIN due to the sampling of a finite number of phase-space

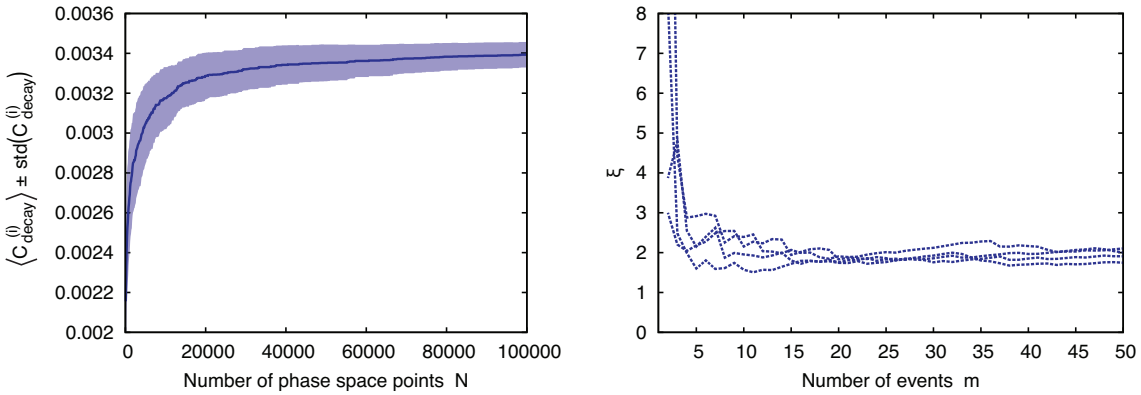

Figure 3.2: Analysis of $pp \to W$ events used for the calibration of parameters (N, m, ξ). Left pane: the average $\langle C^{(i)}_{\text{decay}} \rangle$ over $m = 100$ production events becomes constant for a large number of phase-space points N. Notice that the standard deviation remains nonzero, reflecting the presence of finite-width corrections. Right pane: the parameter ξ becomes constant as a function of the number of production events for 20k phase-space points. Different curves are associated with different sets of production events.

points. Finally, making an underestimate of the maximum weight has an undesired impact on differential cross sections as it leads to automatic acceptance of events with a larger weight, whose spin-correlation effects are therefore not properly taken into account.

The prescription that we implemented is slightly more elaborate in order to deal with these issues. First the estimates $C^{(1)}_{\text{decay}}, \ldots, C^{(m)}_{\text{decay}}$ are extracted from the first m production events, using N phase-space points for each event. An estimate for the constant C_{decay} in the maximum weight is then expressed as

$$C^{\text{est.}}_{\text{decay}} = \left\langle C^{(i)}_{\text{decay}} \right\rangle + \xi \, \text{std} \left(C^{(i)}_{\text{decay}} \right) , \tag{3.10}$$

where the average and standard deviation are both taken over the set of m events.

This prescription contains three adjustable parameters: the number of phase-space points N associated with the decay, the number of production events m, and the number ξ of standard deviations added to the average in eq. (3.10). These parameters are chosen such that the resulting $C^{\text{est.}}_{\text{decay}}$ is as close as possible to (but also strictly larger than) the true value C_{decay} in order to optimize the efficiency of the unweighting procedure. The values of these parameters are calibrated on processes for which an analytical expression for the constant is known. Empirical studies involving different processes verified that the same calibration can be used for all those processes.

The calibration of the three parameters N, m and ξ, is based on an analysis of W-production events and goes a follows (see fig. 3.2). First, for each of a large number (of order 100) of production events, the number of phase-space points N is increased until the average $\langle C^{(i)}_{\text{decay}} \rangle$ of the decay constants becomes independent of N. This determines the number of phase-space points to be used. Next, the true value C_{decay} is extracted from an analytic formula (or by considering an even much larger number of production events). Requiring

that the right-hand side of eq. (3.10) reproduces this true value allows us to extract the parameters ξ and m. The value of ξ will be large for a small number of events and will settle to a constant value as m increases. The point where this happens determines these two remaining parameters. The first version of MadSpin used the conservative values ($N = 10^4$, $m = 20$, $\xi = 4$), which was later optimized to ($N = 400$, $m = 75$, $\xi = 4$) for increased performance [27].

3.3.2. Validation of the method and implementation

The efficiency and flexibility of MadSpin comes at the cost of a possible loss of two desired effects. The first possibility is that finite-width effects may be lost in the distributions of events, due to the narrow-width approximation that is at the heart of the method. The second possibility is that spin-correlation effects may not be included with enough accuracy, since the unweighting procedure uses only tree-level information. We have performed detailed studies in order to assess to what extent these effects are retained. Apart from a few isolated cases, where the inherent approximations are expected to break down, these studies revealed the method to be working remarkably well.

Finite-width effects

The extent to which finite-width effects are retained by MadSpin has been tested for a large class of processes involving narrow resonances. This was done by comparing decayed events generated with MadSpin, to decayed events generated with an exact reference method (in this case MadGraph, using a finite width for narrow resonances at all stages of the generation and including non-resonant contributions). The outcome of this comparison is that a large number of differential cross sections (with respect to transverse momenta, angular separations and invariant masses) display excellent agreement between MadSpin and the reference method.

Nevertheless, also some differences were observed, in particular around thresholds and in the tail of resonant invariant-mass distributions. The largest deviations were found in diboson production at the LHC in the channel $pp \to ZW^+ \to \mu^+\mu^- e^+\nu_e$ (see fig. 3.3). For this process MadSpin was used to decay both vector bosons and compared to the reference method that generates the final state $\mu^+\mu^- e^+\nu_e$ directly and includes non-resonant diagrams. In this case the cut $m(\mu^+,\mu^-) > 40$ GeV was imposed. The result is that MadSpin fails to reproduce the correct distribution of events far below the resonance region, $m(\mu^+,\mu^-) \ll m_Z$. This behaviour is expected, because of the non-resonant diagrams involving the photon splitting $\gamma^* \to \mu^+\mu^-$ which contribute strongly in this region. Considering that without the reshuffling procedure MadSpin would produce only a narrow peak at $m(\mu^+,\mu^-) = m_Z$, it actually reproduces the correct behaviour close to the resonance peak rather well. A good agreement was also seen in the distribution of events with

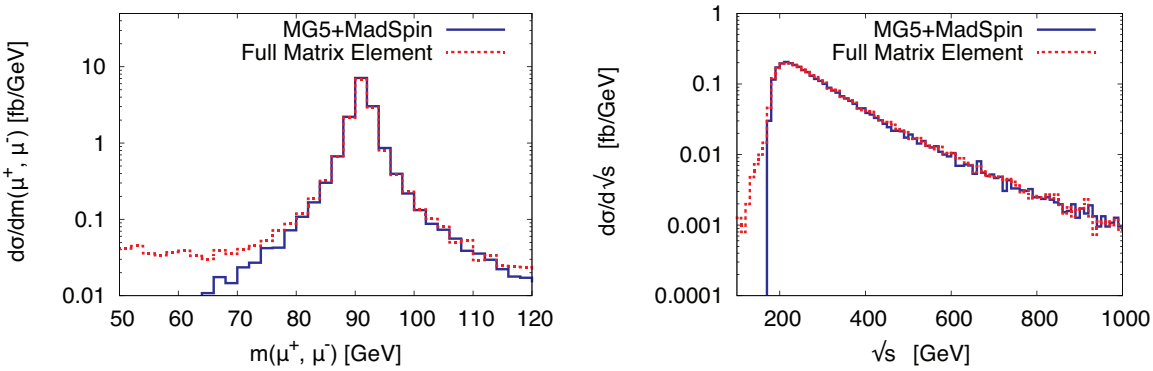

Figure 3.3: Distribution of events with respect to the invariant mass of the muon pair (left) and with respect to the center-of-mass energy (right) in $pp \to ZW^+ \to \mu^+\mu^- e^+\nu_e$. These distributions show the largest observed deviations between MadSpin (solid line) and the exact reference method (dashed line), which occur far below from the resonance region $m(\mu^+,\mu^-) \ll m_Z$ (left) and below threshold $\sqrt{s} < m_Z + m_W$ (right).

respect to the invariant mass of the colliding partons $\sqrt{s}$, except below the threshold region, $\sqrt{s} < m_Z + m_W$, where the finite-width effects of the vector bosons are of primary importance and cannot be reproduced in the narrow-width approximation.

Spin-correlation effects

To check that spin-correlation effects are taken into account with sufficient accuracy in MadSpin, we studied spin-sensitive distributions of specific processes for which more accurate predictions by other Monte Carlo generators are available. Specifically, our predictions for top quark pair production and single-top production are compared against MCFM [58–60], which includes all spin correlations at next-to-leading order for these processes. As a minor limitation on the comparison, MCFM provides only fixed-order predictions, whereas MadSpin is embedded in a scheme involving fixed-order calculations matched to parton shower.

The events have been generated using the following set of input parameters. The production of both processes was simulated at the LHC with $\sqrt{s} = 8$ TeV, with masses $m_t = 172.5$ GeV and $m_b = 4.75$ GeV and semileptonic decay of each top quark. For single-top we used the four-flavour scheme and considered production via the t-channel [61]. The parton-distribution functions for $t\bar{t}$ production were taken from MSTW2008nlo68cl (v5.7), with $\alpha_S(M_Z) = 0.12018$ and two-loop running [62]. For single-top we used the set MSTW2008nlo68cl_nf4 (v5.8.4) with $\alpha_S(M_Z) = 0.11490$ [63]. The renormalization and factorization scales have been set to the same value μ, equal to the average of the t and $\bar{t}$ transverse masses in the case of $t\bar{t}$ production, and equal to four times the b transverse mass in single-top production [64]. Jets were reconstructed by means of the anti-k_T algorithm [65], with $R_{\text{cut}} = 0.4$ and $(p_T)_{\text{min}} = 25$ GeV. Events generated by MadSpin were showered and hadronized with the program HERWIG.

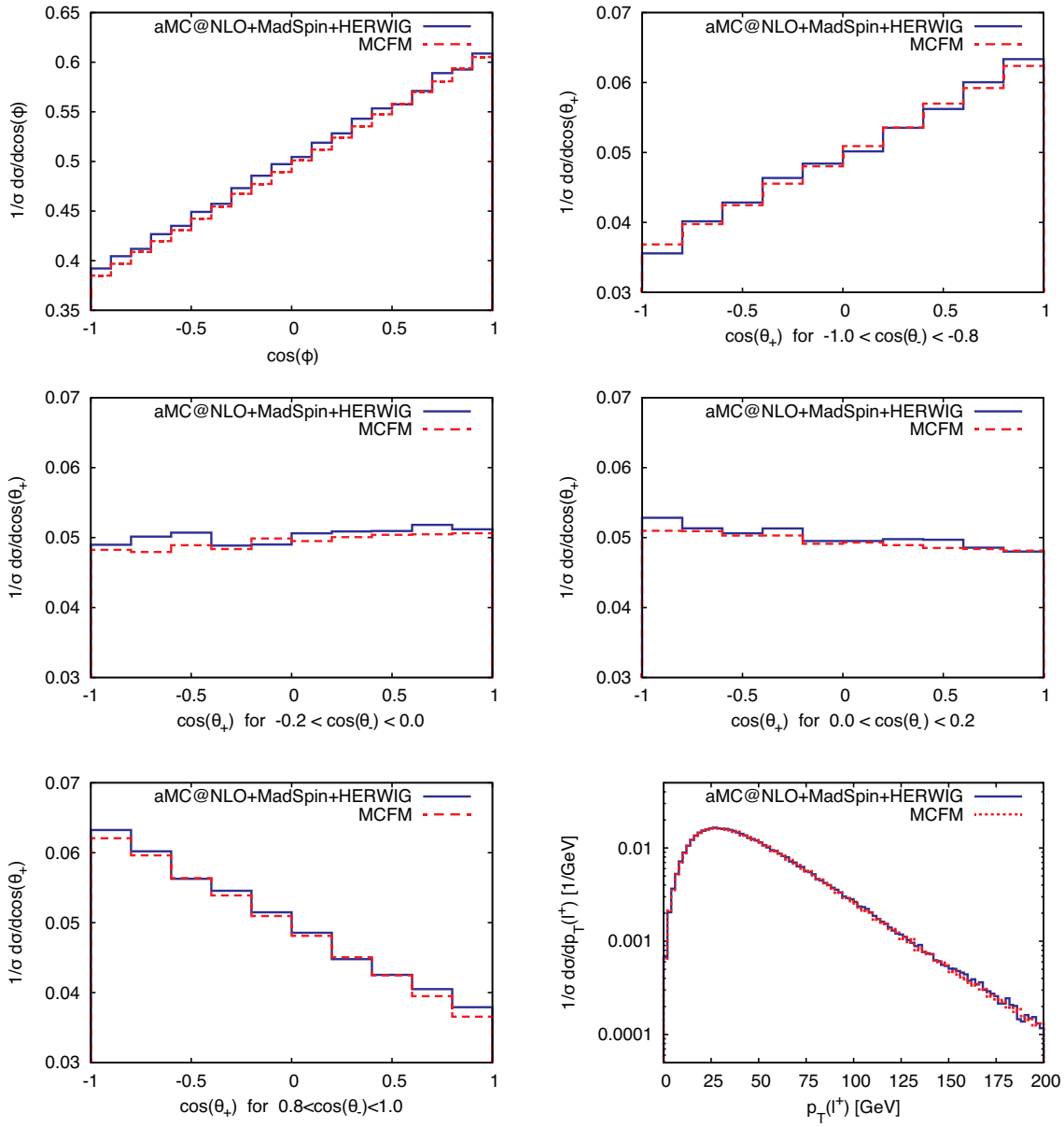

Figure 3.4: Cross sections differential in $\cos(\phi)$, $\cos(\theta_+)$ and $p_T(l^+)$ for $pp \to t\bar{t}$ events in the dileptonic decay channel. These distributions show that MadSpin reproduces the correct behaviour with respect to observables that are particularly sensitive to spin correlations.

Using the generated events, we studied observables that are particularly sensitive to spin correlations. For top quark pair production, good observables are $\cos(\phi)$ and $\cos(\theta_\pm)$, where ϕ is the angle between the direction of flight of l^+ in the t rest frame and the direction of flight of l^- in the $\bar{t}$ rest frame, θ_+ is the angle between the direction of flight of l^+ in the t rest frame and the positive beam direction and θ_- is the angle between the direction of flight of l^- in the $\bar{t}$ rest frame and the positive beam direction [66]. For t-channel single-top production, the observable that is most sensitive to spin-correlation effects is $\cos(\theta)$, where θ is defined in the top quark rest frame as the angle between the directions of flight of l^+ and the hardest non-b-tagged jet [67]. The results for differential

cross sections as a function of these observables obtained with MadSpin were found to be in agreement with those generated by MCFM (see figs. 3.4 and 3.5).

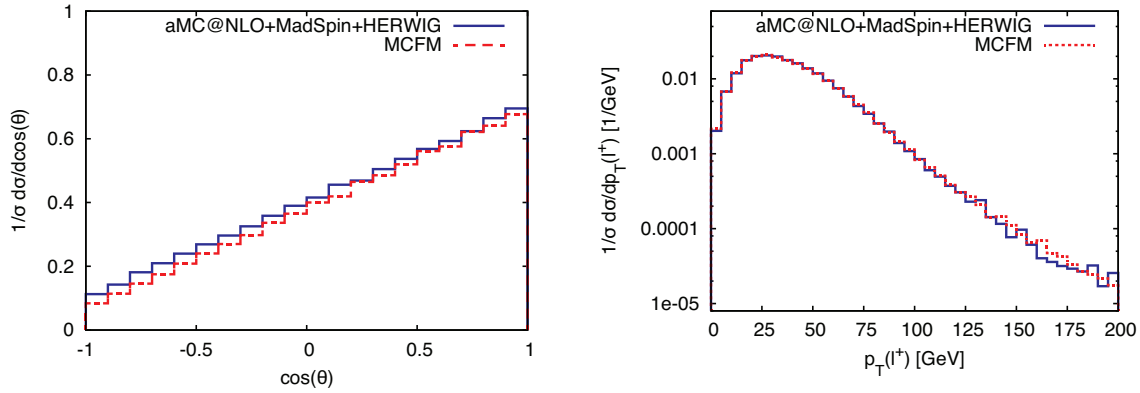

Figure 3.5: Cross sections differential in $\cos(\theta)$ and $p_T(l^+)$ for t-channel single-top production in the four flavour scheme, where θ is the angle between the directions of flight of l^+ and the hardest non-b-tagged jet in the top quark rest frame. The slight difference in normalisation of the two curves in the left plot is due to the definition of the observable: in the aMC@NLO + MadSpin + HERWIG predictions there are slightly more events with a non-b-tagged jet compared to the fixed-order results of MCFM (80% versus 76%, respectively).

3.4. Application to Higgs boson and top-quark pair production

In order to illustrate the capabilities of MadSpin, we have applied it to top-quark pair production in association with a light Higgs boson at the LHC, considering the scalar (H) and pseudo-scalar (A) hypotheses for the Higgs boson. These processes have been analysed by two groups [68, 69] and a comparison between the two has appeared in ref. [70]. In those works it was shown that the NLO QCD corrections to the (undecayed) $t\bar{t}H$ processes are very mild, in particular on shapes of distributions.

Nevertheless, an observation of the Higgs boson calls for accurate theoretical predictions. The Higgs boson decays in the Standard Model predominantly into a pair of bottom quarks, which are also commonly produced by other QCD processes. Due to those irreducible QCD backgrounds, any search strategy for Higgs production relies on characteristics that are specific to the Higgs boson in order to separate signal from background. Spin correlations can provide such a discriminating characteristic.

With MadSpin, we provided the first predictions for $t\bar{t}H$ and $t\bar{t}A$ production at NLO accuracy, with inclusion of spin-correlation effects at leading order. In the setup of this analysis, the NLO parton-level events are first generated with aMC@NLO[1] and then decayed with

[1] Simulating LHC at 8 TeV, using PDF set MSTW2008(n)lo68cl, with $m_H = m_A = 125$ GeV and renormalization and factorization scales $\mu_R = \mu_F = (m_T(H/A)m_T(t)m_T(\bar{t}))^{(1/3)}$, without imposing kinematical cuts.

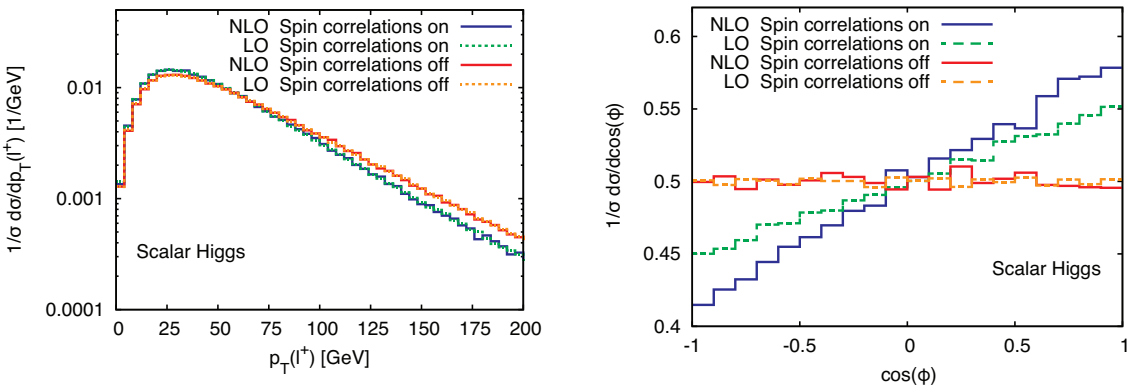

Figure 3.6: Next-to-leading-order cross sections differential in $p_T(l^+)$ (left) and in $\cos(\phi)$ (right) for $t\bar{t}H$ production with and without spin-correlation effects. For comparison, also the leading-order results are shown. Events were generated with aMC@NLO, then decayed with MadSpin, and finally passed to HERWIG for shower and hadronization.

MadSpin before they are passed to HERWIG for shower and hadronization. In this illustration, top and anti-top quarks are decayed semileptonically, whereas the Higgs is decayed into a pair of bottom quarks.

Figure 3.6 shows the normalized distribution of events with respect to $\cos(\phi)$, where ϕ is the angle between the direction of flight of l^+ in the t rest frame and the direction of flight of l^- in the $\bar{t}$ rest frame, and with respect to the transverse momentum of the hardest positively-charged lepton. Although spin-correlation effects significantly distort the distribution of events with respect to $\cos(\phi)$, their impact on the p_T spectrum of the leptons is milder, except at large transverse momentum. The relatively larger effect in the tail of this distribution can easily be understood from the fact that the inclusion of the spin correlations is a unitary procedure: a small change at low p_T, where the cross section is large, needs to be compensated by a larger (relative) effect at high p_T.

It is interesting that spin correlations have a much more dramatic influence on the shape of the observed p_T spectrum than NLO corrections: the leading order results fall directly on top of the NLO results for these normalized distributions (either with or without spin correlations). This suggests that for this observable, preserving spin correlations is more important than including NLO corrections. However, the inclusion of both is necessary for an accurate prediction of the distribution of events with respect to $\cos(\phi)$. In general, a scheme including both spin-correlation effects and QCD corrections is preferred: it retains the good features of reduced scale uncertainties in an NLO calculation, while keeping the correlations among the decay products.

Results for the pseudo-scalar Higgs boson are shown in fig. 3.7, which shows that the effects of the spin correlations on the transverse momentum of the charged lepton are similar to the case of a scalar Higgs boson: about 10% at small p_T, increasing to about 40% at $p_T \simeq 200$ GeV. On the other hand, the $\cos(\phi)$ distribution does not show any significant effect from the spin-correlations. Therefore this observable is sensitive to the

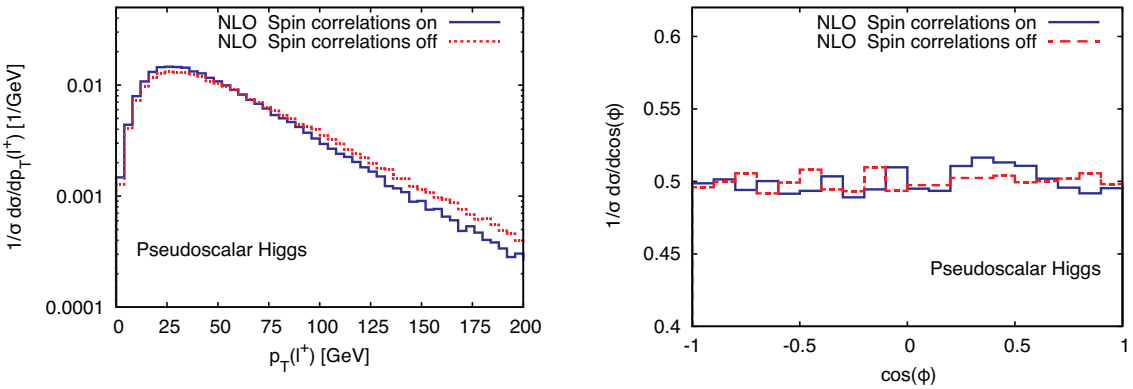

Figure 3.7: Next-to-leading-order cross sections differential in $p_T(l^+)$ (left) and in $\cos(\phi)$ (right) for $t\bar{t}A$ production with and without spin-correlation effects. Events were generated with aMC@NLO, then decayed with MadSpin, and finally passed to HERWIG for shower and hadronization.

transformation property of the Higgs boson under charge-parity conjugation, emphasising the importance of the inclusion of the spin-correlation effects.

3.5. Conclusions

In this chapter I discussed the generation of Monte Carlo events for scattering processes involving unstable particles. An important simplification in this context is the narrow-width approximation for particles whose width is small compared to their mass, effectively putting them on-shell. When employing that approximation, particular care has to be taken to retain spin-correlation effects. A procedure that does this has been implemented in the program MadSpin in a fully automatic way.

The algorithm of MadSpin has the feature that it reproduces off-shell effects through smearing of invariant masses according to Breit-Wigner distributions and that it recovers spin correlations effects at leading-order through an unweighting procedure. Limitations of the method show up in specific distributions (below threshold or far away from the resonance), as expected. But within its range of applicability, the method produces remarkable results that compare well against exact methods for specific processes. Going beyond specific cases, MadSpin can be applied to generic processes in the Standard Model and BSM models, an example of which is given by our study of (pseudo)scalar Higgs boson production in associated with a pair of top quarks.

In conclusion, the field of NLO computations in QCD has evolved into a mature discipline, witnessed by a wealth of programs that make detailed predictions for LHC cross sections. The achieved level of precision is not always enough, though, in which case the next order(s) in perturbation theory must be taken into account. Accordingly, the following chapters of this thesis venture into the realm of multi-loop diagrams.

Chapter 4

Cutting rules for Wilson line correlators

Infrared singularities of gauge theory scattering amplitudes play a fundamental role in both phenomenological and theoretical particle physics. Their precise cancellation between real and virtual amplitudes leaves behind large logarithmic contributions to cross sections that need to be resummed. They have a universal structure among different gauge theories [71,72], they exponentiate [73–75] and they allow an exploration of the all-order structure of scattering amplitudes [76,77].

A key tool for efficiently computing infrared singularities of scattering amplitudes is provided by the eikonal approximation. In this approximation, every energetic particle is replaced by a semi-infinite straight Wilson line and acts as a source of soft gluon radiation. The resulting Wilson line correlator captures precisely all infrared singularities, but is much simpler to compute than the original amplitude. In fact, Wilson line correlators are scale invariant, so their infrared singularities can also be obtained from their ultraviolet renormalization factor [10,78].

Focussing on the imaginary part of Wilson line correlators provides various important insights, concerning rapidity gaps [79,80], cross section calculations [81,82] and the breaking of collinear factorization theorems [83,84]. The latter effect is due to exchanges of transverse gluons, which produce purely imaginary terms that take the form of a non-Abelian analog of the QED Coulomb phase. It is therefore desirable to have a method for the direct calculation of imaginary parts.

In this chapter we first develop a notion of cuts of eikonal diagrams, which appear in the perturbative expansion of Wilson line correlators. In this new method, the imaginary part of eikonal diagrams is given by the sum of its cuts, in analogy with the Cutkosky rules for standard Feynman diagrams. The novelty of the cutting prescription is that it applies to the position-space representation of eikonal diagrams, as opposed to their momentum-space representation (for which a cutting prescription already existed [10]). We will see that the position-space cuts offer a substantial simplification over momentum-space cuts in the computation of imaginary parts of eikonal diagrams.

4.1. The perturbative expansion of Wilson line correlators: eikonal diagrams

Infrared singularities in scattering amplitudes arise from phase-space regions where massless particles have vanishing momentum, or where two massless particles become collinear. The description of collinear gluons can be isolated to individual external lines, which is well-understood. In this chapter we focus on infrared singularities caused by *soft particles*, whose momentum components are much smaller than the energy scale of the hard scattering event among the so-called *hard particles*. Soft particles can occur inside loop diagrams but also as extra radiation in the initial or final state, and the infrared singularities from these two cases cancel each other for so-called infrared safe observables. After this cancellation (and after absorbing remaining divergences into the definitions of masses, coupling constants and parton distribution functions) only finite terms are left, which take the form $\alpha_s^n \log^k(E/Q)$, where $0 \leq k \leq 2n$, E is the energy of a particle and Q the scale of hard scattering. For soft particles, $E \ll Q$ and the logarithms are large and the convergence of the perturbative expansion is endangered, as the effective expansion parameter is not α_s but rather α_s *times* $\log(E/Q)$. Such cases require the knowledge and organisation of these logarithmic terms to all orders in the strong coupling constant, which is referred to as *resummation*. Studying the infrared singularities is crucial to uncover the structure of these large logarithms and thus aids cross section calculations in regimes where perturbation theory is troubled. Let us see how infrared singularities may be identified.

We consider a generic amplitude, containing a hard particle which radiates by emitting a soft particle. To be specific, we take the hard particle to be a massless final state quark and the soft particle to be an off-shell gluon[1] (see fig. 4.1). The amplitude for this process may be decomposed in the following way

$$\mathscr{M}^{s,a,\mu} = \bar{u}^s(p)\, igt^a\gamma^\mu \, \frac{i(\not{p}+\not{k})}{(p+k)^2+i\eta}\mathscr{M}_0 \,. \tag{4.1}$$

Here, $\bar{u}^s(p)$ is the spinor of the final state quark, $igt^a\gamma^\mu$ is the quark-gluon coupling, followed by the intermediate quark propagator and $\mathscr{M}_0$, representing the rest of the process.

The amplitude in eq. (4.1) simplifies considerably upon making the *eikonal approximation*, which consists of taking the limit $k^\mu \ll p^\mu$ for all $\mu = 0,1,2,3$. As a consequence, the term $\not{k}$ can be dropped from the numerator of the quark propagator. The remaining $\not{p}$ and the gamma matrix can be anti-commuted using the Dirac algebra, $\{\gamma^\mu,\gamma^\nu\} = 2\eta^{\mu\nu}$, leaving only $2p^\mu$ upon imposing the Dirac equation $\bar{u}^s(p)\not{p} = 0$. As a result, the amplitude reduces to

$$\mathscr{M}^{s,a,\mu} \xrightarrow{k^\mu \ll p^\mu} igt^a \left(\frac{ip^\mu}{p\cdot k + i\eta}\right) \bar{u}^s(p)\,\mathscr{M}_0 \,. \tag{4.2}$$

[1] There are various other options. The soft particle can be either a gluon or a photon, in which case the hard particle can be a quark/gluon or quark/lepton/vector boson, respectively. The hard particle can also be among the initial states. In this chapter we emphasize the application to gluons.

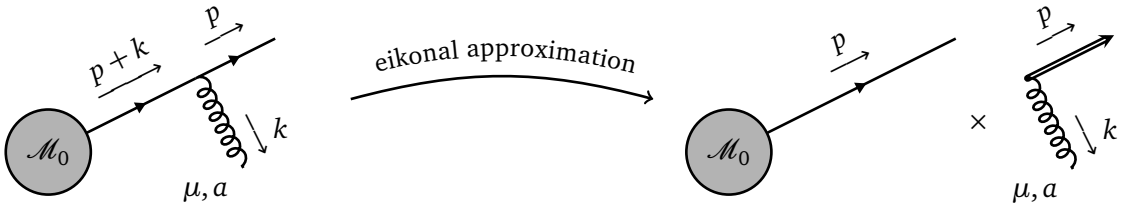

Figure 4.1: The eikonal approximation, valid when $k^\mu \ll p^\mu$, has the effect of factorizing soft gluon emissions from the remaining hard process contained in $\mathscr{M}_0$.

The right-hand side of eq. (4.2) has two interesting features. First, it is free of Dirac matrices. The corresponding physical interpretation is that the soft gluon cannot resolve the spin of the emitting particle due to its large wavelength. Second, the factor in round brackets, which is an eikonal propagator, is invariant under rescaling of p^μ. This means that the gluon is insensitive to the energy of the quark, which in turn does not recoil after emitting the soft gluon. Effectively, the (kinematic part of) the emission of a soft gluon can be described with the eikonal Feynman rule

$$\frac{ip^\mu}{p\cdot k + i\eta} = \frac{iv^\mu}{v\cdot k + i\eta}\,, \tag{4.3}$$

where v^μ is the unit vector ($v^2 = 1$) along the direction of the emitting particle ($v^\mu \propto p^\mu$).

One may ask if the eikonal Feynman rules can be derived from some quantum field theory. The answer turns out to be affirmative [85,86]. The underlying theory is the quantum field theory of soft gauge fields, described by the path integral

$$Z_n = \int \mathscr{D}A_\mu\, e^{iS[A_\mu]} \prod_{i=1}^{n} \left(\mathscr{P}\, e^{ig\int \mathrm{d}x_i^\mu A_\mu(x_i)} \right), \tag{4.4}$$

where $S[A_\mu]$ is the Yang-Mills action for the soft gauge field A_μ and where the interaction with n hard particles is encoded through a product of path-ordered exponentials, each containing the gauge field integrated along the trajectory x_i^μ of the ith hard particle.[2] The path ordered exponentials are semi-infinite *Wilson lines*,

$$\Phi_{v_i} \equiv \Phi_{v_i}(0,\infty) = \mathscr{P}\exp\left(ig\int_0^\infty \mathrm{d}t\; v_i^\mu A_\mu(tv_i) \right), \tag{4.6}$$

where we parametrized the gluon emissions at $x_i^\mu = t\,v_i^\mu$ by a time t along the fixed direction of a Wilson line. The normalized path integral with the insertion of the product of

[2] The path integral in eq. (4.4) indeed produces the eikonal Feynman rules. Upon substituting the path $x_i^\mu = t\,v_i^\mu$ and inserting the Fourier transform of the soft gauge field, the exponent becomes

$$ig\int \mathrm{d}x^\mu A_\mu(x) = ig\int_0^\infty \mathrm{d}t\, v^\mu \int \frac{\mathrm{d}^d k}{(2\pi)^d}\, \widetilde{A}_\mu(k)\, e^{i(k\cdot v)t} = \int \frac{\mathrm{d}^d k}{(2\pi)^d}\, \widetilde{A}_\mu^a(k)\, igt^a\, \frac{v^\mu}{v\cdot k}\,, \tag{4.5}$$

from which one can read of the eikonal Feynman rule in eq. (4.3).

Wilson lines is a *Wilson line correlator*

$$S = Z_n/Z_0 = \left\langle \Phi_{v_1} \Phi_{v_2} \cdots \Phi_{v_n} \right\rangle , \tag{4.7}$$

where $Z_0 = \int \mathscr{D}A_\mu \, e^{iS[A_\mu]}$. This correlator describes the scattering amplitude among n hard particles that interact only through the exchange of soft gluons. Recalling the argument in the beginning of this chapter, it may be thought of as the eikonal limit of some n-particle amplitude in another theory, like QCD. Therefore the correlator S captures the infrared singularities coming from soft gluon exchanges among hard particles. Wilson line correlators thus provide a tool for computing infrared singularities of scattering amplitudes in other gauge theories.

The Wilson line correlator in eq. (4.7) contains infrared *and* ultraviolet singularities (coming, respectively, from the infrared divergences of the original gauge theory and the new interaction vertex introduced by the product of Wilson lines). A convenient method for regulating those singularities simultaneously is provided by dimensional regularization, with $d = 4 - 2\epsilon$ spacetime dimensions. This introduces a dependence of S on ϵ and the renormalization scale μ. Since loop corrections have a non-integer mass dimension in dimensional regularization and the correlators depend on no other scales (the v_i are dimensionless), one concludes that all loop corrections vanish, leaving $S(\epsilon_{\text{UV+IR}}, \mu) = 1$. In fact, in dimensional regularization scaleless integrals vanish in general.

This observation implies that the renormalized correlator equals the ultraviolet counterterm,

$$S_{\text{ren}}(\epsilon_{\text{IR}}, \mu) \equiv S(\epsilon_{\text{UV+IR}}, \mu)\, Z(\epsilon_{\text{UV}}, \mu) = Z(\epsilon_{\text{UV}}, \mu) \, , \tag{4.8}$$

where a subscript on ϵ indicates its origin of infrared and/or ultraviolet nature. Ultimately we are interested in the infrared singularities captured by $S_{\text{ren}}(\epsilon_{\text{IR}}, \mu)$, but this equation implies that we can equivalently study the counterterm $Z(\epsilon_{\text{UV}}, \mu)$. Studying the latter is convenient in view of the well-developed theory of ultraviolet renormalization. In particular, the dependence of an ultraviolet counterterm on the renormalization scale is encoded in a (finite) anomalous dimension Γ, through the relation

$$\Gamma(\epsilon_{\text{UV}}, \mu) = -\frac{\mathrm{d} \log Z(\epsilon_{\text{UV}}, \mu)}{\mathrm{d} \log \mu} \, . \tag{4.9}$$

For instance, if Z is taken to be the strong coupling constant α_s, then Γ is the well-known QCD β-function. Applied to Wilson line correlators, Γ is either the cusp anomalous dimension (for two Wilson lines) or more generally the soft anomalous dimension matrix. The cusp anomalous dimension has been computed up to three loops in QCD [10, 87, 88] and some progress has been made towards the four-loop result [89]. The soft anomalous dimension matrix is more involved due to its dependence on more variables and has been computed at two loops [90–96] and recently at three loops [97–99].

In practice, the calculation of the anomalous dimension is performed by removing the infrared singularities in Wilson line correlators. This can be implemented rigorously by in-

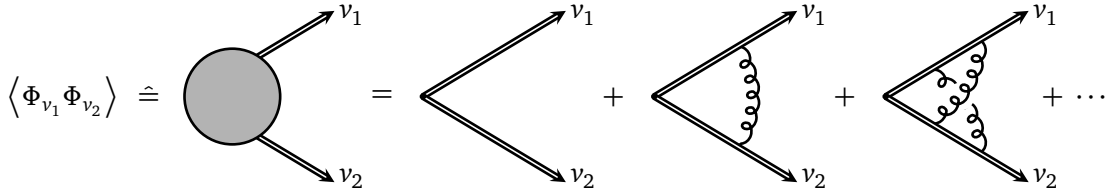

Figure 4.2: The perturbative expansion of Wilson line correlators is given in terms of eikonal diagrams. This figure shows a few terms in the expansion of a correlator of two Wilson lines.

cluding an exponential damping factor in the definition of each Wilson line operator [100],

$$\Phi_{v_i} \;\to\; \mathscr{P} \exp\left(i g \mu^{\epsilon} \int_0^{\infty} \mathrm{d}t \; v_i \cdot A_{\mu}(t v_i) \, e^{-mt\sqrt{|v_i^2|}} \right) , \tag{4.10}$$

so that the long distance contributions are smoothly cut off. In this chapter we shall be somewhat more practical and introduce the necessary exponential damping factors where needed. In any case, the precise way in which the infrared singularities are removed is not very relevant, as long as different diagrams added together have been calculated with the same regularization procedure, so that the ultraviolet poles may be unambiguously extracted.

The perturbative expansion of Wilson line correlators with respect to the strong coupling constant is given in terms of eikonal diagrams (see fig. 4.2). Perhaps the simplest example of an eikonal diagram is the one-loop correction to a correlator of two Wilson lines,

$$F^{(1)} = i g^2 C_F \mu^{2\epsilon} \int \frac{\mathrm{d}^d k}{(2\pi)^d} \frac{v_1 \cdot v_2}{(k^2 + i\eta)(v_1 \cdot k + i\eta)(v_2 \cdot k - i\eta)} \;\hat{=}$$

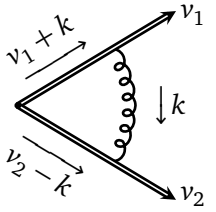

. (4.11)

The denominator factors of the integrand in this formula come from, respectively, the gluon propagator and the two Wilson line propagators. The opposite $i\eta$ prescription in the last denominator factor indicates that the Wilson line Φ_{v_2} absorbs (rather than emits) a gluon. We have adopted the Feynman gauge and taken the gauge group to be SU(N), with the quadratic Casimir operator $C_F = (N^2 - 1)/(2N)$ for the fundamental representation.

An alternative formula for $F^{(1)}$ is given by its representation in position space, which can be obtained by Schwinger parametrising the eikonal propagators in eq. (4.11) and performing

the resulting Fourier transform. This yields the position-space representation

$$F^{(1)} = C^{(1)}\mu^{2\epsilon}\int_0^\infty \mathrm{d}t_1 \int_0^\infty \mathrm{d}t_2 \, \frac{v_1\cdot v_2}{\left[-(t_1 v_1 - t_2 v_2)^2 + i\eta\right]^{1-\epsilon}} \;\hat{=}\; \quad , \tag{4.12}$$

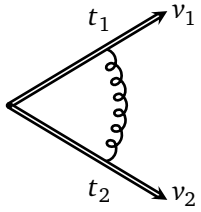

where the prefactor

$$C^{(1)} = g^2 C_F \frac{\Gamma(d/2-1)}{4\pi^{d/2}} \tag{4.13}$$

absorbs the overall constants. Notice that this diagram has only one propagator in position space, which corresponds to the exchanged gluon. In this representation the Wilson lines merely provide a recoilless source of gluon radiation. One benefit of this representation is the limited number of integrations, namely two one-dimensional integrals over the emission and absorption times t_1 and t_2, as compared to the d-dimensional integration in the momentum-space representation. Furthermore, this representation can be written down directly (without passing through momentum space) by using the eikonal Feynman rules in position space [101].

The one-loop eikonal diagram $F^{(1)}$ provides an excellent starting point for the studies in the remainder of this chapter, where we will look in particular at the imaginary part of eikonal diagrams as a means to calculate the corresponding imaginary part of Wilson line correlators order-by-order in perturbation theory.

4.2. The imaginary part of eikonal diagrams

The imaginary part of eikonal diagrams has been found to play a role in a variety of topics, including rapidity gaps [79, 80], cross section calculations [81, 82] and the breaking of collinear factorization theorems [83, 84]. This section starts with the explicit computation of the one-loop exchange diagram and its imaginary part, after which the origin of the imaginary part is analysed from the perspectives of causality and unitarity. These analyses naturally lead to a method for computing the imaginary part from diagrammatic cuts, which will be discussed in the next section.

Let us calculate the one-loop eikonal diagram $F^{(1)}$. This is most easily done starting from its position-space representation in eq. (4.12). The integrations over t_1 and t_2 produce divergences, which can be extracted via the change of variables $(t_1, t_2) = (\lambda x, \lambda(1-x))$, with $0 \leq x \leq 1$. The dimension-full quantity λ measures the overall distance between the origin and the gluon exchange, while x encodes the angle under which the gluon is emitted.

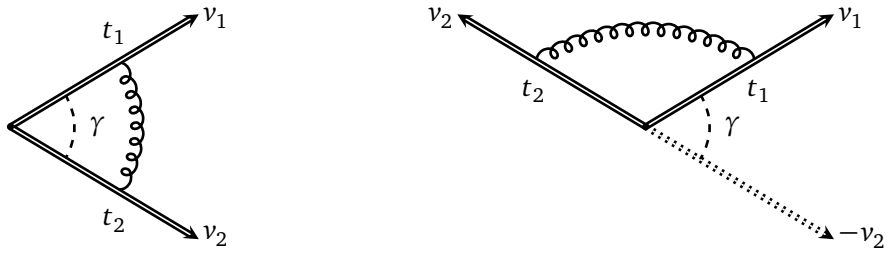

(a): $v_1 \cdot v_2 > 0$ (timelike) (b): $v_1 \cdot v_2 < 0$ (spacelike)

Figure 4.3: One-loop eikonal diagram in two different configurations of external momenta. In (a) both Wilson lines represent final-state partons, as for example in $e^+e^- \to q\bar{q}$, so in this case $v_1 \cdot v_2 > 0$. In (b) one Wilson line represents a final-state particle and one represents an initial-state particle (like in deep inelastic scattering), so that $v_1 \cdot v_2 < 0$.

After this change of variables the diagram reads

$$F^{(1)} = C^{(1)}\mu^{2\epsilon}\int_0^\infty \frac{\mathrm{d}\lambda}{\lambda^{1-2\epsilon}}\int_0^1 \mathrm{d}x \frac{v_1\cdot v_2}{\left[-(xv_1-(1-x)v_2)^2+i\eta\right]^{1-\epsilon}}\,. \tag{4.14}$$

The λ-integral is divergent at both endpoints: in the region $\lambda \to 0$ it develops an ultraviolet singularity while in the region $\lambda \to \infty$ resides an infrared singularity. Following the discussion in section 4.1, we regulate the infrared divergence in a gauge invariant fashion by introducing an exponential damping factor $e^{-\Lambda\lambda}$ with $\Lambda \ll 1$, whereby the λ-integral becomes

$$\mu^{2\epsilon}\int_0^\infty \frac{\mathrm{d}\lambda\, e^{-\Lambda\lambda}}{\lambda^{1-2\epsilon}} = \Gamma(2\epsilon)\left(\frac{\mu}{\Lambda}\right)^{2\epsilon} = \frac{1}{2\epsilon}\left(\frac{\mu}{\Lambda}\right)^{2\epsilon} + \mathcal{O}(\epsilon^0)\,. \tag{4.15}$$

The remaining integration over x is more interesting, because it depends on the given Wilson line velocities v_1 and v_2. Since these velocities may correspond to either initial or final state particles, there are two distinct situations. For initial-initial state and final-final state configurations we have that $v_1 \cdot v_2 > 0$, or *timelike* kinematics. On the other hand, the mixed configurations initial-final state feature *spacelike* kinematics, $v_1 \cdot v_2 < 0$. These two situations are connected via analytic continuation of an initial state particle to the final state, or vice versa (see fig. 4.3). The integration over x in eq. (4.14) turns out to be most easily carried out in the mixed configuration. Introducing a Minkowski angle γ angle between the two velocities, the one-loop diagram with spacelike kinematics evaluates to

$$F^{(1)} = \frac{C^{(1)}}{2\epsilon}\left(\frac{\mu}{\Lambda}\right)^{2\epsilon}\gamma\coth\gamma\,, \qquad \text{for } \gamma = \operatorname{arcosh}(-v_1\cdot v_2) > 0\,. \tag{4.16}$$

The analogous result for timelike kinematics can be obtained by flipping the sign of v_2. This is accommodated by changing the angle according to $\gamma \to i\pi - \gamma$,

$$F^{(1)} = \frac{C^{(1)}}{2\epsilon}\left(\frac{\mu}{\Lambda}\right)^{2\epsilon}(\gamma - i\pi)\coth\gamma\,, \qquad \text{for } \gamma = \operatorname{arcosh}(v_1\cdot v_2) > 0\,. \tag{4.17}$$

We observe that the imaginary part of $F^{(1)}$ in eqs. (4.16) and (4.17) is respectively vanishing and non-vanishing. The origin of this phenomenon has a nice physical interpretation in terms of causality and unitarity.

4.2.1. Physical interpretation of the imaginary part: causality

The origin of the imaginary part of $F^{(1)}$ for timelike kinematics may be understood from a causality consideration by inspecting the position-space representation of the eikonal diagram in eq. (4.12). Focussing on the imaginary part to the leading order in the dimensional regularization parameter allows to drop ϵ in the power of the propagator. After furthermore stripping off real prefactors, the position-space integral takes the form

$$\int_0^\infty \mathrm{d}t_1 \int_0^\infty \mathrm{d}t_2 \, \frac{1}{-(t_1 v_1 - t_2 v_2)^2 + i\eta} \, . \tag{4.18}$$

For timelike kinematics, $v_1 \cdot v_2 > 0$, there are regions $t_1 = t_2 e^{\pm\gamma}$ within the integration domain where $(t_1 v_1 - t_2 v_2)^2 = 0$. Here the $+i\eta$ term becomes relevant and generates an imaginary part. This introduces a complex phase in the Wilson line correlator, which can be absorbed into the definition of the states corresponding to the Wilson lines. Indeed, the soft gluons can alter the state of the hard particles only by a complex phase, since the eikonal interactions preserve the momentum and polarization of the states [81]. What is happening physically at times t_1, t_2 for which the denominator in eq. (4.18) vanishes is that the two particles traveling along v_1 and v_2 become lightlike separated, see fig. 4.4(a). As a result, the causally connected particles can affect each other's states through exchanges of lightlike gluons. In contrast, for spacelike kinematics, $v_1 \cdot v_2 < 0$, the integral in eq. (4.18) has no imaginary part: the denominator $(t_1 v_1 - t_2 v_2)^2$ is strictly positive within the region of integration and the $+i\eta$ can therefore be dropped. In this situation, the partons are never lightlike separated and cannot change each other's states, see fig. 4.4(b).

This observation suggests that the imaginary part may be interpreted as an inter-particle potential between causally connected states. Indeed, in the non-relativistic limit the final and initial two-particle states are related in the interaction picture through time evolution by $|f\rangle_I = e^{i\int_0^\infty \mathrm{d}t\, e^{-\Lambda t} V_I(t)} |i\rangle_I$ where V_I denotes the interaction potential. The relation of the correlator to a non-relativistic potential can be made precise in the situation where the pair of energetic particles carry no color charges, as for example in the case of an e^+e^- pair. In Abelian gauge theories, like QED, the correlator of two Wilson lines can be written as the exponential of the sum of connected diagrams [102],

$$W \equiv \left\langle \Phi_{v_1} \Phi_{v_2} \right\rangle = \exp\left(F^{(1)} + \mathcal{O}(e^4) \right) , \tag{4.19}$$

where $F^{(1)}$ is the one-loop diagram in fig. 4.3 and the suppressed diagrams of $\mathcal{O}(e^4)$ contain a single lepton loop connected to the Wilson lines by an arbitrary even number of soft-photon exchanges. Using the result for the diagram $F^{(1)}$ computed for timelike kinematics

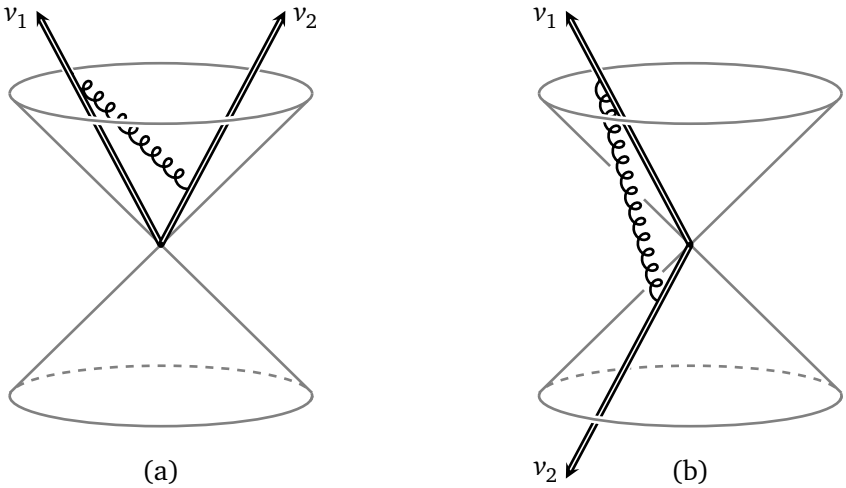

Figure 4.4: The one-loop eikonal diagrams of fig. 4.3 embedded in a space-time diagram. In (a) both Wilson lines are confined to the interior of the future light cone, describing two final state particles. In this case the particles can become lightlike separated, which is illustrated by the exchange of a lightlike gluon (i.e. a gluon that is aligned to the light cone). In (b) there is one incoming particle inside the past light cone and an outgoing particle inside the future light cone. These particles are never lightlike separated and indeed the gluon stretching between these two Wilson lines is necessarily timelike (i.e. off shell).

in eq. (4.17) with $g \to e$ and $C_F \to 1$ to recover the Abelian case, the cusp anomalous dimension (see eq. (4.9)) of this Wilson line correlator evaluates to

$$\Gamma_{\text{cusp}}(\gamma) \equiv -\lim_{\epsilon\to 0} \frac{\mathrm{d}\log W}{\mathrm{d}\log\mu} = -\frac{e^2}{4\pi^2}(\gamma - i\pi)\coth\gamma \,. \tag{4.20}$$

The non-relativistic limit of this result corresponds to the small-angle regime $\gamma \approx 0$, where the two velocities v_1 and v_2 are nearly collinear and the relative velocity of the hard leptons thus small. Expanding eq. (4.20) around $\gamma = 0$ and taking the imaginary part, we find

$$\operatorname{Im}\Gamma_{\text{cusp}}(\gamma) = \frac{e^2}{4\pi\gamma} + \mathcal{O}(\gamma^0) \,. \tag{4.21}$$

We observe that the imaginary part of the cusp anomalous dimension evaluated in timelike kinematics takes the form of the non-relativistic Coulomb potential (after replacing the angle γ by the distance between the two fermions to acquire the appropriate dimension).

This relation extends to conformal field theories, such as $\mathcal{N} = 4$ super Yang-Mills theory, where the state-operator correspondence relates Wilson line operators in Minkowski space to states in $\mathbb{R}\times\mathrm{AdS}_3$. In radial quantization, a pair of Wilson lines intersecting at a cusp angle γ with the resulting anomalous dimension $\Gamma_{\text{cusp}}(\gamma)$ is mapped to a pair of static charges in AdS_3 separated by a distance γ with an electrostatic energy of $\operatorname{Im}\Gamma_{\text{cusp}}(\gamma)$ [103]. For small values of the cusp angle, the charges on AdS_3 become closer than the curvature scale, and the electrostatic energy takes the form of the non-relativistic interquark potential in flat space [104, 105]. (The non-relativistic approximation becomes relevant here, as in the

small-angle regime $\gamma \approx 0$, the relative velocity of the hard partons is small, as discussed above.)

However, for non-Abelian and non-conformal gauge theories such as QCD, diagrams containing loop corrections to the soft propagators will have a dependence on the beta function, thereby explicitly breaking the scale invariance of the diagram. As a result, in QCD, the imaginary part of the three-loop cusp anomalous dimension $\Gamma^{(3)}_{\text{cusp}}$ differs from the static interquark potential by terms proportional to the beta function[3] [87].

4.2.2. Physical interpretation of the imaginary part: unitarity

The origin of the imaginary part of $F^{(1)}$ for timelike kinematics may also be understood from unitarity, starting from the momentum-space representation in eq. (4.11). In ref. [10] it has been shown that the imaginary part of the one-loop diagram may be obtained by replacing the two eikonal propagators with delta functions,

$$\frac{1}{k\cdot v_i \pm i\eta} \xrightarrow{\text{cut}} \mp 2\pi i\,\theta(v_i^0)\,\delta(k\cdot v_i)\,. \tag{4.22}$$

This cutting prescription can be thought of as the eikonal limit of the standard Cutkosky rules. Applying it to $F^{(1)}$ in eq. (4.11), its imaginary part is determined as follows

$$2i\ \text{Im}\,F^{(1)} = (2\pi)^2 i g^2 C_F \theta(v_1^0)\theta(v_2^0)(v_1\cdot v_2)\mu^{2\epsilon}\int \frac{\mathrm{d}^d k}{(2\pi)^d}\,\frac{\delta(v_1\cdot k)\,\delta(v_2\cdot k)}{k^2+i\eta}\,. \tag{4.23}$$

This representation of the imaginary part of the one-loop diagram (see fig. 4.5) motivates two remarks.

The first concerns the region of momentum space that gives rise to the imaginary part. Defining the light-cone variables $k^\pm \equiv \frac{1}{\sqrt{2}}(k^0 \pm k^3)$ and choosing the Lorentz frame in which the transverse components of the velocities vanish, $v_{iT} = 0$, the support of the delta functions in eq. (4.23) is the region where the momentum of the exchanged gluon is maximally transverse,

$$k_T \gg k^+ \sim k^- \approx 0\,, \tag{4.24}$$

which was identified in ref. [10] as the Glauber region [108]. This explains our anticipation in the introduction: the imaginary part of eikonal diagrams arises from the exchanges of Glauber-region gluons.

The second remark concerns the physical interpretation of applying the momentum-space cutting rules. By writing the delta functions in eq. (4.23) in terms of their plane-wave

[3] This can be seen by comparing the N_f^2 contribution to $\Gamma^{(3)}_{\text{cusp}}$, given in eq. (A.2) of ref. [106], against the N_f^2 term of the three-loop static QCD potential, given in eq. (10) of ref. [107].

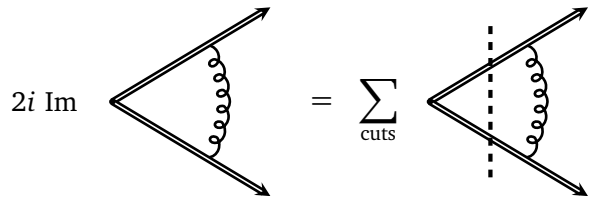

Figure 4.5: Graphical representation of cuts of eikonal diagrams in momentum space.

representation $\delta(x) = \frac{1}{2\pi}\int_{-\infty}^{\infty} \mathrm{d}t\, e^{itx}$ and performing the Fourier transform we find

$$2i\ \mathrm{Im}\, F^{(1)} = C^{(1)}\theta(v_1^0)\theta(v_2^0)\mu^{2\epsilon}\int_{-\infty}^{\infty}\mathrm{d}t_1\int_{-\infty}^{\infty}\mathrm{d}t_2\,\frac{v_1\cdot v_2}{\left[-(t_1v_1-t_2v_2)^2+i\eta\right]^{1-\epsilon}}\,. \tag{4.25}$$

Notice that this expression is similar to the position-space representation of the *uncut* one-loop diagram in eq. (4.12). The only difference is that the integration bounds are extended according to $\int_0^\infty \mathrm{d}t_i \longrightarrow \int_{-\infty}^\infty \mathrm{d}t_i$. This state of affairs can be simply understood on physical grounds: as the hard particles have been put on shell through the cutting rule eq. (4.22), they are now asymptotic states propagating from $t_i = -\infty$ to the interaction point.

We see that the position- and momentum-space representations of eikonal diagrams offer complementary points of view on the origin of their imaginary part. To summarize, in the position-space representation, the imaginary part is seen to arise from the exchanges of lightlike soft gauge bosons whose emission and absorption change the phases of the hard-particle states. In contrast, in momentum space, the imaginary part arises from the two hard particles going on shell and exchanging Glauber gluons.

The momentum-space cutting prescription has the conceptual advantage of factoring eikonal diagrams into on-shell lower-loop and tree diagrams, which in turn can be computed as independent objects. However, the resulting cut diagrams involve integrations over two-, three-, four-, ... particle phase space (see fig. 4.6). In practice, the evaluation of these phase-space integrals poses a substantial computational challenge, which limits the appli-

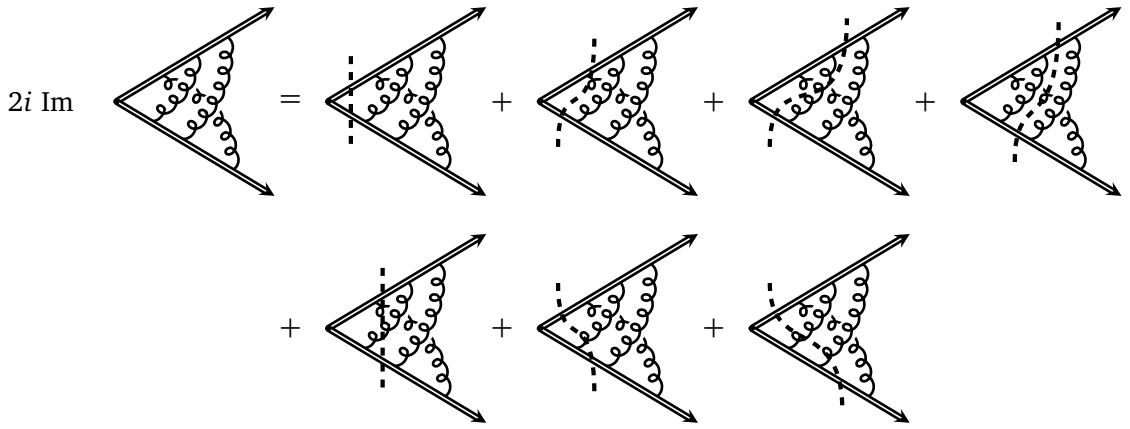

Figure 4.6: The non-vanishing momentum-space cuts of a non-planar three-loop ladder diagram. The cuts require the evaluation of two-, three- and four-particle phase-space integrals.

cability of the momentum-space cutting prescription for obtaining imaginary parts.

In position space, eikonal diagrams without internal vertices take the form of iterated integrals in position space. Their imaginary parts can, in this representation, be obtained more straightforwardly, as we shall see in the next section.

4.3. Position-space cuts of eikonal diagrams

In the previous section we have seen a cutting prescription for computing the imaginary part of eikonal diagrams in momentum space, which has been known a long time [10]. One might wonder if there exist a similar cutting prescription in position space, motivated by the idea that the actual calculation of cut diagrams may be simpler than in momentum space. Indeed, such a cutting prescription can be defined, as will be described below.

4.3.1. The cut one-loop diagram

As a warm-up, let us turn to the question of how the imaginary part of the eikonal diagram $F^{(1)}$ may be obtained from its position-space representation. It is convenient to start from the integral representation in eq. (4.14), where the leading divergence has been extracted. We will restrict our attention to the leading term in the Laurent expansion in the dimensional regulator ϵ, and consequently drop the ϵ in the propagator exponent. We can then use the formula

$$\int_a^b \mathrm{d}x \, \frac{f(x)}{D(x) \pm i\eta} = \mathrm{PV} \int_a^b \mathrm{d}x \, \frac{f(x)}{D(x)} \mp i\pi \int_a^b \mathrm{d}x \, f(x) \, \delta\big(D(x)\big) \,, \tag{4.26}$$

where PV indicates that the Cauchy principal value prescription is to be applied, and the integration bounds a and b are real numbers. The denominator $D(x)$ is a real-valued polynomial in x, and the numerator $f(x)$ is an arbitrary real-valued function without poles or branch points inside the integration path. As both integrals on the right-hand side of eq. (4.26) are real, this formula achieves a decomposition into a purely real and purely imaginary part. Accordingly, we define the position-space cut prescription

$$\frac{1}{D(x) \pm i\eta} \xrightarrow{\text{cut}} \mp i\pi \, \delta\big(D(x)\big) \,, \tag{4.27}$$

in terms of which it is straightforward to obtain the imaginary part of the one-loop diagram $F^{(1)}$ to the leading order in ϵ in either one of the two kinematic configurations. Considering timelike kinematics in fig. 4.3(a) first and applying the prescription eq. (4.27) to eq. (4.14) with the ϵ in the propagator exponent set to zero, we find

$$\mathrm{Im}\, F^{(1)} = -\pi C^{(1)} \, v_1 \cdot v_2 \, \mu^{2\epsilon} \int_0^\infty \frac{\mathrm{d}\lambda \, e^{-\Lambda\lambda}}{\lambda^{1-2\epsilon}} \int_0^1 \mathrm{d}x \, \delta\big(\big(x v_1 - (1-x) v_2\big)^2\big) \,. \tag{4.28}$$

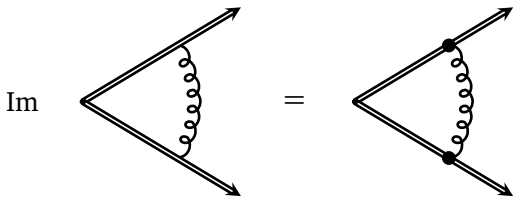

Figure 4.7: Graphical representation of the position-space cutting equation for a one-loop eikonal diagram. The black dots represent the emission/absorption of a lightlike gluon.

We can integrate out the delta function by use of the identity

$$\int_0^1 \mathrm{d}x\, \delta(Ax^2+Bx+C) = \frac{1}{\sqrt{\Delta}} \sum_{i=1,2} \theta(\rho_i)\theta(1-\rho_i)\,, \tag{4.29}$$

where $\Delta \equiv B^2 - 4AC$ and ρ_i respectively denote the discriminant and roots of the polynomial. The roots $\rho_i = \frac{1}{1+e^{\pm\gamma}}$ of the delta function argument in eq. (4.28) are manifestly located inside the domain of the x-integration. The result of integrating out the delta function is therefore

$$\mathrm{Im}\, F^{(1)} = -\pi \frac{C^{(1)}}{2\epsilon} \left(\frac{\mu}{\Lambda}\right)^{2\epsilon} \coth\gamma\,, \tag{4.30}$$

which is in agreement with eq. (4.17). The calculation for spacelike kinematics in fig. 4.3(b) is completely analogous, except that in this case $\int_0^1 \mathrm{d}x\, \delta\big(\big(xv_1-(1-x)v_2\big)^2\big) = 0$, as both roots $\rho_i = \frac{1}{1-e^{\pm\gamma}}$ are located outside the domain of integration. We therefore find a vanishing imaginary part, in agreement with eq. (4.16). We conclude that in both cases (a) and (b) the cutting prescription eq. (4.27) produces the correct imaginary part. A graphical notation for the position-space cutting prescription is introduced accordingly (see fig. 4.7).

4.3.2. Generalization to multi-loop diagrams

In order to generalize our position-space cutting prescription to more complicated diagrams, we have to start by introducing some notation. An arbitrary L-loop eikonal diagram without internal vertices in position space is composed of L soft-gluon propagators (rungs). Each rung extends between the Wilson lines spanned by any two external four-velocities $v_1,\ldots,v_n$ where $1 \le n \le L+1$. For the jth rung we will denote these four-velocities by v_{ℓ_j} and v_{r_j}. We let $t_{i,k}$ denote the position of the kth attachment on the Wilson line spanned by v_i, counting from the hard interaction vertex and outwards, so that $0 \le t_{i,1} < t_{i,2} < \cdots < t_{i,N_i-1} < t_{i,N_i}$, where N_i denotes the total number of soft-gluon attachments on the Wilson line. In addition, for the jth rung, we let the variables m_j and n_j record the soft-gluon attachment numbers on the Wilson lines spanned by v_{ℓ_j} and v_{r_j}, respectively. The L-loop eikonal diagram is then defined as the $2L$-fold iterated integral

$$F^{(L)} = C^{(L)}(g\mu^\epsilon)^{2L} \prod_{j=1}^{L} \int_0^\infty \mathrm{d}t_{\ell_j,m_j} \mathrm{d}t_{r_j,n_j} \frac{(v_{\ell_j}\cdot v_{r_j}) \prod_{i=1}^{n} \prod_{k=0}^{N_i} \theta(t_{i,k+1}-t_{i,k})}{\big[-(t_{\ell_j,m_j}v_{\ell_j} - t_{r_j,n_j}v_{r_j})^2 + i\eta\big]^{1-\epsilon}}\,, \tag{4.31}$$

where the kinematics-independent prefactor $C^{(L)}$ is determined by the color structure of the diagram and where it is implied that $t_{i,N_i+1} \equiv \infty$ and $t_{i,0} \equiv 0$. Without loss of generality, we will assume that any rungs with both endpoints attached to the same Wilson line have been integrated out, and we suppress the resulting pole factors in ϵ.

To extract the imaginary part of $F^{(L)}$ from the integral representation in eq. (4.31) it turns out to be useful to perform a change of variables which leaves each soft propagator dependent on a single variable. The idea is to first express the attachment points of the jth rung in terms of "polar" coordinates measuring the distance ρ_j to the cusp and x_j essentially measuring the emission angle of the soft gluon to the Wilson line,

$$\begin{pmatrix} t_{\ell_j,m_j} \\ t_{r_j,n_j} \end{pmatrix} = \rho_j \begin{pmatrix} x_j \\ 1-x_j \end{pmatrix}, \quad \text{where} \quad \begin{cases} 0 \le \rho_j < \infty, \\ 0 \le x_j \le 1. \end{cases} \tag{4.32}$$

After this change of variables, the diagram takes the form

$$F^{(L)} = C^{(L)} (g\mu^\epsilon)^{2L} \prod_{j=1}^{L} \int_0^\infty \frac{\mathrm{d}\rho_j}{\rho_j^{1-2\epsilon}} \int_0^1 \mathrm{d}x_j \, P^{[\epsilon]}_{\ell_j r_j}(x_j) \, \Theta(\boldsymbol{\rho}, \boldsymbol{x}), \tag{4.33}$$

where the soft propagators are defined as

$$P^{[\epsilon]}_{ij}(x) = \frac{v_i \cdot v_j}{\left[-\big(x v_i - (1-x) v_j\big)^2 + i\eta\right]^{1-\epsilon}}, \tag{4.34}$$

and where the nesting of the integrations is encoded through Θ, defined by

$$\Theta(\boldsymbol{\rho}, \boldsymbol{x}) = \prod_{i=1}^{n} \prod_{k=0}^{N_i} \theta(t_{i,k+1} - t_{i,k}) \Big|_{\left(\begin{smallmatrix} t_{\ell_j,m_j} \\ t_{r_j,n_j} \end{smallmatrix}\right) = \rho_j \left(\begin{smallmatrix} x_j \\ 1-x_j \end{smallmatrix}\right)}. \tag{4.35}$$

We observe that the original dependence of the soft propagators on the radial coordinates ρ_j has scaled out in eq. (4.33), such that each propagator now depends on a single variable x_j. This turns out to be particularly advantageous for the purpose of extracting the imaginary part of the diagram, as this circumvents the need to divide a higher-dimensional domain of integration into subdomains characterized by supporting a specific number of propagator roots.

Now we extract the overall divergence of the diagram by setting $\tau_1 \equiv \rho_1$ and then applying the following sequence of $L-1$ substitutions

$$\begin{pmatrix} \tau_1 \\ \rho_2 \end{pmatrix} = \tau_2 \begin{pmatrix} y_1 \\ 1-y_1 \end{pmatrix}, \ \dots, \ \begin{pmatrix} \tau_{L-1} \\ \rho_L \end{pmatrix} = \tau_L \begin{pmatrix} y_{L-1} \\ 1-y_{L-1} \end{pmatrix} \quad \text{with} \quad \begin{cases} 0 \le \tau_j < \infty, \\ 0 \le y_j \le 1, \end{cases} \tag{4.36}$$

where the variables τ_j have the dimension of length and the y_j are dimensionless. The

L-loop eikonal diagram then becomes

$$F^{(L)} = C^{(L)} \prod_{j=1}^{L} \int_0^1 \mathrm{d}x_j \, P^{[\epsilon]}_{\ell_j r_j}(x_j) \, K(x_1, \ldots, x_L) \,, \tag{4.37}$$

where the infrared divergence of the diagram is now absorbed into the kernel

$$K(x_1, \ldots, x_L) = g^{2L} \Gamma(2L\epsilon) \left(\frac{\mu}{\Lambda}\right)^{2L\epsilon} \prod_{j=1}^{L-1} \int_0^1 \mathrm{d}y_j \, y_j^{-1+2j\epsilon} (1-y_j)^{-1+2\epsilon} \, \Theta\big(\{\boldsymbol{y}, \boldsymbol{x}\}\big) \,. \tag{4.38}$$

Here $\Theta\big(\{\boldsymbol{y}, \boldsymbol{x}\}\big)$ denotes the result of applying the substitutions eq. (4.36) to $\Theta(\boldsymbol{\rho}, \boldsymbol{x})$ in eq. (4.35). Here we have also regulated the infrared divergence in a gauge invariant way through the exponential damping factor $e^{-\Lambda \tau_L}$ with $\Lambda \ll 1$. Equation (4.38) contains in addition any potential ultraviolet sub-divergences of the diagram (generated by the nesting function $\Theta\big(\{\boldsymbol{y}, \boldsymbol{x}\}\big)$).

Having brought the L-loop eikonal diagram in the form of eq. (4.37), we can turn to extracting its imaginary part. Restricting our attention to the leading order in the dimensional regulator ϵ, we will drop the dependence of the soft propagators on ϵ,

$$F^{(L)} = C^{(L)} \prod_{j=1}^{L} \int_0^1 \mathrm{d}x_j \, P^{[0]}_{\ell_j r_j}(x_j) K(x_1, \ldots, x_L) + \mathcal{O}(\epsilon^{-D+1}) \,, \tag{4.39}$$

where D denotes the degree of divergence of the diagram, $F^{(L)} \sim \frac{1}{\epsilon^D} \times (\text{finite})$.

To compute the imaginary part of eq. (4.39), we start by observing that eq. (4.38) is manifestly purely real. As a result, the Feynman $i\eta$'s are the only source of imaginary parts of eq. (4.39). Each of the x_j-integration paths can therefore be decomposed into a principal-value part and small semicircles around the propagator poles. Given that the integrand takes purely imaginary values in the regions close to the poles and is real-valued on the remaining domain of integration, the resulting 2^L terms (each of which involves L integrations) will be either purely real or purely imaginary.

To collect the imaginary contributions, we define the cut propagator

$$\Delta_{ij}(x) = -\pi \, v_i \cdot v_j \, \delta\big((x v_i - (1-x) v_j)^2\big) \,, \tag{4.40}$$

and furthermore the p-fold cutting operator

$$\mathrm{Cut}_{x_{i_1}, \ldots, x_{i_p}} F^{(L)} = \prod_{\substack{j=1 \\ j \neq i_1, \ldots, i_p}}^{n} \mathrm{PV} \int_0^1 \mathrm{d}x_j \, P(x_j) \prod_{k=1}^{p} \int_0^1 \mathrm{d}x_{i_k} \, \Delta(x_{i_k}) \, K(x_1, \ldots, x_L) \,. \tag{4.41}$$

The action of this operator is to replace the p propagators that depend on the specified variables by delta functions and to place a principal-value prescription on the integrals

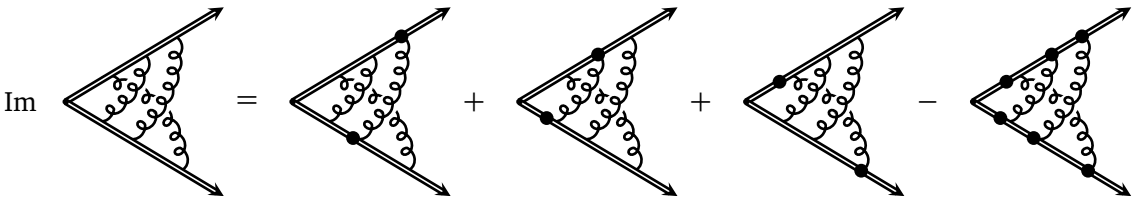

Figure 4.8: Schematic illustration of the formula (4.42) for the imaginary part of an eikonal diagram without internal vertices. The black dots at the endpoints of a soft-gluon propagator denote that the propagator has been cut—that is, replaced by a delta function. It is implied that the integrals over the attachment points of uncut soft propagators are principal-value integrals. The relative signs of the diagrams are determined by the factor i^{p-1}; each individual diagram displayed here corresponds to the action of the cutting operator (4.41) on the eikonal diagram.

over the remaining variables. To simplify notation, we dropped the indices on the (cut) propagators: $P(x_j) \equiv P^{[0]}_{\ell_j r_j}(x_j)$ and $\Delta(x_j) \equiv \Delta_{\ell_j r_j}(x_j)$.

The imaginary part of any L-loop eikonal diagram without internal vertices, to the leading order in ϵ, can then be written as

$$\mathrm{Im}\, F^{(L)} = \sum_{\substack{p=1 \\ p \text{ odd}}}^{L} \sum_{\substack{i_1,\ldots,i_p=1 \\ i_1<\cdots<i_p}}^{L} i^{\,p-1}\, \mathrm{Cut}_{x_{i_1},\ldots,x_{i_p}}\, F^{(L)} \,. \tag{4.42}$$

This formula is illustrated schematically in fig. 4.8 for a non-planar three-loop eikonal diagram ($L = 3$). Equation (4.42) is our master formula for the imaginary part and is applied to a variety of multi-loop eikonal diagrams in the next section.

4.4. Application to two- and three-loop eikonal diagrams

In this section we will demonstrate how eq. (4.42) is used in practice to compute the imaginary part of ladder-type eikonal diagrams. We discuss three different examples in section 4.4.1, 4.4.2 and 4.4.3, each of which provides insight into the position-space cutting prescription within a specific context.

For all the examples we keep the convention that all Wilson line velocities are outgoing, such that velocities associated with outgoing/incoming states have positive/negative time components, respectively. Ultraviolet divergences will be regulated by computing integrals in $d = 4 - 2\epsilon$ dimensions with $\epsilon > 0$, and infrared divergences are removed through an exponential damping factor. Collinear singularities are avoided by taking all Wilson line velocities to be timelike, $v_i^2 = 1$. An appropriate set of variables in terms of which to express integrated results is given by, for each cusp angle γ_{ij}, the exponential

$$\chi_{ij} = e^{-\gamma_{ij}} \,, \tag{4.43}$$

where the cusp angles are related to the Wilson line velocities through $\cosh\gamma_{ij} = |v_i \cdot v_j|$.

The results for all diagrams are verified by explicit computation of both sides of the cutting equation. In order to compute the imaginary part of the original diagrams, we will use the fact that the result for an eikonal diagram in timelike kinematics can be obtained from the spacelike result by analytic continuation of the cusp angle.

Recall that the soft propagator in eq. (4.34) takes the same form in spacelike and timelike kinematics when expressed in terms of $v_i \cdot v_j$, owing to our convention that all velocity vectors are outgoing. However, once expressed in terms of the relative angle $\gamma \equiv \gamma_{ij}$, it takes the respective forms

$$P_{ij}^{[0]}(x) = \begin{cases} \dfrac{-\cosh\gamma}{-x^2-(1-x)^2-2x(1-x)\cosh\gamma} & \text{for} \quad v_i\cdot v_j = -\cosh\gamma < 0\,, \\ \dfrac{\cosh\gamma}{-x^2-(1-x)^2+2x(1-x)\cosh\gamma+i\eta} & \text{for} \quad v_i\cdot v_j = \quad \cosh\gamma > 0\,, \end{cases} \tag{4.44}$$

where we dropped the $i\eta$ in the spacelike case, since the propagator roots are located outside the range $x \in [0,1]$. A comparison of these two expressions shows that we can map spacelike to timelike kinematics with the analytic continuation $-\cosh\gamma \to \cosh\gamma + i\eta$ or, equivalently in terms of $\chi = e^{-\gamma}$, with

$$\chi \;\longrightarrow\; -\frac{1}{\chi} - i\eta\,. \tag{4.45}$$

In the calculations of the following sections it will be useful to partial fraction the soft propagator in eq. (4.44) in order to solve for the roots of the denominator. The resulting expressions for the soft propagator and for the cut propagator in eq. (4.40) are

$$\begin{aligned} P_{ij}^{[0]}(x) &= \frac{R(\chi)}{2}\left(\frac{1}{x-\rho_1+i\eta} - \frac{1}{x-\rho_2-i\eta}\right)\,, \\ \Delta_{ij}(x) &= -\pi\frac{R(\chi)}{2}\Big(\delta(x-\rho_1)+\delta(x-\rho_2)\Big)\,, \end{aligned} \tag{4.46}$$

where $\chi \equiv \chi_{ij}$, the rational prefactor is $R(\chi) = \frac{1+\chi^2}{1-\chi^2} = \coth\gamma_{ij}$, and the denominator roots are given by

$$\big(\rho_1,\rho_2\big) = \begin{cases} \left(\frac{\chi}{\chi-1},\frac{1}{1-\chi}\right) & \text{for} \quad v_i\cdot v_j \;=\; -\cosh\gamma_{ij} < 0\,, \\ \left(\frac{\chi}{\chi+1},\frac{1}{\chi+1}\right) & \text{for} \quad v_i\cdot v_j \;=\; \cosh\gamma_{ij} > 0\,. \end{cases} \tag{4.47}$$

We note that in the upper case of eq. (4.47), the roots satisfy $0 < \rho_1 < \frac{1}{2} < \rho_2 < 1$, whereas in the lower case they satisfy $\rho_1 < 0$ and $\rho_2 > 1$. Since the delta functions are integrated in eq. (4.41) over the interval $x \in [0,1]$, we conclude that the eikonal diagram will only

have contributions to its imaginary part from channels with timelike kinematics $v_i \cdot v_j > 0$, in agreement with the causality considerations of section 4.2.1.

As we shall see, this observation is also in agreement with the relation between the imaginary part of an eikonal diagram and its discontinuities in various kinematic channels. Expressed in terms of the χ_{ij}-variables, the eikonal diagram has branch cuts located on the real line and satisfies Schwarz reflection, $F^{(L)}(\overline{\chi_{ij}}) = \overline{F^{(L)}(\chi_{ij})}$. Consequently the discontinuities of the diagram give rise to the imaginary part through the relation

$$2i \,\mathrm{Im}\, F^{(L)}(\boldsymbol{\chi}) = \sum_{j=1}^{L} \theta(v_{\ell_j} \cdot v_{r_j}) \,\mathrm{Disc}_{\chi_{\ell_j r_j}} F^{(L)}(\boldsymbol{\chi}) \,. \tag{4.48}$$

Here, the step functions account for the fact that the imaginary part has vanishing contributions from channels with spacelike kinematics $v_{\ell_j} \cdot v_{r_j} < 0$. An explicit example of this will be given in section 4.4.3, where we study a diagram that depends on two distinct cusp angles in purely timelike as well as mixed timelike and spacelike kinematics.

4.4.1. The non-planar two-loop ladder diagram

As a first example we consider the non-planar two-loop ladder diagram (see fig. 4.9). This diagram contains no sub-divergence and consequently has a simple pole in the dimensional regulator ϵ. In agreement with the discussion around eq. (4.48), this diagram will only have an imaginary part for timelike kinematics, $v_1 \cdot v_2 > 0$, so we restrict our attention to this case. Since the diagram contains only one cusp angle we will drop the subscripts and define $\cosh\gamma \equiv v_1 \cdot v_2$ as well as $\chi \equiv e^{-\gamma}$.

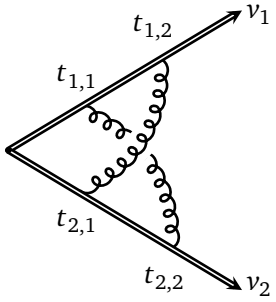

Figure 4.9: The non-planar two-loop ladder diagram.

The non-planar two-loop ladder diagram has the position-space representation

$$F^{(2)} = C^{(2)} \mu^{4\epsilon} \int_0^\infty \frac{\mathrm{d}t_{1,1}\,\mathrm{d}t_{1,2}\,\mathrm{d}t_{2,1}\,\mathrm{d}t_{2,2}\;\theta(t_{1,2}-t_{1,1})\,\theta(t_{2,2}-t_{2,1})(v_1\cdot v_2)^2}{\left[-(t_{1,1}v_1 - t_{2,2}v_2)^2 + i\eta\right]^{1-\epsilon}\left[-(t_{1,2}v_1 - t_{2,1}v_2)^2 + i\eta\right]^{1-\epsilon}}\,, \tag{4.49}$$

where the prefactor is given by $C^{(2)} = -\frac{g^4 C_F}{2N}\frac{\Gamma^2(d/2-1)}{16\pi^d}$. To compute the imaginary part of this diagram, the first task is to write it in the form of eq. (4.37). This can be achieved through

the change of variables in eq. (4.32), followed by that in eq. (4.36). Explicitly,

$$\begin{pmatrix} t_{1,1} \\ t_{2,2} \end{pmatrix} = \lambda \begin{pmatrix} x \\ 1-x \end{pmatrix}, \quad \begin{pmatrix} t_{1,2} \\ t_{2,1} \end{pmatrix} = \sigma \begin{pmatrix} y \\ 1-y \end{pmatrix}, \quad \begin{pmatrix} \lambda \\ \sigma \end{pmatrix} = \beta \begin{pmatrix} t \\ 1-t \end{pmatrix}. \tag{4.50}$$

After these transformations the diagram takes the desired form

$$F^{(2)} = C^{(2)} \int_0^1 \mathrm{d}x \int_0^1 \mathrm{d}y \; P_{12}^{[\epsilon]}(x) P_{12}^{[\epsilon]}(y) K(x,y). \tag{4.51}$$

where the kernel $K(x,y)$, upon the additional change of variable $u = \frac{t}{1-t}$, is given by

$$K(x,y) = \mu^{4\epsilon} \int_0^\infty \frac{\mathrm{d}\beta \, e^{-\Lambda\beta}}{\beta^{1-4\epsilon}} \int_0^\infty \mathrm{d}u \, u^{-1+2\epsilon} (u+1)^{-4\epsilon} \, \theta\left(\frac{y}{x} - u\right) \theta\left(u - \frac{1-y}{1-x}\right). \tag{4.52}$$

The effect of the first two transformations in eq. (4.50) is to leave each soft propagator dependent on a single variable, while the effect of the last change of variable is to extract the overall divergence of the diagram, as can be seen by comparing eqs. (4.49) and (4.51).

To facilitate the computation of the cuts of $F^{(2)}$ we will first evaluate the integral $K(x,y)$. The u-integral in eq. (4.52) may be performed in terms of the ${}_2F_1$ hypergeometric function: the primitive has the ϵ-expansion

$$f(u) = \frac{u^{2\epsilon}}{2\epsilon} \, {}_2F_1(2\epsilon, 4\epsilon; 1+2\epsilon; -u) = \frac{u^{2\epsilon}}{2\epsilon} \left(1 + \mathcal{O}(\epsilon^2)\right) = \frac{1}{2\epsilon} + \log u + \mathcal{O}(\epsilon), \tag{4.53}$$

and as a result $K(x,y)$ is given by

$$\begin{aligned} K(x,y) &= \Gamma(4\epsilon) \left(\frac{\mu}{\Lambda}\right)^{4\epsilon} \theta(y-x) \left[f\left(\frac{y}{x}\right) - f\left(\frac{1-y}{1-x}\right) \right] \\ &= \frac{1}{4\epsilon} \left(\frac{\mu}{\Lambda}\right)^{4\epsilon} \theta(y-x) \left[\log\left(\frac{y}{x}\right) - \log\left(\frac{1-y}{1-x}\right) \right] + \mathcal{O}(\epsilon^0). \end{aligned} \tag{4.54}$$

With this result for $K(x,y)$, the non-planar two-loop ladder diagram in eq. (4.51) can be expressed in the convenient form

$$F^{(2)} = \frac{C^{(2)}}{4\epsilon} \left(\frac{\mu}{\Lambda}\right)^{4\epsilon} \mathscr{F}^{(2)}, \tag{4.55}$$

where $\mathscr{F}^{(2)}$ is finite and its leading order in ϵ is given by

$$\mathscr{F}^{(2)} = \int_0^1 \mathrm{d}x \int_0^1 \mathrm{d}y \; P_{12}^{[0]}(x) P_{12}^{[0]}(y) \Big(\theta(y-x) - \theta(x-y)\Big) \log\left(\frac{y}{x}\right). \tag{4.56}$$

Notice that the integrand of $\mathscr{F}^{(2)}$ is manifestly symmetric under $x \longleftrightarrow y$, which is the result of a simple change of variables $(x,y) \mapsto (1-x, 1-y)$ on the second term.

Evaluation of cuts on the right-hand side of the cutting equation

The prefactor of $\mathscr{F}^{(2)}$ in eq. (4.55) is real, so it factors out on both sides of the cutting equation in eq. (4.42). This yields the following formula (see fig. 4.10),

$$\operatorname{Im}\mathscr{F}^{(2)} = \operatorname{Cut}_x \mathscr{F}^{(2)} + \operatorname{Cut}_y \mathscr{F}^{(2)}, \tag{4.57}$$

where Cut_x replaces the propagator depending on the specified variable by a delta function and introduces a principal-value prescription for the integral over the remaining variable, according to its definition in eq. (4.41). As a consequence of the observation below eq. (4.56), that the integrand of $\mathscr{F}^{(2)}$ is symmetric under the interchange of x and y, the two cuts are equal. So it is sufficient to compute $\operatorname{Cut}_x \mathscr{F}^{(2)}$, which is given by

$$\operatorname{Cut}_x \mathscr{F}^{(2)} = \int_0^1 \mathrm{d}x \,\mathrm{PV} \int_0^1 \mathrm{d}y \;\Delta_{12}(x)\, P_{12}^{[0]}(y) \Big(\theta(y-x) - \theta(x-y)\Big) \log\left(\frac{y}{x}\right). \tag{4.58}$$

The integral over x can be performed trivially due to the delta function. Inserting the expressions for $\Delta_{12}(x)$ and $P_{12}^{[0]}(y)$ given in eq. (4.46) and performing integral yields

$$\operatorname{Cut}_x \mathscr{F}^{(2)} = -\frac{\pi}{4} R(\chi)^2 \sum_{k=1}^{2} \mathrm{PV}\left(\int_{\rho_k}^1 \mathrm{d}y - \int_0^{\rho_k} \mathrm{d}y\right) \left(\tfrac{1}{y-\rho_1+i\eta} - \tfrac{1}{y-\rho_2-i\eta}\right) \log\left(\tfrac{y}{\rho_k}\right), \tag{4.59}$$

where the propagator roots $\rho_{1,2}$ are given in the lower case of eq. (4.47). The remaining integral over y do not immediately take the form of iterated integrals, due to the principle-value prescription. The strategy for their evaluation will be to write them as differences of iterated integrals, which in turn are readily expressible in terms of multiple polylogarithms. Basically, the principal-value integral is equal to the corresponding full integral minus the imaginary part of the integral.

Example 4.1. As a simple illustration, let us consider the following principal-value integral,

$$\mathrm{PV}\int_0^1 \frac{\mathrm{d}y}{y-\rho_1+i\eta} = \int_0^1 \frac{\mathrm{d}y}{y-\rho_1+i\eta} - i\,\operatorname{Im}\int_0^1 \frac{\mathrm{d}y}{y-\rho_1+i\eta}. \tag{4.60}$$

The first integral on the right-hand side of eq. (4.60) evaluates to $G(\rho_1;1)$, which is a weight-one multiple polylogarithm (see appendix A.1). Its imaginary part arises from the pole of the integrand and is extracted by localising the integration variable,

$$\operatorname{Im}\int_0^1 \frac{\mathrm{d}y}{y-\rho_1+i\eta} = -\pi \int_0^1 \mathrm{d}y\, \delta(y-\rho_1) = -\pi, \tag{4.61}$$

where we used in the last step that the pole is located inside the range of integration, in agreement with the discussion below eq. (4.47). We thus arrive at

$$\mathrm{PV}\int_0^1 \frac{\mathrm{d}y}{y-\rho_1+i\eta} = G(\rho_1;1) + i\pi. \tag{4.62}$$

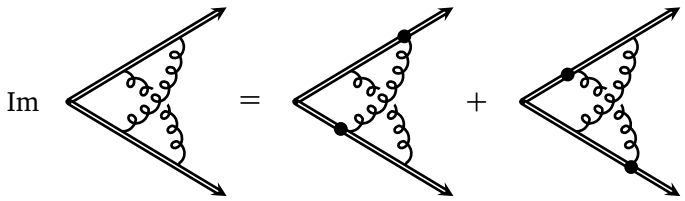

Figure 4.10: Graphical representation of the cutting prescription for the non-planar two-loop ladder stated in eq. (4.57). The black dots at the endpoints of a soft-gluon propagator indicate that the propagator has been replaced by a delta function. It is implied that the integrals over the attachment points of uncut soft propagators are principal-value integrals.

In the above example we could have computed the real part directly,

$$\mathrm{PV}\int_0^1 \frac{\mathrm{d}y}{y-\rho_1} = \mathrm{Re}\,G(\rho_1;1) = \mathrm{Re}\log\left(1-\tfrac{1}{\rho_1}\right) = \log\left|1-\tfrac{1}{\rho_1}\right| = \log\left(\tfrac{1}{\rho_1}-1\right). \tag{4.63}$$

However, an extension of this direct approach to higher-weight cases requires the use of a sequence of functional identities, which is case-dependent in practice and therefore not applicable in a systematic way. In contrast, the above method relies only on the construction of the imaginary part, which is derived systematically in appendix A.2.

Evaluating the principle-value integrals in eq. (4.59) according to this procedure results in the following expression for the cut in terms of multiple polylogarithms,

$$\begin{aligned}\mathrm{Cut}_x\,\mathscr{F}^{(2)} = -\frac{\pi}{4}R(\chi)^2\Big(&-2G(\rho_2,0;1)+2G(\rho_1,0;1)-2G(0,\rho_2;\rho_2)-2G(0,\rho_2;\rho_1)\\&+2G(0,\rho_1;\rho_2)+2G(0,\rho_1;\rho_1)+G(0;\rho_2)G(\rho_2;1)+G(0;\rho_1)G(\rho_2;1)\\&-G(0;\rho_2)G(\rho_1;1)-G(0;\rho_1)G(\rho_1;1)-2\pi i\,G(0;\tfrac{\rho_1}{\rho_2})\Big),\end{aligned} \tag{4.64}$$

where $G(\vec{a};x)$ for indices $\vec{a}$ and argument x is defined in eq. (A.1). We observe that in this expression the multiple polylogarithms depend on the propagator roots $\rho_k(\chi)$ through both their indices and their argument. This expression can be rewritten in terms of multiple polylogarithms with constant indices by exploiting the Hopf algebra structure of multiple polylogarithms [109–114]. We have described in detail in algorithm A.4 how this rewriting is performed and we have implemented the required steps to achieve the simplified functional form. The algorithm reduces eq. (4.64) to harmonic polylogarithms that can be further simplified into classical polylogarithms using eq. (A.5), which produces

$$\begin{aligned}\mathrm{Cut}_x\,\mathscr{F}^{(2)} &= -\pi R(\chi)^2\Big(-G(0,1;\chi)+G(0,0;\chi)-G(0,-1;\chi)-\frac{1}{2}\zeta_2\Big)\\&= -\frac{\pi}{2}R(\chi)^2\Big(\mathrm{Li}_2(\chi^2)+\log^2\chi-\zeta_2\Big).\end{aligned} \tag{4.65}$$

Inserting this elegant result for the cut into eq. (4.57) for the imaginary part of the two-loop

ladder, we finally obtain

$$\operatorname{Im} \mathscr{F}^{(2)} = -\pi R(\chi)^2 \left(\operatorname{Li}_2(\chi^2) + \log^2 \chi - \zeta_2\right), \tag{4.66}$$

The imaginary part of the original diagram $F^{(2)}$ is given by multiplying both sides of this equation by a real prefactor, see eq. (4.55), which completes the evaluation to the leading order in ϵ of the imaginary part of the non-planar two-loop ladder diagram.

Computation of imaginary part on the left-hand side of the cutting equation

We now proceed to verify the result in eq. (4.66), by computing the imaginary part of the non-planar two-loop ladder directly. This can be done by evaluating the diagram for spacelike kinematics $v_1 \cdot v_2 < 0$, in which case it will be purely real, subsequently perform the analytic continuation to timelike kinematics and collect the imaginary part of the latter.

The two-loop ladder is given by eq. (4.56), although we must keep in mind that for spacelike kinematics the propagator roots ρ_k are given by the upper case of eq. (4.47). Inserting the expressions for $P_{12}^{[0]}$ given in eq. (4.46), the diagram readily evaluates into multiple polylogarithms,

$$\widetilde{\mathscr{F}}^{(2)} = \frac{R(\chi)^2}{2}\big(G(\rho_1, 0, \rho_1; 1) - G(\rho_1, 0, \rho_2; 1) - G(\rho_2, 0, \rho_1; 1) + G(\rho_2, 0, \rho_2; 1)\big). \tag{4.67}$$

The tilde on the left-hand side serves to indicate that the expression on the right-hand side is only valid for spacelike kinematics. This is the second expression that features the roots ρ_k in the indices of multiple polylogarithms. Again we can use algorithm A.4 to recast this expression in terms of polylogarithms with constant indices. In fact, the two-loop ladder diagram reduces to classical polylogarithms,

$$\begin{aligned}\widetilde{\mathscr{F}}^{(2)} &= R(\chi)^2 \left(2G(0,1,0;\chi) - 2G(0,0,0;\chi) + 2G(0,-1,0;\chi) - \zeta_2 G(0;\chi) - \zeta_3\right) \\ &= R(\chi)^2 \left(\operatorname{Li}_3(\chi^2) - \log\chi \operatorname{Li}_2(\chi^2) - \tfrac{1}{3}\log^3\chi - \zeta_2 \log\chi - \zeta_3\right).\end{aligned} \tag{4.68}$$

We can now construct the result for the two-loop ladder diagram in timelike kinematics by performing the analytic continuation $\chi \to -1/\chi - i\eta$ on eq. (4.68). Applying this analytic continuation to the classical polylogarithms is straightforward. For example,

$$\begin{aligned}\operatorname{Li}_2(\chi^2) &\to -\operatorname{Li}_2(\chi^2) - 2\log^2\chi + 2\zeta_2 - 2\pi i \log\chi\,, \\ \operatorname{Li}_3(\chi^2) &\to \operatorname{Li}_3(\chi^2) + \tfrac{4}{3}\log^3\chi - 4\zeta_2\log\chi + 2\pi i \log^2\chi\,.\end{aligned} \tag{4.69}$$

Applying these analytic continuations to eq. (4.68) we find the following result for the non-planar two-loop ladder with timelike kinematics,

$$\begin{aligned}\mathscr{F}^{(2)} = R(\chi)^2 \Big(&\operatorname{Li}_3(\chi^2) - \log\chi \operatorname{Li}_2(\chi^2) - \tfrac{1}{3}\log^3\chi + 5\zeta_2\log\chi - \zeta_3 \\ &- i\pi\big(\operatorname{Li}_2(\chi^2) + \log^2\chi - \zeta_2\big)\Big).\end{aligned} \tag{4.70}$$

The imaginary part of $\mathscr{F}^{(2)}$ in this expression fully agrees with the result found in eq. (4.66), arising from the sum of cut diagrams. We can therefore conclude that the cutting prescription for the two-loop ladder, stated in eq. (4.57), is correct.

4.4.2. Three-loop non-planar ladder diagram

In this section we consider the three-loop ladder diagram, see fig. 4.11, to demonstrate that the principal-value integrals in cut diagrams can indeed be evaluated in non-trivial cases. The three-loop ladder diagram also represents an example of an eikonal diagram with multiple-cut contributions to its imaginary part, in the case at hand a triple cut, as prescribed by eq. (4.41). As in the previous section, we take $\cosh\gamma \equiv v_1 \cdot v_2 > 0$ in order to have a non-vanishing imaginary part and we will express our results in terms of $\chi \equiv e^{-\gamma}$.

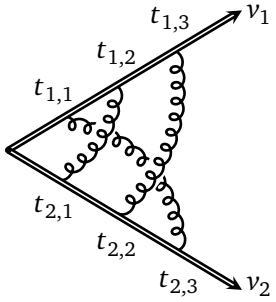

Figure 4.11: A three-loop non-planar ladder diagram.

The position-space representation of the diagram in fig. 4.11 takes the form

$$F^{(3)} = C^{(3)}\mu^{6\epsilon}\int_0^\infty \left(\prod_{i=1}^{2}\prod_{j=1}^{3}\mathrm{d}t_{i,j}\right)\frac{\prod_{i,j=1}^{2}\theta(t_{i,j+1}-t_{i,j})(v_1\cdot v_2)^3}{D(t_{1,1},t_{2,3})\,D(t_{1,2},t_{2,1})\,D(t_{1,3},t_{2,2})}\,, \tag{4.71}$$

where $D(t_1,t_2) = \left[-(t_1v_1 - t_2v_2)^2 + i\eta\right]^{1-\epsilon}$. To compute the imaginary part of this diagram, we first bring it into the form of eq. (4.37). This is achieved through the changes of variables in eq. (4.32) (with $t_{\ell_j,m_j} = t_{1,j}$), followed by the sequence of substitutions in eq. (4.36). For convenience we use the notation $(x_1,x_2,x_3) = (x,y,z)$ and $(y_1,y_2) = (t,u)$. After these transformations, the diagram becomes

$$F^{(3)} = C^{(3)}\int_0^1 \mathrm{d}x\,\mathrm{d}y\,\mathrm{d}z\,P_{12}^{[\epsilon]}(x)\,P_{12}^{[\epsilon]}(y)\,P_{12}^{[\epsilon]}(z)\,K(x,y,z)\,, \tag{4.72}$$

where the kernel is given, after integrating out the overall scale, by

$$\begin{aligned}K(x,y,z) = \Gamma(6\epsilon)\left(\frac{\mu}{\Lambda}\right)^{6\epsilon}&\int_0^1 \mathrm{d}t\;t^{-1+2\epsilon}(1-t)^{-1+2\epsilon}\int_0^1 \mathrm{d}u\;u^{-1+4\epsilon}(1-u)^{-1+2\epsilon}\\ &\times\theta\left(\tfrac{z}{y}-\tfrac{(1-t)u}{1-u}\right)\theta\left(\tfrac{y}{x}-\tfrac{t}{1-t}\right)\theta\left(\tfrac{tu}{1-u}-\tfrac{1-z}{1-x}\right)\theta\left(\tfrac{1-z}{1-y}-\tfrac{(1-t)u}{1-u}\right).\end{aligned} \tag{4.73}$$

We are interested in the leading order in ϵ of this expression. Owing to the step functions, whose arguments simplify after rescaling the integration variables according to $\frac{t}{1-t} \mapsto t$ and $\frac{u}{1-u} \mapsto u$, the integrals over t and u are finite. After setting ϵ to zero in the u-integral, performing the t-integral in terms of hypergeometric functions and subsequently expanding in ϵ, we obtain the following expression, valid to the leading order in ϵ,

$$\begin{aligned} K(x,y,z) &= \frac{1}{6\epsilon}\left(\frac{\mu}{\Lambda}\right)^{6\epsilon}\left[\,\theta(y-z)\theta(z-x)\tfrac{1}{2}\log^2\left(\frac{1-x}{x}\frac{z}{1-z}\right)+(y\longleftrightarrow z)\,\right] \\ &\equiv \frac{1}{6\epsilon}\left(\frac{\mu}{\Lambda}\right)^{6\epsilon}\,\mathscr{K}(x,y,z), \end{aligned} \tag{4.74}$$

We observe that eq. (4.74) is symmetric under the interchange of y and z. This observation implies that $\mathrm{Cut}_y F^{(3)} = \mathrm{Cut}_z F^{(3)}$, which reduces the number of independent cuts to be computed.

The computation of the cuts of the three-loop ladder diagram is performed conveniently in terms of $\mathscr{F}^{(3)}$, defined as the coefficient of the $1/\epsilon$ pole of the diagram,

$$F^{(3)} = \frac{C^{(3)}}{6\epsilon}\left(\frac{\mu}{\Lambda}\right)^{6\epsilon}\mathscr{F}^{(3)}. \tag{4.75}$$

The function $\mathscr{F}^{(3)}$ is finite and an explicit expression, to leading order in ϵ, is given by

$$\mathscr{F}^{(3)} = \int_0^1 \mathrm{d}x\,\mathrm{d}y\,\mathrm{d}z\,P_{12}^{[0]}(x)\,P_{12}^{[0]}(y)\,P_{12}^{[0]}(z)\,\mathscr{K}(x,y,z). \tag{4.76}$$

Computation of imaginary part on the left-hand side of the cutting equation

The cutting equation for $\mathscr{F}^{(3)}$, which follows upon inserting eq. (4.75) into eq. (4.42), is

$$\mathrm{Im}\,\mathscr{F}^{(3)} = \mathrm{Cut}_x\,\mathscr{F}^{(3)} + \mathrm{Cut}_y\,\mathscr{F}^{(3)} + \mathrm{Cut}_z\,\mathscr{F}^{(3)} - \mathrm{Cut}_{x,y,z}\,\mathscr{F}^{(3)}. \tag{4.77}$$

Here, the last terms on the right-hand side is a triple-cut contribution. Obviously this feature appears only in ladder diagrams that contain three or more loops. Incidentally, the diagram $F^{(3)}$ is the only three-loop ladder diagram with an $\mathscr{O}\left(\epsilon^{-1}\right)$ divergence that has a non-vanishing triple cut, see fig. 4.12, and therefore it provides an excellent example to demonstrate a multiple-cut contribution.

We start the computation of the cuts by evaluating the triple cut. Since as all three integrations in eq. (4.76) become localized by delta functions, this cut is readily computed,

$$\begin{aligned} \mathrm{Cut}_{x,y,z}\,\mathscr{F}^{(3)} &= \int_0^1 \mathrm{d}x\,\mathrm{d}y\,\mathrm{d}z\,\Delta_{12}(x)\,\Delta_{12}(y)\,\Delta_{12}(z)\,\mathscr{K}(x,y,z) \\ &= -\frac{\pi^3}{8}R(\chi)^3\sum_{k,l,m=1}^{2}\mathscr{K}(\rho_k,\rho_l,\rho_m), \end{aligned} \tag{4.78}$$

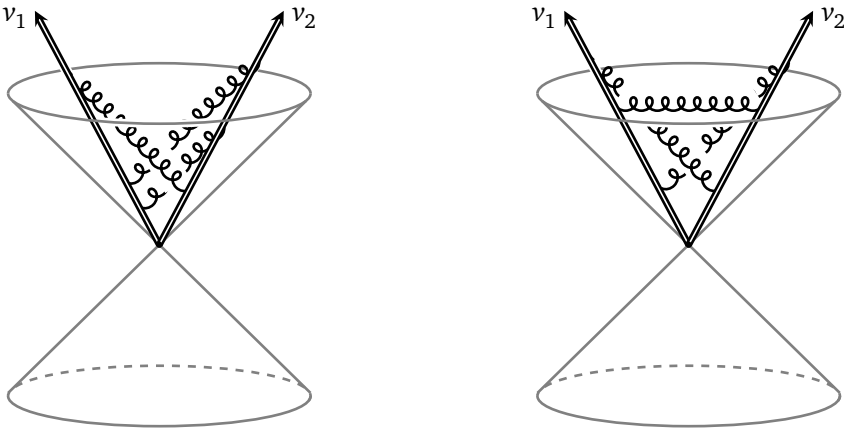

(a) (b)

Figure 4.12: Triple cut of the two three-loop diagrams that have a single pole divergence. In (a) the non-vanishing triple cut of $F^{(3)}$ is illustrated by the exchange of three lightlike gluons. In contrast, (b) shows graphically that the triple cut of the maximally crossed diagram vanishes, because the three gluons cannot simultaneously be aligned with the light cone.

where the roots $\rho_{1,2}$ are given by the lower case in eq. (4.47). An inspection of the explicit expression for $\mathscr{K}(\rho_k, \rho_l, \rho_m)$ reveals that it is non-zero if and only if $(k,l,m) = (1,2,2)$. Indeed, in the first term of eq. (4.74), the logarithm is non-zero only when $k \neq m$, while the step functions dictate that $\rho_k \leq \rho_m \leq \rho_l$. Since $\rho_1 < \rho_2$, we must therefore have $k = 1$ and $l = m = 2$. An identical argument applies to the second term of eq. (4.74), producing the simple result

$$\mathrm{Cut}_{x,y,z}\, \mathscr{F}^{(3)} = -\frac{\pi^3}{2} R(\chi)^3 \log^2 \chi\,. \tag{4.79}$$

This completes the evaluation of the triple-cut contribution to eq. (4.77).

The single cuts feature of mix of delta functions and principal-value prescriptions. Here we focus on the contribution $\mathrm{Cut}_x\, \mathscr{F}^{(3)}$, since the remaining cuts are computed completely analogously. (In fact, only one additional single cut needs to be computed, because we already know that $\mathrm{Cut}_y\, \mathscr{F}^{(3)} = \mathrm{Cut}_z\, \mathscr{F}^{(3)}$.) Using the partial-fractioned expressions for Δ_{12} and $P_{12}^{[0]}$ in eq. (4.46) and integrating out the delta function we find

$$\begin{aligned}
\mathrm{Cut}_x\, \mathscr{F}^{(3)} &= \int_0^1 \mathrm{d}x\, \mathrm{PV} \int_0^1 \mathrm{d}y\, \mathrm{PV} \int_0^1 \mathrm{d}z\; \Delta_{12}(x) P_{12}^{[0]}(y) P_{12}^{[0]}(z)\, \mathscr{K}(x,y,z) \\
&= -\frac{\pi}{8} R(\chi)^3 \sum_{k=1}^{2} \mathrm{PV} \int_{\rho_k}^1 \mathrm{d}y \left(\tfrac{1}{y-\rho_1} - \tfrac{1}{y-\rho_2}\right) \mathrm{PV} \int_{\rho_k}^y \mathrm{d}z \left(\tfrac{1}{z-\rho_1} - \tfrac{1}{z-\rho_2}\right) \log^2\left(\tfrac{1-\rho_k}{\rho_k} \tfrac{z}{1-z}\right),
\end{aligned} \tag{4.80}$$

where the regulating $\pm i\eta$ were dropped for notational convenience. The resulting principal-value integrals may be evaluated as the corresponding full integrals minus the imaginary part, for which formulas are listed in appendix A.2. The innermost PV integral thus gives rise to step functions involving the variables ρ_1, ρ_2 and y. Splitting the remaining y-integral

in the $k=1$ term into two integrals with the respective domains $[\rho_1,\rho_2]$ and $[\rho_2,1]$ allows all step functions to be resolved. Ultimately, the cut is found to evaluate to

$$\begin{aligned}\mathrm{Cut}_x\,\mathscr{F}^{(3)} = \frac{\pi}{2}R(\chi)^3\Big[-\tfrac{1}{3}\log^4\chi+\log^2\chi\Big(H_2(\chi^2)-3\zeta_2\Big)-2\log\chi\Big(H_3(\chi^2)-\zeta_3\Big)\\ +H_{2,2}(\chi^2)+2H_4(\chi^2)-\zeta_2H_2(\chi^2)-\tfrac{1}{4}\zeta_4\Big]\,.\end{aligned} \tag{4.81}$$

This result is expressed in terms of harmonic polylogarithms, which are defined in eq. (A.6). Similarly, the y- and z-cuts are found to evaluate to

$$\begin{aligned}\mathrm{Cut}_y\,\mathscr{F}^{(3)} = \mathrm{Cut}_z\,\mathscr{F}^{(3)} = \frac{\pi}{4}R(\chi)^3\Big[-\tfrac{1}{3}\log^4\chi+\log^2\chi\Big(H_2(\chi^2)+3\zeta_2\Big)\\ +2H_{3,1}(\chi^2)+H_{2,2}(\chi^2)-\zeta_2H_2(\chi^2)+\tfrac{5}{4}\zeta_4\Big]\,.\end{aligned} \tag{4.82}$$

Combining all single and triple cuts according to eq. (4.77) thus yields the imaginary part,

$$\begin{aligned}\mathrm{Im}\,\mathscr{F}^{(3)} = \pi R(\chi)^3\Big[-\tfrac{1}{3}\log^4\chi+\log^2\chi\Big(H_2(\chi^2)+3\zeta_2\Big)-\log\chi\Big(H_3(\chi^2)-\zeta_3\Big)\\ +H_{3,1}(\chi^2)+H_{2,2}(\chi^2)+H_4(\chi^2)-\zeta_2H_2(\chi^2)+\tfrac{1}{2}\zeta_4\Big]\,.\end{aligned} \tag{4.83}$$

Evaluation of imaginary part on the left-hand side of the cutting equation

As a crosscheck of this result, we now proceed to compute the imaginary part of the three-loop ladder by evaluating the diagram for spacelike kinematics $v_1\cdot v_2<0$, perform the analytic continuation to timelike kinematics and collect the imaginary part.

The three-loop ladder is given by eq. (4.76) to the leading order in ϵ. Inserting the expressions for $P_{12}^{[0]}$ and $\mathscr{K}(x,y,z)$ given in eqs. (4.46) and (4.74), respectively, the three-fold integrals evaluate into weight-five multiple polylogarithms,

$$\tilde{\mathscr{F}}^{(3)} = \frac{R(\chi)^3}{4}\sum_{i,j,k,l,m=0,1}(-1)^{i+j+k+l+m}G(\rho_{i+1},\rho_{j+1},k,l,\rho_{m+1};1)\,, \tag{4.84}$$

where the tilde on the left-hand side indicates that the diagram is computed for spacelike kinematics and where the propagator roots ρ_k are equal to the upper case of eq. (4.47). Using the algorithm A.4 to recast this representation in terms of multiple polylogarithms with constant indices, the three-loop ladder diagram is in fact expressible in terms of har-

monic polylogarithms,

$$\begin{aligned}\widetilde{\mathscr{F}}^{(3)} = \frac{R(\chi)^3}{4}\Big[&-\tfrac{4}{15}\log^5\chi + \tfrac{4}{3}\log^3\chi\left(H_2(\chi^2)-\zeta_2\right) - 2\log^2\chi\left(H_3(\chi^2)-\zeta_3\right)\\ &+4\log\chi\left(H_{3,1}(\chi^2)+H_{2,2}(\chi^2)+H_4(\chi^2)+\zeta_2 H_2(\chi^2)+\tfrac{3}{2}\zeta_4\right)\\ &-6H_{4,1}(\chi^2)-6H_{3,2}(\chi^2)-4H_{2,3}(\chi^2)-6H_5(\chi^2)-2\zeta_2 H_3(\chi^2)\\ &+4\zeta_3 H_2(\chi^2)+3\zeta_5+2\zeta_2\zeta_3\Big]. \end{aligned} \tag{4.85}$$

We have checked this expression for the diagram in spacelike kinematics with previous results in refs. [98, 104], finding complete agreement[4].

The result for the three-loop ladder diagram in timelike kinematics is obtained after performing the analytic continuation $\chi \to -1/\chi - i\eta$ on eq. (4.85). The harmonic polylogarithms, in particular, transform as

$$H_{\vec{a}}(\chi^2) \to H_{\vec{a}}(1/\chi^2 + i\eta). \tag{4.86}$$

The resulting harmonic polylogarithms are evaluated slightly above the branch cut $[1,\infty)$ and may in turn be expressed in terms of $H_{\vec{a}}(\chi^2)$ and $\log\chi$ using the `Mathematica` package `HPL` [115, 116]. This produces the three-loop ladder diagram with timelike kinematics,

$$\begin{aligned}\mathscr{F}^{(3)} = -\frac{R(\chi)^3}{4}\Big[&\tfrac{4}{15}\log^5\chi - \tfrac{4}{3}\log^3\chi\left(H_2(\chi^2)+11\zeta_2\right) + 2\log^2\chi\left(H_3(\chi^2)-\zeta_3\right)\\ &-4\log\chi\left(H_{3,1}(\chi^2)+H_{2,2}(\chi^2)+H_4(\chi^2)-5\zeta_2 H_2(\chi^2)-\tfrac{27}{2}\zeta_4\right)\\ &+6H_{4,1}(\chi^2)+6H_{3,2}(\chi^2)+4H_{2,3}(\chi^2)+6H_5(\chi^2)-10\zeta_2 H_3(\chi^2)\\ &-4\zeta_3 H_2(\chi^2)-3\zeta_5+10\zeta_2\zeta_3\\ &+4\pi i\Big(\tfrac{1}{3}\log^4\chi-\log^2\chi\left(H_2(\chi^2)+3\zeta_2\right)+\log\chi\left(H_3(\chi^2)-\zeta_3\right)\\ &\qquad -H_{3,1}(\chi^2)-H_{2,2}(\chi^2)-H_4(\chi^2)+\zeta_2 H_2(\chi^2)-\tfrac{1}{2}\zeta_4\Big)\Big]. \end{aligned} \tag{4.87}$$

The imaginary part of this expression agrees with the result found in eq. (4.83), so we can conclude that the cutting prescription for the three-loop ladder correctly produces the imaginary part.

[4] More specifically, adding the diagram in fig. 4.11 to the maximally-crossed three-loop ladder, which we have computed by the same methods, we find agreement with eq. (A.1) of ref. [104]. Furthermore, according to eq. (4.26) in ref. [98], the two color structures of the (3,3) web are linear combinations of these two diagrams. Inserting our results for the two diagrams, we recover the color structures in their eqs. (4.29) and (4.33), thereby cross-checking the results for both diagrams individually, and in particular our eq. (4.85) for the three-loop non-planar ladder.

4.4.3. Two-loop web with three Wilson lines

The formalism of section 4.3 allows to compute the imaginary part of eikonal diagrams to the leading order in ϵ. This may appear to limit its applicability, but in practice a large class of diagrams have only simple poles in ϵ, whose coefficient contributes to physical observables of interest, such as the cusp anomalous dimension in eq. (4.20). In fact, the cusp anomalous dimension can be expressed entirely in terms of diagrams with simple poles in ϵ, once the coupling constants are renormalized. For Abelian gauge theories this can be inferred from eq. (4.19). The statement also holds for non-Abelian gauge theories, owing to the non-Abelian exponentiation theorem for two Wilson lines. This theorem states that the two-line correlator can be written as the exponential of *webs*: the eikonal diagrams that are eikonal-line two-particle irreducible[5] [73, 74].

Over the past six years, non-Abelian exponentiation has been shown to generalize to correlators of an *arbitrary* number of Wilson lines [75, 100, 117–121]. This generalized non-Abelian exponentiation theorem states that the correlator of an arbitrary number of Wilson lines is given as the exponential of the sum of webs,

$$\left\langle \Phi_{v_1} \cdots \Phi_{v_n} \right\rangle = \exp\left(\sum_{i \in \{\text{webs}\}} C_i^T R_i \mathscr{F}_i \right), \tag{4.88}$$

where a web is defined as a *collection* of diagrams that are mutually related by permutations of the order of gluon attachments. The webs contribute to the exponent through the (vector of) color factors C_i and kinematical factors $\mathscr{F}_i$ of their constituent diagrams, weighted by means of a web mixing matrix R_i. The web mixing matrices can be computed systematically with the help of the replica trick of statistical mechanics [85, 117]. Among several properties, they satisfy the zero-sum-row condition, $\sum_b R_{ab} = 0$, which ensures that the symmetric linear combination of the constituent diagrams is projected out [119]. The mixing matrices also satisfy a weighted zero-sum column condition which ensures that the leading divergence of the constituent diagrams of a web conspire to cancel when the diagrams are combined into the web. This is a general feature of webs, ultimately following from their renormalization properties [100, 117, 118]. Further cancellations of non-leading divergences can be achieved by constructing *subtracted webs* [97], which incorporate commutators of lower-loop webs (computed at subleading order in ϵ). Subtracted webs have an $\mathcal{O}(\epsilon^{-1})$ divergence and, as such, they contribute directly to the soft anomalous dimension, without any further cancellation of poles. In this respect webs are particularly amenable to the position space cutting formalism.

As an example, we consider in this section the $(1, 2, 1)$ web in fig. 4.13. The labels of the web refer to the number of gluon attachments on each eikonal line, and the two diagrams are related by permutations of the attachment points, where the permutations act on each line separately. Although the individual diagrams in fig. 4.13 are clearly not eikonal-line

[5] Eikonal-line two-particle irreducible means that the set of gluon propagators in a web cannot be partitioned without cutting at least one of the gluon propagators. Gluons that cross each other count as connected lines.

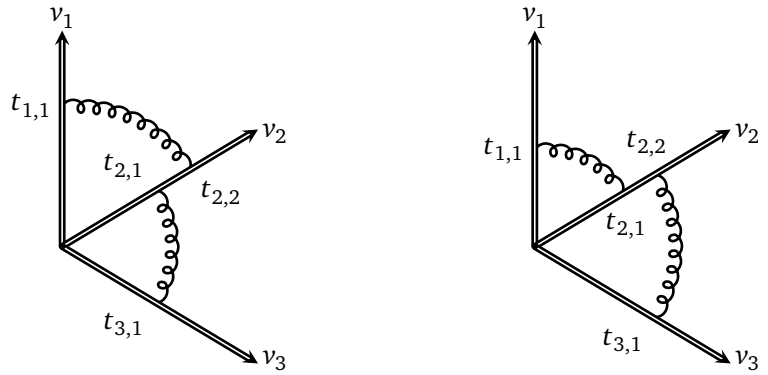

Figure 4.13: The two diagrams constituting the $(1,2,1)$ web. The antisymmetric combination of the two diagrams is not captured by exponentiation of the one-loop sub-diagrams, and this linear combination of the diagrams, defining the web, appears in the exponent. Diagram (a) is given by $C_{\mathrm{a}}\mathscr{F}_{\mathrm{a}}$, split into the color and kinematic factors, and likewise for (b).

two-particle irreducible, their contributions are not entirely reproduced by exponentiation of their one-loop sub-diagrams (as would be the case for contributions to a two-Wilson line correlator). Indeed, the sum of the one-loop sub-diagrams spanned by the pairs of lines $\{v_1, v_2\}$ and $\{v_2, v_3\}$ will appear in the exponent, but upon expanding the exponential to second order, these sub-diagrams only reproduce the symmetric linear combination of the two-loop diagrams. To compensate, the antisymmetric linear combination of the two-loop diagrams, which defines the web, must be added to the exponent as a contribution. Denoting the color and kinematical factors of the diagrams in fig. 4.13 by $C_{\mathrm{a,b}}$ and $\mathscr{F}_{\mathrm{a,b}}$, the web is accordingly defined as

$$W^{(2)}_{(1,2,1)} = \left(C_{\mathrm{a}}, C_{\mathrm{b}}\right) \begin{pmatrix} \frac{1}{2} & -\frac{1}{2} \\ -\frac{1}{2} & \frac{1}{2} \end{pmatrix} \begin{pmatrix} \mathscr{F}_{\mathrm{a}} \\ \mathscr{F}_{\mathrm{b}} \end{pmatrix} = \frac{1}{2}(C_{\mathrm{a}} - C_{\mathrm{b}})(\mathscr{F}_{\mathrm{a}} - \mathscr{F}_{\mathrm{b}}). \tag{4.89}$$

To illustrate the cutting procedure for webs, let us prepare the web $W^{(2)}_{(1,2,1)}$ for the computation of its imaginary part. In analogy with the previous two examples, we take $\cosh\gamma_{12} \equiv v_1 \cdot v_2 > 0$ and $\cosh\gamma_{23} \equiv v_2 \cdot v_3 > 0$, in order to have a non-vanishing contribution to the imaginary part from both channels. We will express our results in terms of the variables $\chi \equiv e^{-\gamma_{12}}$ and $\psi \equiv e^{-\gamma_{23}}$. The first task will be to show that the leading $\mathscr{O}(\epsilon^{-2})$ divergences of the individual diagrams cancel out, leaving an $\mathscr{O}(\epsilon^{-1})$ divergence. We will then be ready to apply the position-space cutting prescription directly to the web.

Let us first consider diagram (a) in fig. 4.13. Its kinematical factor is given by

$$\mathscr{F}_{\mathrm{a}} = C^{(2)}\mu^{4\epsilon}\int_0^\infty \frac{\mathrm{d}t_{1,1}\,\mathrm{d}t_{2,1}\,\mathrm{d}t_{2,2}\,\mathrm{d}t_{3,1}\;\theta(t_{2,2}-t_{2,1})(v_1\cdot v_2)(v_2\cdot v_3)}{\left[-(t_{1,1}v_1 - t_{2,2}v_2)^2 + i\eta\right]^{1-\epsilon}\left[-(t_{2,1}v_2 - t_{3,1}v_3)^2 + i\eta\right]^{1-\epsilon}}, \tag{4.90}$$

where $C^{(2)}$ collects irrelevant constants, but no color factor. The overall divergence of these integrals can be extracted through the changes of variables in eqs. (4.32) and (4.36). After

these transformations, the kinematical factor takes the form

$$\mathscr{F}_{\mathrm{a}} = C^{(2)} \int_0^1 \mathrm{d}x\, \mathrm{d}y\, P_{12}^{[\epsilon]}(x)\, P_{23}^{[\epsilon]}(y)\, K(x,y)\,, \tag{4.91}$$

where the kernel is given by

$$\begin{aligned} K(x,y) &= \mu^{4\epsilon} \int_0^\infty \frac{\mathrm{d}\rho_1\, \mathrm{d}\rho_2}{(\rho_1\rho_2)^{1-2\epsilon}}\, \theta(\rho_1 x - \rho_2 y) \\ &= \frac{\Gamma(4\epsilon)}{2\epsilon} \left(\frac{\mu}{\Lambda}\right)^{4\epsilon} \Big[u^{2\epsilon}\, {}_2F_1(2\epsilon, 4\epsilon; 1+2\epsilon; -u) \Big]_{u=y/x}^{u=\infty}. \end{aligned} \tag{4.92}$$

An analogous computation for the second diagram in the web, $\mathscr{F}_{\mathrm{b}}$, would lead to a result that differs only in the step function, which reads $\theta(\rho_2 y - \rho_1 x)$ and changes the lower integration bound in eq. (4.92) from y/x into x/y. After expanding the gamma function and the hypergeometric function in ϵ, the kinematical factor of the $(1,2,1)$ web in eq. (4.89) therefore takes the form

$$\mathscr{F}_{\mathrm{a}} - \mathscr{F}_{\mathrm{b}} = \frac{C^{(2)}}{8\epsilon^2} \left(\frac{\mu}{\Lambda}\right)^{4\epsilon} \int_0^1 \mathrm{d}x\, \mathrm{d}y\, P_{12}^{[\epsilon]}(x)\, P_{23}^{[\epsilon]}(y) \left[\left(\frac{x}{y}\right)^{2\epsilon} - \left(\frac{y}{x}\right)^{2\epsilon} \right] \big(1 + \mathscr{O}(\epsilon^2)\big)\,. \tag{4.93}$$

After expanding the expression in square brackets in ϵ, the leading poles of the separate diagrams cancel, leaving an $\mathscr{O}(\epsilon^{-1})$ divergence, in agreement with the previous discussions in this section. If we factor out the remaining pole, then we can write the web in the convenient form

$$W_{(1,2,1)}^{(2)} = \frac{C_{\mathrm{a}} - C_{\mathrm{b}}}{2}\, \frac{C^{(2)}}{2\epsilon} \left(\frac{\mu}{\Lambda}\right)^{4\epsilon} \mathscr{F}_{(1,2,1)}^{(2)}\,, \tag{4.94}$$

where $\mathscr{F}_{(1,2,1)}^{(2)}$ is finite and is given to the leading order in ϵ by

$$\mathscr{F}_{(1,2,1)}^{(2)} = \int_0^1 \mathrm{d}x\, \mathrm{d}y\, P_{12}^{[0]}(x)\, P_{23}^{[0]}(y)\, \log\left(\frac{x}{y}\right). \tag{4.95}$$

Computation of imaginary part on the left-hand side of the cutting equation

The cutting equation for the web reduces to a cutting equation for $\mathscr{F}_{(1,2,1)}^{(2)}$, since the overall prefactor in eq. (4.94) is real. This yields the formula

$$\mathrm{Im}\, \mathscr{F}_{(1,2,1)}^{(2)} = \mathrm{Cut}_x\, \mathscr{F}_{(1,2,1)}^{(2)} + \mathrm{Cut}_y\, \mathscr{F}_{(1,2,1)}^{(2)}\,. \tag{4.96}$$

More explicitly, by inserting the definition of the operator Cut_{x_i} (see eq. (4.41)), we have

$$\begin{aligned}\mathrm{Im}\,\mathscr{F}^{(2)}_{(1,2,1)} = &\int_0^1 \mathrm{d}x\ \mathrm{PV}\int_0^1 \mathrm{d}y\ \Delta_{12}(x)\,P^{[0]}_{23}(y)\,\log\left(\frac{x}{y}\right)\\ &+\mathrm{PV}\int_0^1 \mathrm{d}x\int_0^1 \mathrm{d}y\ P^{[0]}_{12}(x)\,\Delta_{23}(y)\,\log\left(\frac{x}{y}\right).\end{aligned} \tag{4.97}$$

In this expression, the second term is equal to the first term (up to a sign) with the two cusp angles and integration variables interchanged. As a result, the imaginary part of the web is antisymmetric under the interchange $\gamma_{12}\leftrightarrow\gamma_{23}$. This observation allows us to write the imaginary part in a manifestly antisymmetric form

$$\mathrm{Im}\,\mathscr{F}^{(2)}_{(1,2,1)} = J(\chi,\psi) - J(\psi,\chi), \tag{4.98}$$

where the auxiliary function $J(\chi,\psi)$ is defined as the first term of eq. (4.97),

$$J(\chi,\psi) = \int_0^1 \mathrm{d}x\,\mathrm{PV}\int_0^1 \mathrm{d}y\ \Delta_{12}(x)\,P^{[0]}_{23}(y)\,\log\left(\frac{x}{y}\right). \tag{4.99}$$

The evaluation of the imaginary part of the web thus amounts to the evaluation of the integral $J(\chi,\psi)$. It can be computed by inserting the partial-fractioned expressions for Δ_{12} and $P^{[0]}_{23}$, which are given in eq. (4.46) and which read

$$\begin{aligned}\Delta_{12}(x) &= -\pi\frac{R(\chi)}{2}\Big(\delta\big(x-\rho_1(\chi)\big)+\delta\big(x-\rho_2(\chi)\big)\Big),\\ P^{[0]}_{23}(y) &= \frac{R(\psi)}{2}\left(\frac{1}{y-\rho_1(\psi)+i\eta}-\frac{1}{y-\rho_2(\psi)-i\eta}\right),\end{aligned} \tag{4.100}$$

in terms of the two distinct kinematical invariants χ and ψ.

The integration over the delta function in eq. (4.99) becomes trivial, leaving a single principal-value integral to be evaluated. The principal-value integral can be computed, as in the previous two examples, by evaluating the corresponding full integral minus its imaginary part. In the following, we assume without loss of generality that $\psi<\chi$, which fixes $\rho_1(\chi)<\rho_1(\psi)<\rho_2(\psi)<\rho_2(\chi)$ and allows the step functions in the relevant eqs. (A.13)–(A.16) to be resolved. In this way, we find that

$$\begin{aligned}J(\chi,\psi) &= -\frac{\pi}{4}R(\chi)R(\psi)\sum_{k=1}^{2}\mathrm{PV}\int_0^1 \mathrm{d}y\left(\frac{1}{y-\rho_1(\psi)+i\eta}-\frac{1}{y-\rho_2(\psi)-i\eta}\right)\log\left(\frac{\rho_k(\chi)}{y}\right)\\ &= -\frac{\pi}{4}R(\chi)R(\psi)\Big(-4\mathrm{Li}_2(-\psi)+\log^2\psi-4\log\psi\big(\log(\psi+1)-\log(\chi+1)\big)\\ &\qquad -2\log\chi\log\psi-2\zeta_2\Big).\end{aligned} \tag{4.101}$$

Upon the anti-symmetrisation in χ and ψ the terms on the last line of eq. (4.101) cancel.

We thus arrive at the following result for the imaginary part of the $(1,2,1)$ web,

$$\begin{aligned}\mathrm{Im}\,\mathscr{F}^{(2)}_{(1,2,1)} = -\pi R(\chi)R(\psi)\Big(&\mathrm{Li}_2(-\chi) - \mathrm{Li}_2(-\psi) - \tfrac{1}{4}\big(\log^2\chi - \log^2\psi\big)\\ &+ \big(\log\chi + \log\psi\big)\big(\log(\chi+1) - \log(\psi+1)\big)\Big)\,. \end{aligned} \tag{4.102}$$

Evaluation of imaginary part on the left-hand side of the cutting equation

The verification of our result in eq. (4.102) proceeds through an alternative computation of the imaginary part of the web, by evaluating the diagram for spacelike kinematics, $v_1 \cdot v_2 < 0$ and $v_2 \cdot v_3 < 0$, and subsequently performing the analytic continuation to timelike kinematics.

The web with spacelike kinematics is given to the leading order in ϵ by eq. (4.95), with the propagator roots ρ_k given by the upper case of eq. (4.47). Inserting the expressions for $P_{12}^{[0]}$ given in eq. (4.46) and performing the integrals in analogy with the calculations in eqs. (4.67) and (4.68) for the case of the non-planar two-loop ladder, leads to the following result for the web in spacelike kinematics,

$$\widetilde{\mathscr{F}}^{(2)}_{(1,2,1)} = R(\chi)R(\psi)\left(L(\psi)\log\chi - L(\chi)\log\psi\right), \tag{4.103}$$

where we introduced the auxiliary function $L(\chi) = -\mathrm{Li}_2(1-\chi) - \frac{1}{4}\log^2\chi$. This expression is consistent with previous results in the literature, see for example eq. (3.11) in ref. [97]. Upon analytic continuation in both χ and ψ we find the following result for the web with timelike kinematics,

$$\begin{aligned}\mathscr{F}^{(2)}_{(1,2,1)} = R(\chi)R(\psi)\Big[&-i\pi\Big(\mathrm{Li}_2(-\chi) - \tfrac{1}{4}\log^2\chi + \big(\log\chi + \log\psi\big)\log(\chi+1)\Big)\\ &+ \log\chi\,\mathrm{Li}_2(-\psi) - \big(\log\chi\log\psi - 6\zeta_2\big)\log(\chi+1)\\ &+ \tfrac{1}{4}\big(\log\chi\log\psi - 10\zeta_2\big)\log\chi\Big] - (\chi \leftrightarrow \psi)\,. \end{aligned} \tag{4.104}$$

The imaginary part of this expression agrees with the result in eq. (4.102), which was obtained from the cutting equation. This demonstrates explicitly that the position-space cutting prescription is also capable of reproducing the imaginary part of a web.

The web offers further checks, based on its dependence on two cusp angles. In addition to the preceding discussion, we may also consider the diagram in the case of mixed time- and spacelike kinematics, for example $\cosh\gamma_{12} \equiv v_1 \cdot v_2 > 0$ and $\cosh\gamma_{23} \equiv -v_2 \cdot v_3 > 0$. As we shall see shortly, the formalism of section 4.3 readily applies in this case as well. Effectively, the difference is that the imaginary part now receives no contribution from the γ_{23}-channel, since gluon propagators stretched between mutually spacelike eikonal lines have vanishing cuts. Indeed, going back to the formula for the imaginary part in the explicit form eq. (4.97), we observe that in the above case of mixed time- and spacelike kinematics, the roots of the propagator $P_{23}^{[0]}(y)$ lie outside the range of integration. As a result, the

second term in eq. (4.97) vanishes and in the first term the principal-value prescription may be dropped, which results in

$$\operatorname{Im}\mathscr{F}^{(2)}_{(1,2,1)} = \int_0^1 \mathrm{d}x\,\mathrm{d}y\;\Delta_{12}(x)\,P^{[0]}_{23}(y)\log\left(\frac{x}{y}\right). \tag{4.105}$$

After inserting $\Delta_{12}(x)$ and $P^{[0]}_{23}(y)$ from eq. (4.100) and integrating out the delta functions, the imaginary part can be expressed in terms of multiple polylogarithms, which in turn readily simplify into classical polylogarithms, yielding

$$\begin{aligned}\operatorname{Im}\mathscr{F}^{(2)}_{(1,2,1)} &= \frac{\pi}{4}R(\chi)R(\psi)\Big(-2G(\rho_2(\psi),0;1)+2G(\rho_1(\psi),0;1)\\ &\qquad + G(0;\rho_2(\chi))G(\rho_2(\psi);1)+G(0;\rho_1(\chi))G(\rho_2(\psi);1)\\ &\qquad - G(0;\rho_2(\chi))G(\rho_1(\psi);1)-G(0;\rho_1(\chi))G(\rho_1(\psi);1)\Big)\\ &= \pi R(\chi)R(\psi)\Big(\mathrm{Li}_2(\psi)-\log\psi\left(\tfrac{1}{4}\log\psi-\log(1-\psi)+\log(\chi+1)-\tfrac{1}{2}\log\chi\right)-\zeta_2\Big).\end{aligned} \tag{4.106}$$

It is straightforward to verify that this result agrees with the imaginary part acquired from eq. (4.103) upon the analytic continuation $\chi \to -1/\chi - i\eta$. We thereby verified in this example that that the position-space cutting formula (see eq. (4.42)) reproduces the correct imaginary part of the web also for mixed time- and spacelike kinematics.

4.5. Position-space cuts of eikonal diagrams with internal vertices

In this section we turn to the application of the position-space cutting prescription to diagrams with internal (three- and four-gluon) vertices. Such vertices are not constrained to lie on one of the eikonal trajectories, but can reside a priori anywhere in spacetime. In particular we provide details on the calculation of the imaginary part of the diagram involving a three-gluon vertex connected to three Wilson lines (see fig. 4.14).

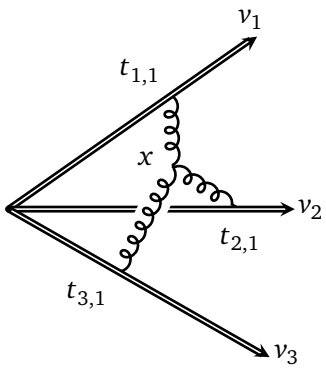

Figure 4.14: The non-planar two-loop three-gluon vertex diagram.

The integrated result for the diagram in fig. 4.14 was first obtained in refs. [93, 94] using a Mellin-Barnes representation of the two loop-momentum integrals. In terms of the cusp angles γ_{ij}, defined through $\cosh\gamma_{ij} = -v_i \cdot v_j$, it is given by

$$\widetilde{F}_{3g} = -if^{abc}\mathbf{T}_1^a\mathbf{T}_2^b\mathbf{T}_3^c \frac{2}{\epsilon}\left(\frac{\alpha_s}{4\pi}\right)^2 \sum_{i,j,k=1}^{3} \varepsilon_{ijk}\, \gamma_{ij}^2 \gamma_{ki} \coth\gamma_{ki} \,. \tag{4.107}$$

This expression is valid for an unphysical configuration with spacelike kinematics for all pairs of Wilson lines, i.e. $v_i \cdot v_j < 0$, as indicated by the tilde on $\widetilde{F}_{3g}$. In agreement with our observations in section 4.2, $\widetilde{F}_{3g}$ has no imaginary part. In a physical configuration of massive Wilson lines, each velocity is constrained to the unit three-hyperboloid, either inside the future light cone or inside the past light cone. There are two inequivalent physical configurations, with either two or three velocities inside the same light cone (see fig. 4.15). In both configurations at least one pair of Wilson lines is timelike separated, i.e. $v_i \cdot v_j > 0$, leading to a non-vanishing imaginary part.

In this section we consider the configuration in fig. 4.15(b), where all Wilson lines correspond to outgoing states, such that $v_i \cdot v_j > 0$ for each pair of Wilson lines. The analytic result for such timelike kinematics, denoted by F_{3g}, is obtained from the spacelike expression $\widetilde{F}_{3g}$ in eq. (4.107) by analytic continuation $\gamma_{ij} \to i\pi - \gamma_{ij}$ for all $i \neq j$. The imaginary

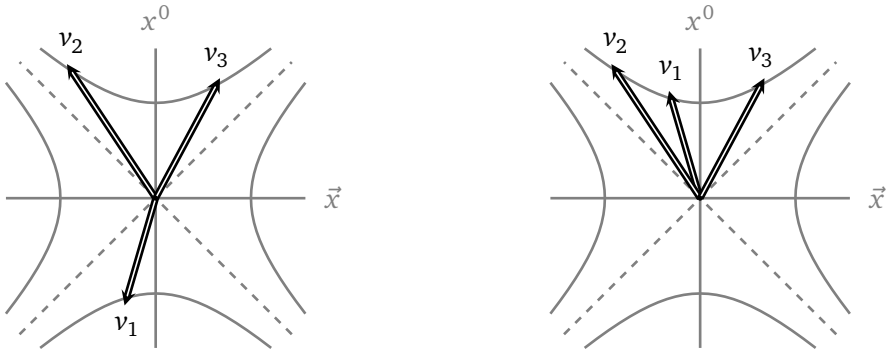

Figure 4.15: Physical configurations for three distinct Wilson-line velocities: (a) one incoming and two outgoing lines, or (b) three outgoing lines. Configurations related by time-reversal are omitted. In this section we compute the imaginary part of the three-gluon vertex diagram in the physical configuration (b).

part of the resulting expression is

$$\operatorname{Im} F_{3g} = -f^{abc}\mathbf{T}_1^a\mathbf{T}_2^b\mathbf{T}_3^c \left(\frac{\alpha_s}{4\pi}\right)^2 \frac{2}{\epsilon} \sum_{i,j,k=1}^{3} \varepsilon_{ijk} \left(\gamma_{ij}^2\gamma_{ki} - 2\pi^2\gamma_{ij}\right) \coth\gamma_{ki} \,. \tag{4.108}$$

In the following, our task is to compute this imaginary part with our formalism. Like in section 4.3, we first need to extract the leading divergence of F_{3g} in its position-space representation. The divergence of the three-gluon vertex diagram, has a only a simple pole in ϵ, is extracted from the radial integral over the three-gluon vertex position. Having extracted the leading divergence, the diagram can be written as $\frac{1}{\epsilon} \times$ (finite) and the position-space cuts can be applied to the finite function. The one-dimensional integrals along the Wilson lines are then trivially performed using the delta functions from the cuts. The remaining integrations over the coordinates of the three-gluon vertex are performed numerically, after which the final result is compared to the analytic expression in eq. (4.108).

We start by writing down the position-space representation of F_{3g}. It reads[6]

$$F_{3g} = -f^{abc}\mathbf{T}_1^a\mathbf{T}_2^b\mathbf{T}_3^c \left(\frac{\alpha_s}{4\pi}\right)^2 \frac{4}{\pi^2}\mu^{4\epsilon} \int \frac{\mathrm{d}^d x}{r^{4-6\epsilon}} \Bigg(\sum_{i,j,k=1}^{3} \varepsilon_{ijk}\, v_i\cdot v_j\, \zeta_i\, \zeta_k \times \frac{\partial\, g(\zeta_i,\epsilon)}{\partial\,\zeta_i} g(\zeta_j,\epsilon)\, g(\zeta_k,\epsilon) \Bigg) \,. \tag{4.109}$$

Here the three-gluon vertex position x is integrated over all of Minkowski space. In the integrand x is decomposed into a radial distance r and direction u, via $x^\mu = r\,u^\mu$, such that $u^2 = 1$ for timelike x and $u^2 = -1$ for spacelike x. Dot products between u and the Wilson line velocities are denoted by $\zeta_i = v_i \cdot u$. The one-dimensional integrals along the Wilson

[6] See ref. [122] for the corresponding representation of this diagram in Euclidean space.

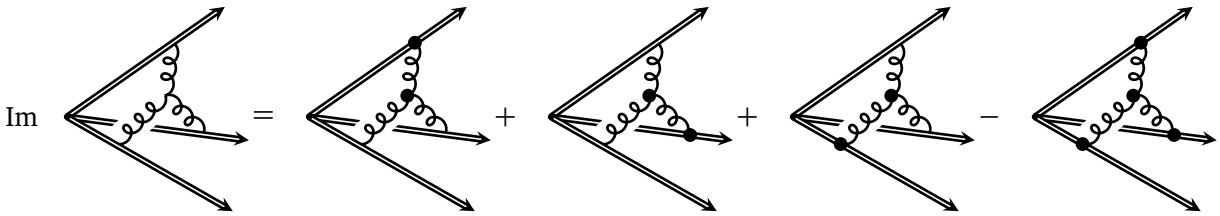

Figure 4.16: Graphical representation of position-space cuts applied to a diagram with an internal vertex.

lines are contained in the functions $g(\zeta_i, \epsilon)$, which are defined as

$$g(\zeta_i, \epsilon) = \int_0^\infty \frac{\mathrm{d}x_i}{[-(u^2 - 2\,x_i\,\zeta_i + x_i^2) + i\eta]^{1-\epsilon}} \,. \tag{4.110}$$

After a change of variables in eq. (4.109) to hyperspherical coordinates, the radial integral contains the overall divergence and may easily be performed. Restricting attention to the leading order in ϵ allows us to set $\epsilon = 0$ in the finite function $\mathscr{F}_{3g}$, yielding

$$\begin{aligned} F_{3g} &= -f^{abc}\mathbf{T}_1^a\mathbf{T}_2^b\mathbf{T}_3^c \left(\frac{\alpha_s}{4\pi}\right)^2 \frac{1}{\pi^2\,\epsilon}\,\mathscr{F}_{3g} \,, \\ \mathscr{F}_{3g} &= \int_{\widetilde{\mathbb{RP}}^{1,2}} \mathrm{d}^3u \sum_{i,j,k=1}^{3} \varepsilon_{ijk}\, v_i\cdot v_j\; \zeta_i\,\zeta_k\, \frac{\partial\, g(\zeta_i, 0)}{\partial\,\zeta_i}\, g(\zeta_j, 0)\, g(\zeta_k, 0) \,. \end{aligned} \tag{4.111}$$

The integration domain for the three-gluon vertex u is $\widetilde{\mathbb{RP}}^{1,2} \equiv \mathrm{H}_+^3 \cup \mathrm{H}_-^3 \cup \mathrm{dS}_3^+ \cup \mathrm{dS}_3^-$, the union of the upper and lower sheets of the unit three-hyperboloid and three-dimensional de Sitter space, defined by

$$\begin{aligned} \mathrm{H}_\pm^3 &= \{u \in \mathbb{R}^{1,3} : u^2 = 1 \quad \text{and } u_0 \gtrless 0\} \,, \\ \mathrm{dS}_3^\pm &= \{u \in \mathbb{R}^{1,3} : u^2 = -1 \text{ and } u_0 \gtrless 0\} \,. \end{aligned} \tag{4.112}$$

Having written the three-gluon vertex diagram in the form of eq. (4.111), we are ready to apply our formalism to obtain the imaginary part of $\mathscr{F}_{3g}$ from its cuts. This in turn gives the imaginary part of the full diagram F_{3g}, as they are proportional up to a real constant.

The imaginary part of $\mathscr{F}_{3g}$ is computed from the formula in eq. (4.42), as illustrated schematically in fig. 4.16. The cut propagators stretching between the three-gluon vertex and the Wilson lines take the obvious form $\Delta_i(x_i) = -\pi\,\delta(u^2 - 2\,x_i\,\zeta_i + x_i^2)$, rather than eq. (4.40) for propagators connecting two Wilson lines. In order to resolve the support of these delta functions in the different subregions of $\widetilde{\mathbb{RP}}^{1,2}$ it is convenient to introduce variables y_i that are equal to ζ_i, possibly up to a sign depending on the location of u. Explicitly, we let $y_i = \zeta_i$ for $u \in \mathrm{H}_+^3 \cup \mathrm{dS}_3^+$ and $y_i = -\zeta_i$ for $u \in \mathrm{H}_-^3 \cup \mathrm{dS}_3^-$. In terms of these variables a

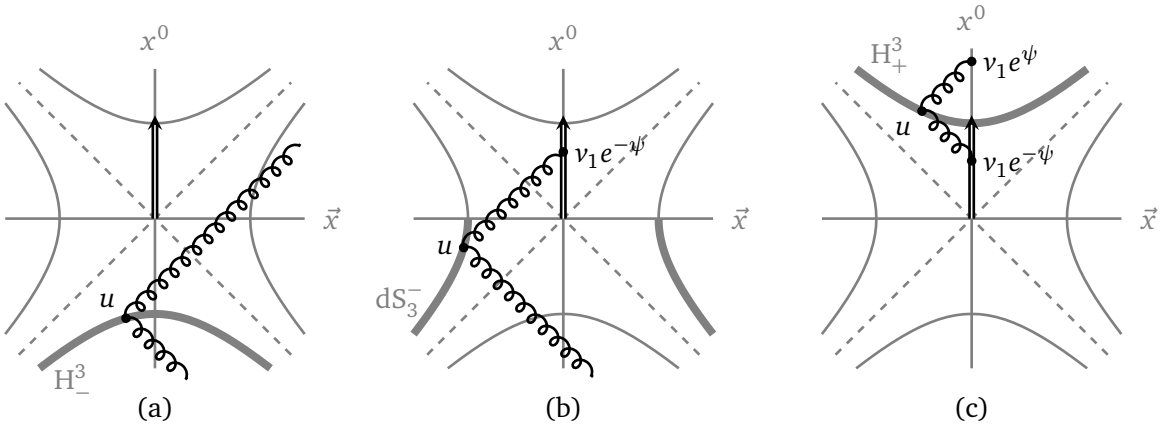

Figure 4.17: Spacetime pictures of a Wilson line along the positive x^0-axis (with normalized velocity v_1) and a three-gluon vertex u, located in the region (a) H^3_-, (b) dS^-_3 or (c) H^3_+. The region dS^+_3 is similar to dS^-_3 and thus omitted. Each figure shows two lightlike gluons emanating from u: one along the future light cone and the other along the past light cone. Among the two on-shell gluons either zero, one or two gluons are able to connect to the Wilson line. In other words, in case (a), (b) and (c) there are respectively zero, one and two solutions to the delta functions coming from the cut operators. This means that in the region (a) H^3_- the operator Cut_{x_1} vanishes, thereby producing no imaginary part. Furthermore, as discussed in the main text, the imaginary parts from the spacelike regions (b) dS^-_3 and dS^+_3 cancel each other, so the imaginary part of the diagram arises from the region (c) H^3_+.

cut operator acting on a function $g(\zeta_i, 0)$ yields

$$\mathrm{Cut}_{x_i}\, g(\zeta_i,0) = -\pi \int_0^\infty \mathrm{d}x_i\; \delta(u^2 - 2\,x_i\,\zeta_i + x_i^2) = \begin{cases} -\frac{\pi}{2}\,(1\pm 1)\,\big(y_i^2-1\big)^{-1/2} & \text{in } \mathrm{H}^3_\pm\,, \\ -\frac{\pi}{2}\,\big(y_i^2+1\big)^{-1/2} & \text{in } \mathrm{dS}^\pm_3\,, \end{cases} \tag{4.113}$$

while the principal-value part, due to $\mathrm{Cut}_{x_j}\, g(\zeta_i, 0)$ with $i \neq j$, evaluates to

$$\mathrm{PV} \int_0^\infty \frac{\mathrm{d}x_i}{-(u^2 - 2\,x_i\,\zeta_i + x_i^2) + i\eta} \;=\; \begin{cases} \pm\,\mathrm{arcosh}(y_i)\,\big(y_i^2-1\big)^{-1/2} & \text{in } \mathrm{H}^3_\pm\,, \\ \mp\,\mathrm{arsinh}(y_i)\,\big(y_i^2+1\big)^{-1/2} & \text{in } \mathrm{dS}^\pm_3\,. \end{cases} \tag{4.114}$$

The right-hand side of eq. (4.113) shows that the cut vanishes for u in the region H^3_-. This is a consequence of the delta function having no support inside the domain of integration $[0, \infty)$. In the regions $\mathrm{dS}^\pm_3$ and H^3_+ there are respectively one and two solutions to the delta-function constraint, as can also be understood by inspection of fig. 4.17.

Focusing on the contributions to the imaginary part from dS^+_3 and dS^-_3, we see that both the single and the triple cuts acting on the product $g(\zeta_i, 0)\, g(\zeta_j, 0)\, g(\zeta_k, 0)$ in $\mathscr{F}_{3g}$ yield the same results in both regions. But apart from this product of g's, the sum in eq. (4.111) also contains $\zeta_i\,\zeta_k\,\frac{\partial}{\partial \zeta_i}$, which differs by a sign between the two regions. As a result, the imaginary part arising from the regions dS^+_3 and dS^-_3 cancel each other. The upshot is thus that the imaginary part of $\mathscr{F}_{3g}$ arises solely from the region H^3_+.

The final step in the computation of $\mathrm{Im}\,\mathscr{F}_{3g}$ is now to perform the integration over the direction of the three-gluon vertex $u \in \mathrm{H}^3_+$. We do not have analytic results for the integrals involved, but a numerical evaluation is sufficient to show agreement with the analytic formula in eq. (4.108). Let us give a few details regarding the setup of the numerical integration. The three-gluon vertex location u may be parametrized explicitly in terms of Minkowski angles ψ, ϑ and ϕ.

$$\mathrm{H}^3_+ : \quad \begin{cases} u^0 &= \cosh\psi\,, \\ u^1 &= \sinh\psi\sin\vartheta\cos\phi\,, \\ u^2 &= \sinh\psi\sin\vartheta\sin\phi\,, \\ u^3 &= \sinh\psi\cos\vartheta\,, \end{cases} \qquad \begin{array}{rcccl} 0 &\leq& \psi &<& \infty\,, \\ 0 &\leq& \vartheta &\leq& \pi\,, \\ 0 &\leq& \phi &\leq& 2\pi\,. \end{array} \tag{4.115}$$

To facilitate the numerical integration over $\psi \in [0,\infty)$ we perform a further change of variables $z = \tanh\psi$, which has the effect of producing a finite integration domain $z \in [0,1]$. Explicit expressions for $\zeta_i = y_i = u \cdot v_i$ in terms of z, the angles ϑ, ϕ and the cusp angles γ_{ij} are obtained by choosing a convenient Lorentz frame. For example,

$$\begin{aligned} v_1^\mu &= (1,\,0,\,0,\,0)\,, \\ v_2^\mu &= (\cosh\gamma_{12},\,0,\,0,\,\sinh\gamma_{12})\,, \\ v_3^\mu &= (\cosh\gamma_{13},\,0,\,\sin\theta_3\sinh\gamma_{13},\,\cos\theta_3\sinh\gamma_{13})\,. \end{aligned} \tag{4.116}$$

These velocities manifestly satisfy $v_i^2 = 1$ and $v_1 \cdot v_k = \cosh\gamma_{1j}$ for $j = 2,3$. The remaining identity, $v_2 \cdot v_3 = \cosh\gamma_{23}$, fixes θ_3 in terms of the cusp angles,

$$\cos\theta_3 = \frac{\cosh\gamma_{12}\cosh\gamma_{13} - \cosh\gamma_{23}}{\sinh\gamma_{12}\sinh\gamma_{13}}\,. \tag{4.117}$$

The explicit parametrisation of the Wilson-line velocities in eq. (4.116) breaks the antisymmetry of $\mathscr{F}_{3g}$ under interchange of any pair of cusp angles at the integrand level. However, the antisymmetry must be recovered after integration. At the level of numerical integration this indeed happens for small cusp angles, while for large cusp angles numerical instabilities arise from the integration near $z \approx 1$, i.e. very large ψ. Averaging over the cusp angles γ_{ij} remedies those instabilities.

Having constructed expressions for ζ_i in terms of z, the angles ϑ, ϕ and the cusp angles γ_{ij}, the imaginary part of the three-gluon vertex diagram is explicitly given by

$$\mathrm{Im}\,\mathscr{F}_{3g} = \int_0^1 \frac{\mathrm{d}z\,z^2}{(1-z^2)^2} \int_0^\pi \mathrm{d}\vartheta\sin\vartheta \int_0^{2\pi} \mathrm{d}\phi \sum_{i,j,k=1}^{3} \varepsilon_{ijk}\, v_i \cdot v_j\, \zeta_i\, \zeta_k \left(\frac{\partial}{\partial\zeta_i}\,\mathscr{G}\big(\{\zeta_i\}\big)\right), \tag{4.118}$$

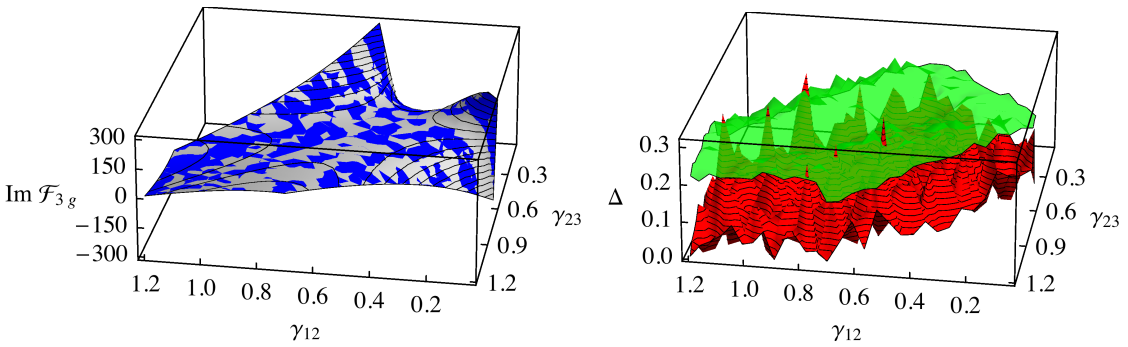

Figure 4.18: A comparison between the numerical and analytical results for the imaginary part of the three-gluon vertex diagram. The left pane shows $\mathrm{Im}\,\mathcal{F}_{3g}$ as a function of two cusp angles from numerical integration (in blue) and from the analytical result (in light gray) superimposed. The numerical result fits the analytic function rather well, with an overall scalefactor deviating from one by about $2 \cdot 10^{-5}$. In the right pane we observe that Δ, the absolute difference between the numerical and the analytical values, (in red) is below the numerical errors (in translucent green) for nearly all points $(\gamma_{12}, \gamma_{23})$ and is on average about three times smaller. The relative difference with respect to the analytic formula, $\Delta/|\mathrm{Im}\,\mathcal{F}_{3g}|$, is on average of the order of 2 percent, leading to the conclusion that there is an excellent agreement between the numerical and analytical results. In both plots $\gamma_{13} = 0.5$, while γ_{12} and γ_{23} vary between 0.0 and 1.2.

where the cut operators are absorbed into the function $\mathcal{G}(\{\zeta_i\})$, given by

$$\begin{aligned}\mathcal{G}(\{\zeta_i\}) &= \left(\mathrm{Cut}_{x_i} + \mathrm{Cut}_{x_j} + \mathrm{Cut}_{x_k} - \mathrm{Cut}_{x_i,x_j,x_k}\right) g(\zeta_i,0) g(\zeta_j,0)\, g(\zeta_k,0) \\ &= -\frac{\pi\,\mathrm{arcosh}\,\zeta_j\,\mathrm{arcosh}\,\zeta_k + \pi\,\mathrm{arcosh}\,\zeta_i\,\mathrm{arcosh}\,\zeta_k + \pi\,\mathrm{arcosh}\,\zeta_i\,\mathrm{arcosh}\,\zeta_j - \pi^3}{(\zeta_i^2-1)^{1/2}(\zeta_j^2-1)^{1/2}(\zeta_k^2-1)^{1/2}}\,.\end{aligned} \tag{4.119}$$

For the numerical integration of eq. (4.118) we have used the C++ library GSL [123]. A comparison between the numerical and analytical results for $\mathrm{Im}\,\mathcal{F}_{3g}$ is shown in fig. 4.18. We find that the relative difference between the numerical and analytical results are at the percent level, with absolute differences smaller than numerical errors. We conclude that our formula for the imaginary part in eq. (4.118) is in excellent agreement with the analytic expression in eq. (4.108). This suggests the applicability of the position-space cutting formalism in section 4.3 for obtaining the imaginary part of any eikonal diagram with internal vertices.

4.6. Conclusions

In this chapter I have described a new notion of diagrammatic cuts, namely position-space cuts of eikonal diagrams in the perturbative expansion of Wilson line correlators. The introduced cutting prescription allows to compute directly the imaginary part of eikonal diagrams by putting an odd number of soft gluons on shell, according to eq. (4.42). Working

in position space offers an elegant physical interpretation of the imaginary part based on causality: only hard particles that are in causal contact can exchange lightlike gluons, thereby affecting the phase of each other's states, giving rise to an imaginary part of the correlator. The imaginary part can be related to an interquark potential in the non-relativistic limit of Abelian or conformal field theories. I demonstrated the practical applicability of the position-space cutting prescription to several two- and three-loop eikonal diagrams, finding agreement with results previously obtained in the literature.

An alternative prescription for computing the imaginary part of eikonal diagrams, via momentum-space cuts, has already been available. In that prescription, unitarity dictates that the imaginary part of an eikonal diagram is given by a sum of phase-space cuts, factoring the diagram into on-shell lower-loop diagrams. But the evaluation of those phase-space cuts can pose a serious challenge. In such cases the position-space cuts provides a computational advantage with respect to momentum-space cuts, as was shown in the case of the three-loop non-planar ladder diagram.

An apparent limitation of the position-space cutting prescription is that it allows to compute the imaginary part of eikonal diagrams only to the leading order in ϵ. But in practice the leading order of a Wilson line correlator typically contains the physically relevant information. This owes to the non-Abelian exponentiation theorem which states that the correlator can be expressed as an exponential of webs (combinations of diagrams in which the leading divergence cancels). The position-space cuts apply directly to the entire webs and can be used to extract their imaginary part, as demonstrated for a two-loop web with three Wilson lines. In this sense the cutting prescription has a nontrivial interplay with non-Abelian exponentiation.

Further developments may include the extension of the present formalism to computations of imaginary parts of Wilson line correlators to sub-leading orders in ϵ and the study of analytic approaches to diagrams with internal vertices. It would also be intriguing to investigate whether the position-space cuts can play a role in developing (generalized) unitarity methods for correlators of Wilson lines. This idea, to reconstruct amplitudes from their discontinuities, is pursued in the next chapter in the context of Drell-Yan production.

Chapter 5

Unitarity method for the Drell-Yan process

Unitarity is not only developed through the construction of new cutting rules, as shown in the previous chapter, but also through the application of existing cutting rules to new processes. Particularly relevant for the Large Hadron Collider (LHC) is the Drell-Yan process, in which a lepton-antilepton pair is produced in the decay of a virtual photon or Z boson. Extracting the Drell-Yan cross section through the use of unitarity is the topic of the present chapter.

Inspiration for this idea is drawn from the application of unitarity to deep inelastic scattering (DIS). For this fully-inclusive process the optical theorem is valid, so its total cross section can be obtained from the imaginary part of the corresponding forward scattering process (see section 2.1). Integrating the imaginary part along the physical branch cuts corresponds to Mellin moments of the structure function, which can be most conveniently extracted as series coefficients of the forward amplitude. This approach has been very successful for the computation of two- and three-loop DIS splitting functions [124–126].

A step up in complexity is required to describe the one-particle inclusive Drell-Yan process, which is prototypical for other processes such as Higgs production in the large top mass limit. However, in taking this step we introduce a problem: the optical theorem is invalid for non-inclusive processes and therefore unitarity cannot be applied – at least straightforwardly – to the Drell-Yan process.

The origin of this problem is analysed in the following two sections and, subsequently, it is shown to affect cutting equations for Drell-Yan amplitudes through the appearance of unphysical cut diagrams. Section 5.3 proceeds to provide a prescription for removing such unphysical cut contributions, which is then finally applied in section 5.4 to two-loop diagrams that are representative next-to-next-to-leading order (NNLO) QCD corrections to the Drell-Yan cross section.

5.1. The optical theorem for deep inelastic scattering

Let us first briefly review the application of the optical theorem to deep inelastic scattering. Following the exposition in the textbook [101], the fully inclusive differential cross section for this process, in which a lepton with momentum ℓ scatters off a quark with momentum p through an off-shell photon exchange, can be written in the form

$$d\sigma = \frac{1}{2s}\frac{1}{Q^4} L^{\mu\nu}(\ell,\ell') W_{\mu\nu}(p,q) \frac{d^3\ell'}{|\ell'|}, \tag{5.1}$$

where ℓ' is the momentum of the recoiling lepton and $q = \ell - \ell'$ is the momentum of the exchanged photon. The decomposition of the cross section into a hadronic tensor $W_{\mu\nu}$ and a leptonic tensor $L_{\mu\nu}$ is depicted in fig. 5.1. These two tensors are defined as

$$\begin{aligned} L_{\mu\nu}(\ell,\ell') &= \frac{e^2}{8\pi^2}\left(\ell_\mu \ell'_\nu + \ell_\nu \ell'_\mu - \eta_{\mu\nu}\ell\cdot\ell'\right), \\ W_{\mu\nu}(p,q) &= \frac{1}{8\pi}\sum_n \langle P(p)|J^\dagger_\mu(0)|n\rangle\langle n|J_\nu(0)|P(p)\rangle (2\pi)^4\delta^4(p_n - p - q), \end{aligned} \tag{5.2}$$

where implicit spin quantum numbers in the external states are summed over.

The hadronic tensor effectively describes the process $\gamma^*(q) + p \to X$, where X denotes all hadronic final states consistent with quantum number conservation, including a recoiling quark with momentum p'. This process receives higher-order QCD corrections, which can be computed in a clever way through unitarity. This works as follows. Current conservation

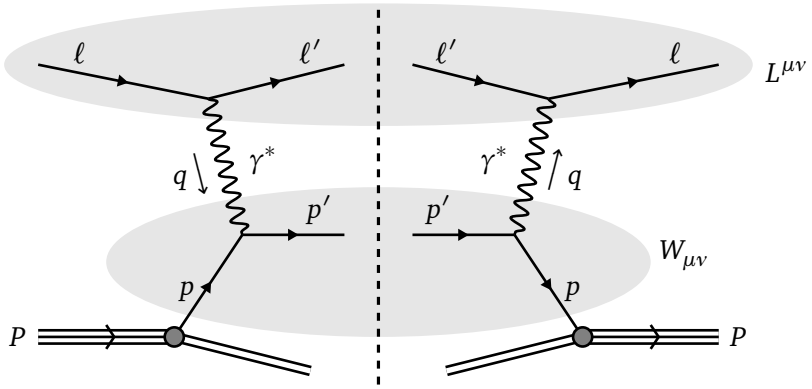

Figure 5.1: The first-order contribution to the DIS cross section in cut diagram notation: the tree-amplitude for the DIS process (left of the dashed line) is multiplied by its complex conjugate (on the right) and integrated over the phase space of the particles crossing the dashed line. The decomposition into $L^{\mu\nu}$ and $W_{\mu\nu}$ is indicated by the shaded regions. The hadronic tensor $W_{\mu\nu}$ receives QCD corrections and is computed through the optical theorem.

($q^\mu W_{\mu\nu} = q^\nu W_{\mu\nu} = 0$) and parity invariance in both indices imply the structure

$$W_{\mu\nu}(p,q) = -\left(\eta_{\mu\nu} - \frac{q_\mu q_\nu}{q^2}\right) W_1(x,Q^2) + \left(p_\mu - \frac{q_\mu p\cdot q}{q^2}\right)\left(p_\nu - \frac{q_\nu p\cdot q}{q^2}\right) W_2(x,Q^2), \tag{5.3}$$

so that in this process the structure of the proton is encoded in just two scalar functions, W_1 and W_2, which depend on the variables

$$Q^2 = -q^2, \qquad x = \frac{Q^2}{2p\cdot q}. \tag{5.4}$$

The optical theorem applies to the hadronic tensor $W_{\mu\nu}$ because the sum in eq. (5.2) is fully inclusive, so that we can write

$$W_{\mu\nu}(p,q) = 2\,\mathrm{Im}\,T_{\mu\nu}(p,q), \tag{5.5}$$

where $T_{\mu\nu}$ is the forward Compton scattering amplitude, $\gamma^*(q)+p \to \gamma^*(q)+p$. This process has kinematic thresholds, where intermediate states can go on-shell, at $(p\pm q)^2 > 0$. To uncover the resulting analytic structure of $T_{\mu\nu}(p,q)$, it is convenient to first decompose it in exactly the same way as $W_{\mu\nu}$ in eq. (5.3), but now in terms of the scalar functions

$$T_i\left(\omega = \frac{1}{x}, Q^2\right), \quad i = 1,2, \tag{5.6}$$

where we have chosen to indicate the functional dependence in terms of the *reciprocal* variable $\omega = 1/x$. At fixed Q^2, these functions are analytic for all ω except for branch cuts along the ω-intervals $(-\infty,-1]$ and $[1,\infty)$. Moreover, the T_i are symmetric in ω,

$$T_i(-\omega,Q^2) = T_i(\omega,Q^2). \tag{5.7}$$

One can now compute Mellin moments of the $W_i(x,Q^2)$ functions by expanding the $T_i(\omega,Q^2)$ amplitudes. More explicitly, the nth derivative of T_i at $\omega = 0$ may be rewritten by Cauchy's theorem in terms of the contour in fig. 5.2a,

$$T_i^{(n)}(Q^2) \equiv \frac{1}{n!}\frac{\mathrm{d}^n T_i(\omega,Q^2)}{\mathrm{d}\omega^n}\bigg|_{\omega=0} = \oint_{C_0}\frac{\mathrm{d}\omega}{2\pi i}\,\omega^{-n-1}T_i(\omega,Q^2). \tag{5.8}$$

The contour C_0 may be deformed into the contour C_1 shown in fig. 5.2b. Using the symmetry property in eq. (5.7) we then have

$$T_i^{(n)}(Q^2) = \frac{(1+(-1)^n)}{2\pi i}\int_1^\infty \mathrm{d}\omega\,\omega^{-n-1}\,\underset{\omega}{\mathrm{Disc}}\,T_i(\omega,Q^2)\,. \tag{5.9}$$

The presence of the factor $(1+(-1)^n)$ in eq. (5.9) implies that odd series coefficients vanish. For n even, instead, using the optical theorem in the form of eq. (5.5), and changing

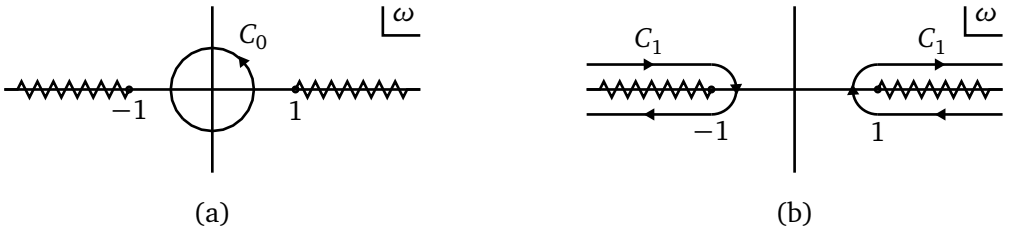

(a) (b)

Figure 5.2: The branch cut structure of $T_i(\omega, Q^2)$ and the contours used in the computation of $T_i^{(n)}(Q^2)$. The contour C_0 that wraps around the origin (a) is deformed into the contour C_1 that encloses the two branch cuts (b). Note that the integrand in eq. (5.8) contains an additional pole at the origin, which makes the contour integrals non-vanishing.

integration variables to $x = 1/\omega$, we find

$$T_i^{(n)}(Q^2) = \frac{1}{\pi}\int_0^1 \mathrm{d}x\, x^{n-1} W_i(x, Q^2) = \frac{1}{\pi}\mathscr{M}_n\left[W_i(Q^2)\right] \,, \tag{5.10}$$

where the second equality uses the definition of the Mellin transform, see eq. (B.8). Thus, the expansion of the forward scattering amplitude in ω, which is relatively easy to calculate, yields directly the Mellin moments of the total cross section. This is the optical theorem in Mellin space.

This way of using the optical theorem, computing directly the Mellin moments of the DIS structure functions by expansion in $1/x$, has been marvellously successful for two- and three-loop calculations for deep inelastic scattering [125–127] and serves as inspiration to the work described in this chapter.

5.2. From deep inelastic scattering to the Drell-Yan process

Deep inelastic scattering has been experimentally studied extensively in the past, for example at the Hadron Electron RingAnlage (HERA) in Hamburg, which has operated between 1992 and 2007. By colliding electrons or positrons against protons, this experiment yielded valuable insights regarding the structure of the proton, providing evidence for the existence of sea-quarks, the unification of electromagnetic and weak forces and the peculiar scale dependence of the strong force (asymptotic freedom), to name a few examples [128]. Since 2008 the field of particle physics has entered a new era with the startup of the LHC in Geneva. For understanding collisions in this experiment, we need to study processes of the type $pp \to W + \text{jets}$, $pp \to H + \text{jets}$, and so on. In view of the successful application of the optical theorem to deep inelastic scattering, as reviewed in the previous section, one might wonder if similar techniques may also be applied to such LHC processes.

A prototypical example of an LHC process is the Drell-Yan process, where two partons collide to produce a massive particle (off-shell photon, vector boson or Higgs particle, say) plus extra radiation allowed by quantum number conservation. The massive particle has

a mass Q^2, analogous to the off-shell-ness $q^2 = -Q^2$ in deep inelastic scattering. It is unstable and subsequently decays, for example into two leptons. A typical Drell-Yan process is depicted in fig. 5.3.

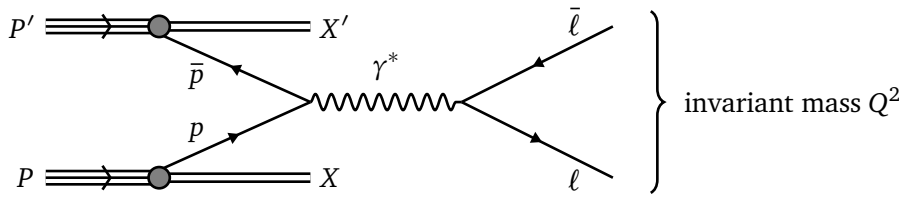

Figure 5.3: Schematic representation of a typical Drell-Yan process: two quarks produce a lepton pair mediated by an off-shell photon.

The Drell-Yan process is different from deep inelastic scattering, although they are closely related. The similarities and differences are best appreciated by focussing on the partonic interactions. As illustrated in fig. 5.4, the two corresponding processes are related by crossing symmetry. Crossing symmetry states that the amplitude for a process with a particle with momentum p in the initial state is equal to the amplitude for the identical process, but with instead an antiparticle with momentum $\bar{p} = -p$ in the final state, $\mathcal{A}(\psi(p)+\cdots\to\cdots) = \mathcal{A}(\cdots\to\overline{\psi}(\bar{p})+\cdots)$. Thus, the amplitudes for Drell-Yan are closely related to the amplitudes for deep inelastic scattering.

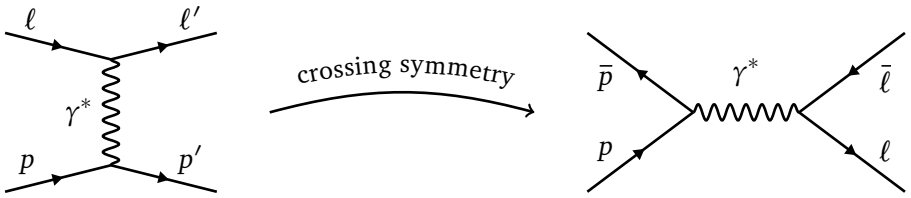

Figure 5.4: At partonic level, deep inelastic scattering (left) is related to the Drell-Yan process (right) by exchanging the incoming lepton with the outgoing quark (crossing symmetry).

Taking one step further, let us zoom in on the parts where QCD is at work. The concept of separating the partonic cross section into hadronic and leptonic tensors, as used for deep inelastic scattering (see fig. 5.1), also applies to the Drell-Yan process. Again, the hadronic tensor is the factor that receives higher-order QCD corrections. We focus on that piece, which essentially describes the process $\gamma^* + p \to p' + X$ in the case of deep inelastic scattering and $p + \bar{p} \to \gamma + X$ in the case of Drell-Yan. This is illustrated in fig. 5.5 in the case that X is comprised of a single gluon.

Between these two hadronic processes there is a small difference, but one which has a significant impact. In the case of deep inelastic scattering, the final state can consist of any set of particles, as long as quantum number conservation is not violated. That set of particles necessarily includes the explicit final state parton with momentum p', according to the Feynman rules. In other words, this process is fully inclusive. The Drell-Yan process, on the other hand, is not fully inclusive. In this case the final state is constrained to contain a particular type of massive particle, be it either an off-shell photon, vector boson or Higgs

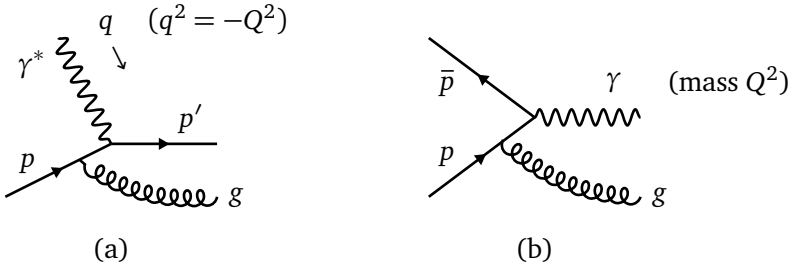

Figure 5.5: The hadronic interactions in (a) deep inelastic scattering and (b) the Drell-Yan process. The single gluon radiation shows an example of an allowed final state X.

boson. The Feynman rules allow all options, but the particular process under consideration calls for only one of these options. The impact of this non-inclusiveness of the Drell-Yan process is that the optical theorem is not applicable. For this reason we shall have to use cutting equations instead, as will be explained in the next section.

5.3. The Drell-Yan cross section from cutting equations

The non-inclusive Drell-Yan cross section cannot be obtained from the optical theorem. Fortunately the more general cutting equations hold for any amplitude, as explained in section 2.2, which therefore *can* be used in this context. Analogous to the treatment of deep inelastic scattering, this approach will allow to compute the Mellin moments of the Drell-Yan cross section. Accordingly, this section starts with a discussion of cutting equations in Mellin space. In section 5.3.2 the encountered cut diagrams are separated in two classes: cuts that contribute to the Drell-Yan cross section (physical) and cuts that belong to other processes (unphysical). The crucial task is then to eliminate the unphysical cuts from the cutting equations, so as to be left with the Drell-Yan cross section. How to achieve this in practice in the context of master integrals (which will be introduced in sections 5.3.3 and 5.3.4) is the main result of this chapter and will finally be described in section 5.3.5.

5.3.1. Cutting equation in Mellin space

Any Feynman diagram (or amplitude) $\mathscr{F}$ satisfies a unitarity cutting equation, as described in section 2.2. The generic form of such a cutting equation reads

$$\text{Disc}\,\mathscr{F} = \sum_k \text{Cut}_k\,\mathscr{F}\ . \tag{5.11}$$

An explicit example of this equation can be found in eq. (5.5), where the amplitude $\mathscr{F}$ is taken to be the forward Compton scattering amplitude and where the corresponding sum of cuts $\sum_k \text{Cut}_k\,\mathscr{F}$ produces the total DIS cross section. In this case there is no obstruction to take the Mellin transform on both sides of the cutting equation and the result can be found in eq. (5.10). Such an expression is referred to as the cutting equation in Mellin space.

Similarly, one can insert forward amplitudes $\mathscr{F}$ into eq. (5.11), whose cuts are supposed to reproduce the Drell-Yan cross section. However, due to the non-inclusiveness of the Drell-Yan process, the total sum of cut diagrams on the right-hand side does not reproduce the cross section, but only a subset of them does. The cuts in the sum that *do* contribute to the Drell-Yan cross section are referred to as *physical cuts*. The remaining cut diagrams do not contribute to the cross section and are called *unphysical cuts*. In anticipation of a precise classification of these physical and unphysical cut diagrams, which will be given in the next subsection, we first discuss their role in the cutting equation.

The forward amplitudes $\mathscr{F}$ for the Drell-Yan process have a rich branch cut structure, which is depicted in fig. 5.6. The amplitudes have (some of) four branch cuts, along the ω-domains $(-\infty,-1]$, $(-\infty,0]$, $[0,\infty)$ or $[1,\infty)$. The branch cuts that start at the origin prevent us from defining the series coefficients of $\mathscr{F}$ at the origin, let alone making a contour deformation analogous to fig. 5.2. As will become clear in the next section, these branch cuts correspond precisely to the unphysical cut diagrams.

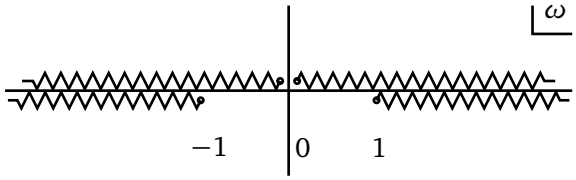

Figure 5.6: Branch cuts in a generic forward amplitude $\mathscr{F}$ for the Drell-Yan process. Compared to the analytic structure of deep inelastic scattering in fig. 5.2, there are additional branch cuts with a branch point at the origin.

The key issue, that the forward amplitude cannot be expanded around the origin, is therefore conceptually solved by restricting the sum over cuts in the cutting equation to only physical cuts, which then reads

$$\operatorname{Disc} \mathscr{F}_{\text{phys}} = \sum_{k \in \text{phys}} \operatorname{Cut}_k \mathscr{F} \ . \tag{5.12}$$

How to construct the function $\mathscr{F}_{\text{phys}}$ in practice will become clear in section 5.3.5, but for the moment it may be considered as some abstract forward amplitude that satisfies eq. (5.12). Taking the Mellin transform on both sides of this equation leads to the Drell-Yan cutting equation in Mellin space,

$$\mathscr{F}^{(n)}_{\text{phys}} = \frac{1}{2\pi i} \sum_{k \in \text{phys}} \mathscr{M}_n \big[\operatorname{Cut}_k \mathscr{F} \big] \ , \tag{5.13}$$

where $\mathscr{F}^{(n)}_{\text{phys}}$ denote the series coefficients of $\mathscr{F}_{\text{phys}}$. One of the main results in this chapter is to provide an efficient method for extracting these series coefficients from the original forward amplitude $\mathscr{F}$. The first step towards such a method is to understand precisely which cuts contribute to the right-hand side of eq. (5.12) and which cuts do not.

5.3.2. Classification of physical and unphysical cuts

We now discuss in detail the distinction between physical an unphysical cut diagrams. To set up a generic classification of different types of cut diagrams, we start by considering all possible ways to cut a forward amplitude into two subgraphs. Although the forward amplitudes depend on a single external invariant, $s = (p + \bar{p})^2$, we shall use the nomenclature of generic massless four-point amplitudes, which possess the invariants s, t and u. In this language, we distinguish four different classes of cuts, depicted in fig. 5.7, and denote them as vertex, s-channel, t-channel and u-channel cuts.

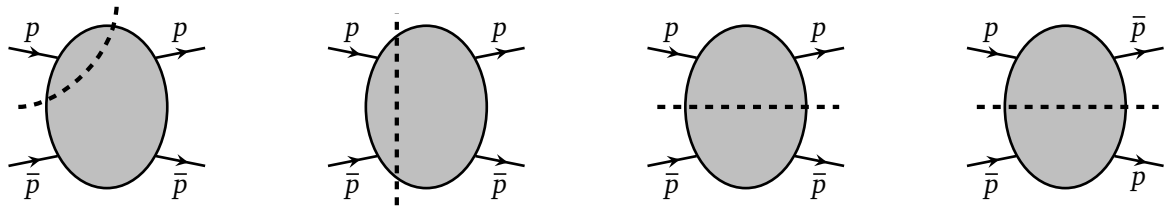

(a) vertex cut (b) s-channel cut (c) t-channel cut (d) u-channel cut

Figure 5.7: Generic cuts of forward amplitudes with two initial massless particles with momenta p and $\bar{p}$. The cuts of type (a) and (c) vanish by the general cutting rules. Note that the u-channel differs from the t-channel by interchange of the two outgoing momenta.

Among these four classes of cuts only (a subset of) the s-channel cuts contribute to the Drell-Yan cross section. All the other cuts do not contribute to the Drell-Yan cross section and are thus unphysical. Fortunately, two of these classes of cut do not need to be taken into account because they cut a forward amplitude. Firstly, the vertex cut in fig. 5.7a vanishes, because it measures the discontinuity of the forward amplitude in the p^2-channel. But this discontinuity is zero, because the forward amplitude does not actually depend on this variable due to the on-shell condition $p^2 = 0$. The same holds when any other of the four vertices is cut. By the same reasoning the t-channel cut in fig. 5.7c also vanishes. This leaves only the s- and u-channel cuts to be considered.

Taking a step further, we zoom in on the particular internal structure of the non-vanishing cut amplitudes in figs. 5.7b and 5.7d. We may then further characterize cuts as being *massive* or *massless*, depending on whether or not the cut runs through the massive propagator. The resulting four types of cuts are shown in fig. 5.8, out of which only the massive s-channel cut is physical, while the other three types of cuts are unphysical.

This distinction between massive and massless cuts is important, because it also allows us to connect each of the four types of non-vanishing cuts to discontinuities around specific branch cut in the forward amplitude. It is well known that the phase-space integration, represented by the cut in a cut diagram, comes along with a step function that enforces positive energy flow across the cut. After picking a parametrisation of the phase space, those step functions can be written in terms of the dimensionless variable $\omega = (p+\bar{p})^2/Q^2$. For the four cut diagrams (a)–(d) in fig. 5.8 the corresponding step functions are $\theta(\omega-1), \theta(\omega), \theta(-\omega)$ and $\theta(-\omega-1)$, respectively. Likewise, the discontinuity of a function contains a step

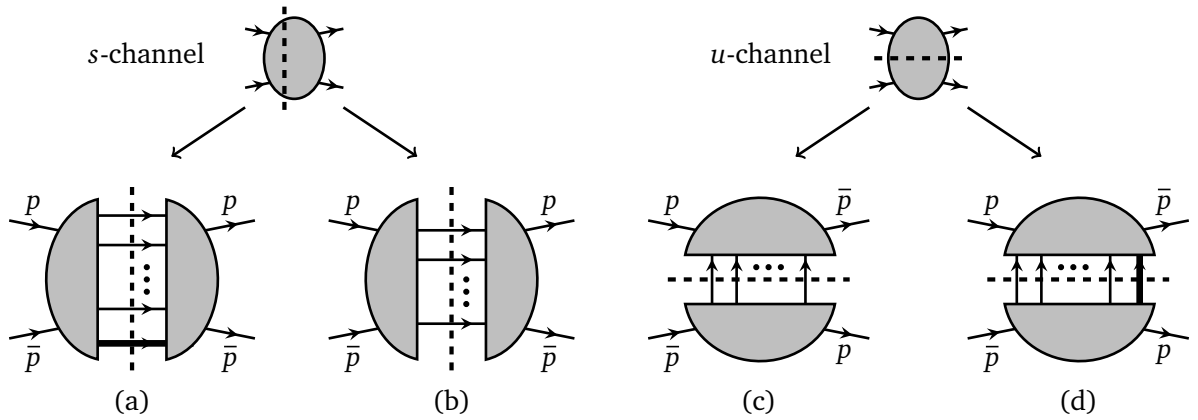

Figure 5.8: The four types of non-vanishing cut diagrams: (a) massive s-channel cut; (b) massless s-channel cut; (c) massless u-channel cut; (d) massive u-channel cut. The thick line represents the propagator of the massive photon. Only the first type of cut in this subdivision is a physical cut.

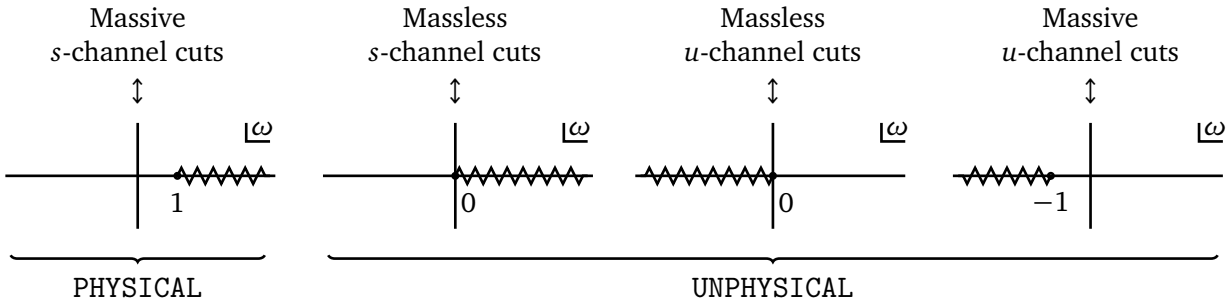

Figure 5.9: The four non-vanishing types of cut diagrams (top row) and the corresponding branch cut discontinuity in forward amplitudes. Only the first type of cut is physical, i.e. contributes to the Drell-Yan cross section.

function, which ensures that it is only non-vanishing for values along the branch cut. Consequently, the step functions in the cut diagrams tell us where the corresponding branch cut in the forward amplitude is located. This connection between the cuts and the analytic structure of the forward amplitude is displayed in fig. 5.9. In the following we shall use this observation to identify and remove the unphysical cuts from the forward amplitude.

5.3.3. Forward amplitude in terms of master integrals

The internal structure of the Drell-Yan forward amplitudes can be made more explicit by expressing them in terms of forward Feynman diagrams, which always have the same external momenta p and $\bar{p}$ and contain n loops for $\mathcal{O}(\alpha_s^n)$ corrections to the Drell-Yan cross section. At higher orders in perturbation theory, $n \geq 2$, these forward diagrams produce many Feynman integrals.

A convenient bookkeeping system for all those Feynman integrals is to write them as special case of a *topology*: a family of Feynman integrals defined by a set of propagators (each

raised to an arbitrary power) such that every scalar product between two integration momenta or between one integration momentum and one external momentum can be expressed as a linear combination of propagators and external invariants. For example,

$$T(a,b,c) = \int \mathrm{d}^{4-2\epsilon}k \, \frac{1}{(k^2)^a \left((k+p)^2\right)^b \left((k-\bar{p})^2 - Q^2\right)^c} \,, \tag{5.14}$$

is a one-loop topology, since the scalar products $k^2, k\cdot p$ and $k\cdot\bar{p}$ are all expressible in terms of the three propagators and the mass Q^2. The integrals in a topology, such as $T(a,b,c)$, differ only by the powers of the propagators, which are assumed to be integers.

All Feynman integrals in a given topology can be expressed in terms of a finite subset of independent integrals, called master integrals. The reason is that there exist many linear relations among the integrals in a topology. This stems from the observation that an integral over a total derivative vanishes in dimensional regularisation. For example,

$$\int \mathrm{d}^{4-2\epsilon}k \frac{\partial}{\partial k^\mu} \frac{v^\mu}{(k^2)^a \left((k+p)^2\right)^b \left((k-\bar{p})^2 - Q^2\right)^c} = 0 \,, \tag{5.15}$$

where v^μ can be either the loop momentum k^μ or one of the external momenta p^μ or $\bar{p}^\mu$. Equation (5.15) is known as an integration-by-parts identity (IBP). Working out the derivative on its left-hand side produces a sum of integrals that differ by the powers of the propagators and thus produces a linear recursion relation. The set of linear recursions, obtained by varying the values of (a,b,c), can be solved algorithmically with the Laporta algorithm [21]. The solution space to such a linear system is known to be finite [129, 130] and a basis for the solution space is given by a set of *master integrals*. This process of expressing Feynman integrals in terms of master integrals is known as IBP reduction.

As a result, assuming that the decomposition into master integrals can be done in practice, we write Drell-Yan forward scattering amplitudes as a combination of master integrals M_i,

$$\mathscr{F} = \sum_i C_i \, M_i \tag{5.16}$$

where the coefficients C_i are rational polynomials in ϵ and the external invariants. The computation of Feynman integrals for cross sections thus boils down to computing master integrals. Diagrammatically,

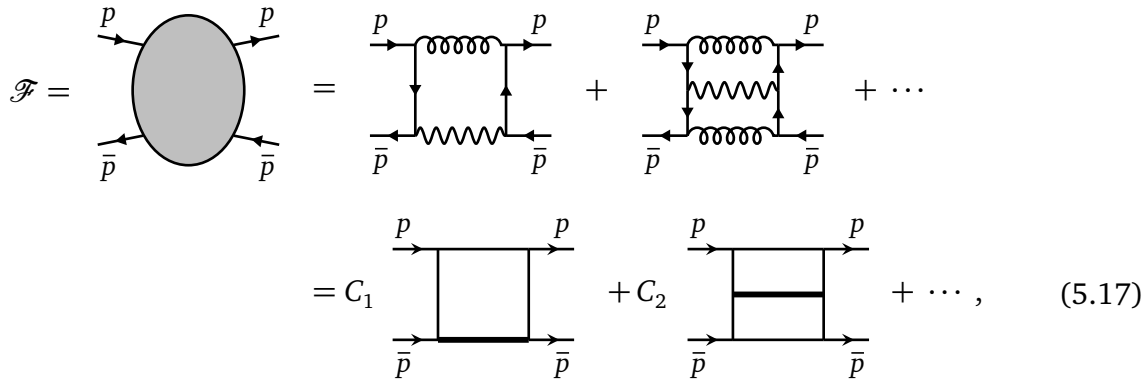

(5.17)

where the first line represents the decomposition of a Drell-Yan forward amplitude in terms of Feynman diagrams, while the second line with master integrals is obtained by IBP reduction. For this reason we focus in the remainder of this section on the application of our method on master integrals. That is, in the Mellin space cutting equation in eq. (5.13) we take $\mathscr{F}$ to be an individual master integral rather than an entire forward amplitude. The computation of such forward master integrals as a series expansion in ω, in anticipation of their role in the Mellin space cutting equation, is the topic of the next subsection.

5.3.4. Series coefficients of master integrals

Master integrals are usually computed as a Laurent series in ϵ, especially the sufficiently complicated ones. Master integrals for forward Drell-Yan amplitudes, computed in such a way, contain powers of $\log(s/Q^2) = \log\omega$. Since our aim will be to extract their series coefficients at the origin in ω-space – which is not strictly possible in the presence of such logarithmic divergences – it will be convenient to (partially) reverse the order of expansion in ϵ and ω. This approach to computing master integrals is described in this subsection.

The logarithms $\log\omega$ that appear in Drell-Yan master integrals are produced by factors ω^ϵ, upon expansion in ϵ. This non-analyticity of master integrals can be parametrized by making the following decomposition for an L-loop master integral

$$M_i(\omega,\epsilon) = \sum_{j=0}^{L} \omega^{-j\epsilon}\, g_{ij}(\omega,\epsilon)\,, \tag{5.18}$$

where the functions $g_{ij}(\omega,\epsilon)$ can be written as Taylor series in ω,

$$g_{ij}(\omega,\epsilon) = \sum_{n=0}^{\infty} c_{ij,n}(\epsilon)\,\omega^n\,. \tag{5.19}$$

The coefficients $c_{ij,n}(\epsilon)$ may be expressed as a Laurent series in ϵ, whose coefficients in turn are rational functions of n.

Example 5.1. The result for the one-loop crossed-box diagram (normalized to have zero mass dimension and with $\mu^2 = Q^2$),

$$M_i\left(\omega = \frac{s}{Q^2}\,,\,\epsilon\right) = \frac{s^2 Q^{2\epsilon}}{i\pi^{2-\epsilon} r_\Gamma} \int \frac{\mathrm{d}^{4-2\epsilon}k}{(k+p)^2(k+\bar{p})^2(k+p+\bar{p})^2(k^2-Q^2)}\,, \tag{5.20}$$

takes the form in eq. (5.18) with $L = 1$ and

$$g_{i0}(\omega,\epsilon) = \sum_{n=1}^{\infty} \frac{\Gamma(1-2\epsilon)}{\epsilon^2\,\Gamma(1-\epsilon)\Gamma(n-\epsilon)} \left(\frac{\Gamma(n+\epsilon)}{\Gamma(1+\epsilon)} - \Gamma(n)\right) \omega^n\,, \tag{5.21}$$

$$g_{i1}(\omega,\epsilon) = \sum_{n=1}^{\infty} \frac{\Gamma(1-2\epsilon)\,\Gamma(n-\epsilon)}{\epsilon^2\,\Gamma(1-\epsilon)\,\Gamma(n-2\epsilon)}\,\omega^n\,. \tag{5.22}$$

The factor $\omega^{-\epsilon}$ that multiplies g_{i1} is understood from the fact that the Feynman integral in eq. (5.20) is proportional to either $s^{-\epsilon}$ or $(Q^2)^{-\epsilon}$. Combining this with the overall prefactor, the terms contributing to M_i are proportional to either $(Q^2/s)^\epsilon = \omega^{-\epsilon}$ or to $(Q^2/Q^2)^\epsilon = \omega^0$.

The components $g_{ij}(\omega,\epsilon)$ of a set of master integrals $M_i(\omega,\epsilon)$ may be computed as solutions to appropriate differential equations. Let us outline how to obtain these. Collect into a vector $\mathbf{M}$ a set of n master integrals and organize it such that the first k master integrals are the ones that can be computed analytically by applying known formulae for bubble-type integrals. We indicate this with a superscript B (for bubble) on the first k master integrals. Then the vector of master integrals is written as $\mathbf{M} = (M_1^B, \ldots, M_k^B, M_{k+1}, \ldots, M_n)$.

The bubble-type integrals M_i^B are known exactly in ϵ, so they can serve as inhomogeneous terms for differential equations for the remaining unknown M_i. This works as follows. Gather the unknown integrals in the vector $\overline{\mathbf{M}} = (M_{k+1}, \ldots, M_n)$, take its derivative with respect to ω and reduce the result with IBP identities to master integrals. This yields a system of first-order coupled differential equations, which takes the form $\frac{d}{d\omega}\overline{\mathbf{M}} = \mathbf{A}\cdot\mathbf{M}$ for some matrix $\mathbf{A}$ of rational functions. The right-hand side depends on *all* master integrals, which can be avoided by decoupling the differential equations at the expense of raising the order of the differential equations (see for example [23]). As a result, the differential equation for a given integral M_i will be of some order r in the range $1 \le r \le n-k$, depending on the particular system, and takes the form

$$\left(\sum_{m=0}^{r} a_{im}\,\frac{\mathrm{d}^m}{\mathrm{d}\omega^m}\right) M_i(\omega,\epsilon) = \left(\sum_{j=1}^{k}\sum_{m=0}^{r-1} b_{ijm}\,\frac{\mathrm{d}^m}{\mathrm{d}\omega^m}\,M_j^B(\omega,\epsilon)\right)\,. \tag{5.23}$$

Here, the free index i labels the unknown master integrals, $k+1 \le i \le n$, and the coefficients a_{im} and b_{ijm} are some rational functions of ω and ϵ. We emphasize that the right-hand side is known exactly in ϵ, since it consists of the known bubble-type integrals and derivatives thereof.

Inserting the decomposition of M_i in terms of the g_{ij} in eq. (5.18) into the differential equation in eq. (5.23) produces differential equations for the individual g_{ij}. Furthermore, substituting the latter by their Taylor series in eq. (5.19) leads to *difference equations* in the

discrete variable n for the series coefficients $c_{ij,n}(\epsilon)$ of the form

$$H_{0,n}(\epsilon)\, c_{ij,n}(\epsilon) + H_{1,n}(\epsilon)\, c_{ij,n+1}(\epsilon) + \cdots + H_{r',n}(\epsilon)\, c_{ij,n+r'}(\epsilon) = H_n(\epsilon)\,, \tag{5.24}$$

for given i, j and some fixed rank r', which depends on the particular calculation. In simple cases, one can solve this difference equation exactly in ϵ.

Example 5.2. The one-loop box diagram is $B_1 = \mathscr{C}(\epsilon)(Q^2)^\epsilon s^2\, T(2,1,1)$, where $T(a,b,c)$ was defined in eq. (5.14). Setting $v^\mu = k^\mu$ or p^μ in eq. (5.15) and adding the two resulting IBPs yields a differential equation for B_1,

$$\left[(-1-\epsilon-\epsilon\,\omega) + (s-Q^2)\frac{\partial}{\partial Q^2}\right] B_1(\omega,\epsilon) = \frac{\Gamma(1-2\epsilon)}{\epsilon\,\Gamma(1-\epsilon)^2}\,\omega^2\,. \tag{5.25}$$

Inserting the series ansatz $B_1 = \sum_n c_n \omega^n$ and equating terms with equal powers of ω on both sides leads to a recursion in n,

$$c_2(\epsilon) = \frac{\Gamma(1-2\epsilon)}{\epsilon\,\Gamma(1-\epsilon)\,\Gamma(2-\epsilon)}\,, \quad c_n(\epsilon) = \frac{n-1+\epsilon}{n-1-\epsilon}\, c_{n-1}(\epsilon) \quad \text{for } n > 2\,, \tag{5.26}$$

which is readily solved in terms of Gamma functions,

$$c_n(\epsilon) = \frac{1}{\epsilon\,(1+\epsilon)}\,\frac{\Gamma(1-2\epsilon)}{\Gamma(1-\epsilon)\Gamma(1+\epsilon)}\,\frac{\Gamma(n+\epsilon)}{\Gamma(n-\epsilon)}\,. \tag{5.27}$$

This result for the series coefficients of B_1 fully agrees with a more direct calculation of the box integral and is exact in ϵ.

In some other cases, an exact solution (in ϵ) to the difference equation in eq. (5.24) is not known and one is forced to seek a solution order-by-order in ϵ. One way to proceed is by making an ansatz of the form

$$c_{ij,n}(\epsilon) = \sum_{k,\vec{\ell},m} A_{ij,k\vec{\ell}m}\, \epsilon^k\, S_{\vec{\ell}}(n-m)\,, \tag{5.28}$$

with some conservative choices for the summation variables. Here, the functions $S_{\vec{\ell}}(n)$ are harmonic sums, whose properties are well-known [131], as discussed in appendix B. The unknown coefficients $A_{ij,k\vec{\ell}m}$ contain both rational and transcendental numbers, and may be determined as follows. The simplest approach is to evaluate the difference equation for $c_{ij,n}$ at suitably many values of n, so as to obtain a system of equations which may be solved for the unknown $A_{ij,k\vec{\ell}m}$. In a more sophisticated method [132] each term in the difference equation for $c_{ij,n}$ is projected onto a basis of synchronized harmonic numbers, after which the coefficients of each harmonic number is equated to zero. This also yields a system of equations for the $A_{ij,k\vec{\ell}m}$. We have implemented both techniques and successfully applied them to the two-loop examples below in section 5.4.

In summary, after having computed the series coefficients $c_{ij,n}(\epsilon)$, either exact in ϵ or as a Laurent series in this parameter, the latter effectively provide a solution to the master integrals through eq. (5.18). This is the starting point for the next subsection, where we

explain how to extract the Mellin moments of the physical Drell-Yan cuts from these master integral coefficients.

5.3.5. Removal of unphysical cut contributions

Having computed master integrals we now turn to extract the Mellin moments of their physical cuts. Equivalently, we can remove contributions from unphysical cuts to the discontinuity of master integrals for a forward amplitude. As shown in fig. 5.9, there are three such unphysical contributions: massless s- and u- channel cuts, as well as massive u-channel cuts. Removing the first two contributions rests on the decomposition in eq. (5.18) and is achieved by a shifting procedure, which will be explained below. The massive unphysical u-channel cut is different and we show how its contribution is eliminated with a set of diagram-independent replacement rules.

The massless types of unphysical cuts correspond to branch cuts in forward amplitudes with the branch point at the origin $\omega = 0$. Such branch cuts arise from the factors $\omega^{-j\epsilon}$ in the decomposition of master integrals (combining eq. (5.18) and eq. (5.19)),

$$M_i(\omega,\epsilon) = \sum_{n=0}^{\infty}\sum_{j=0}^{L} c_{ij,n}(\epsilon)\,\omega^{n-j\epsilon} \ . \tag{5.29}$$

The *shifting procedure* is defined by the replacement $n \to n + j\epsilon$ in the summand, but not in the lower bound of the sum on n. This produces the *new* function

$$\widetilde{M}_i(\omega,\epsilon) = \sum_{n=0}^{\infty}\sum_{j=0}^{L} c_{ij,n+j\epsilon}(\epsilon)\,\omega^{n} \ . \tag{5.30}$$

Evidently, this modified version of the master integral no longer contains powers ω^{ϵ} and thus produces no logarithms $\log\omega$ upon expansion in ϵ. therefore, $\widetilde{M}_i(\omega,\epsilon)$ is free of unphysical branch cuts that start at the origin. In other words, the discontinuity of $\widetilde{M}_i(\omega,\epsilon)$ receives contributions from only the massive s- and u-channel cut diagrams (see fig. 5.9). We do need to ensure ourselves, though, that altering the forward amplitude in this way does not destroy the connection between the discontinuity around the physical branch of the forward amplitude and the sum of physical cut diagrams. Let us first clarify this issue through some toy examples.

Example 5.3. Consider a "forward amplitude" given by

$$f_1(\omega) = \frac{\omega^{-\epsilon}}{1-\omega} = \sum_{n=0}^{\infty}\omega^{n-\epsilon} \ . \tag{5.31}$$

Applying the shifting procedure, we arrive at the new function

$$\widetilde{f}_1(\omega) = \sum_{n=0}^{\infty} \omega^n = \frac{1}{1-\omega} \,. \tag{5.32}$$

While the original function has its branch cut along the negative real axis removed, both functions have the same pole structure in the region $\omega \geq 1$, namely

$$\underset{\omega\geq 1}{\text{Disc}}\, f_1(\omega) = 2\pi i\, \delta(1-\omega) = \underset{\omega\geq 1}{\text{Disc}}\, \widetilde{f}_1(\omega) \,. \tag{5.33}$$

Therefore in this example the discontinuity in the physical region is unaltered by the shifting procedure.

Example 5.4. A second example is given by a function with a branch cut in the physical region, which mimics the analytic structure of a typical Feynman integrals more closely,

$$f_2(\omega) = -\log(1-\omega)\,\omega^{-\epsilon} = \sum_{n=1}^{\infty} \frac{1}{n}\,\omega^{n-\epsilon} \,. \tag{5.34}$$

The shifting procedure produces

$$\widetilde{f}_2(\omega) = \sum_{n=1}^{\infty} \frac{1}{n+\epsilon}\,\omega^{n} \,. \tag{5.35}$$

Again, these two functions have the same discontinuity in the physical region. This is most easily verified upon writing both functions as an expansion in ϵ,

$$\begin{aligned} f_2(\omega) &= -\log(1-\omega) \sum_{k=0}^{\infty} (-\epsilon)^k \,\frac{\log^k(\omega)}{k!} \,, \\ \widetilde{f}_2(\omega) &= \sum_{k=0}^{\infty} (-\epsilon)^k \,\text{Li}_{k+1}(\omega) \,. \end{aligned} \tag{5.36}$$

Using the identities

$$\begin{aligned} \underset{\omega\geq 1}{\text{Disc}}\, \big[\log(1-\omega)\log^k(w)\big] &= -2\pi i\, \log^k(\omega) \,, \\ \underset{\omega\geq 1}{\text{Disc}}\, \big[\text{Li}_{k+1}(\omega)\big] &= 2\pi i\, \frac{\log^k(\omega)}{k!} \,, \end{aligned} \tag{5.37}$$

one readily confirms that the discontinuity of $f_2(\omega)$ in the physical region is equal to that of $\widetilde{f}_2(\omega)$ and is thus unaltered by the shifting procedure.

The results of the shifting procedure are modified master integrals $\widetilde{M}_i(\omega,\epsilon) = \sum_{n=0}^{\infty} \widetilde{c}_{i,n}\omega^n$, whose series coefficients are given by $\widetilde{c}_{i,n}(\epsilon) = \Big(\sum_{j=0}^{L} c_{ij,n+j\epsilon}(\epsilon)\Big)$. This begs the question what the shifted coefficients $c_{ij,n+j\epsilon}(\epsilon)$ look like. If the original $c_{ij,n}(\epsilon)$ are known exact in ϵ in terms of Gamma functions, like in eq. (5.27), then the shifted coefficients are simply the same expressions with slightly different arguments for the Gamma functions. But it can also happen that the original coefficients are known order-by-order in ϵ in terms of harmonic

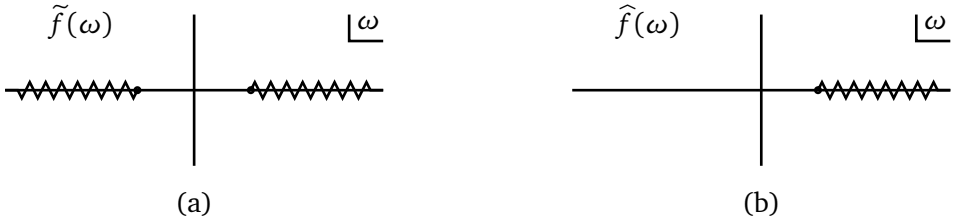

Figure 5.10: The analytic structure of the example functions $\widetilde{f}(\omega)$ and $\widehat{f}(\omega)$, given in eq. (5.38) and eq. (5.44), respectively. The function $\widetilde{f}(\omega)$ represents a forward diagram, whose discontinuity contains contributions from both physical and un-physical cut diagrams. The second function, $\widehat{f}(\omega)$, is a modified version of the forward, such that only the physical branch cut is present.

numbers $S_{\vec{\ell}}(n)$, see eq. (5.28). In that case, the shifted coefficients will contain harmonic numbers at non-integer values, $S_{\vec{\ell}}(n+j\epsilon)$, for which the sum definition does not make sense. In other words, we need to know the analytic continuation of harmonic numbers from the positive integers to the real line. This has been investigated in the literature and appendix B.2 provides a brief review thereof.

After applying the shifting procedure, the discontinuity of the master integrals for forward amplitudes are the sum of only two contributions: physical s-channel cuts and unphysical u-channel cuts. The final step is to remove the last unphysical cut. To this end, we use essentially the same idea as before and modify the master integrals once again, in such a way that the unphysical branch cut along $\omega \in (-\infty, -1]$ is removed while the physical branch cut along $\omega \in [1, \infty)$ remains unchanged. Our technique for obtaining a function that satisfies these requirements is again best illustrated at first with the help of an example.

Example 5.5. Consider the following product of logarithms, denoted $\widetilde{f}(\omega)$ in view of the absence of a branch point at $\omega = 0$,

$$\widetilde{f}(\omega) = \log(1+\omega)\log(1-\omega)\,. \tag{5.38}$$

In the complex ω-plane this function $\widetilde{f}(\omega)$ has two branch cuts, which are located along the disconnected intervals $(-\infty, -1]$ and $[1, \infty)$. This situation is shown in fig. 5.10(a). The discontinuity of $\widetilde{f}(\omega)$ is simply the sum of the discontinuities around the individual branch cuts:

$$\underset{\omega}{\text{Disc}}\,\widetilde{f}(\omega) = 2\pi i \log(1-\omega)\theta(-\omega-1) - 2\pi i \log(1+\omega)\theta(\omega-1)\,. \tag{5.39}$$

In eq. (5.39), the first term on the right-hand side may be interpreted as a contribution coming from unphysical cut diagrams. Removing the unphysical cuts thus amounts to removing the branch cut along $(-\infty, -1]$ from the function $\widetilde{f}(\omega)$, leaving a new function, $\widehat{f}(\omega)$, such that

$$\underset{\omega}{\text{Disc}}\,\widehat{f}(\omega) = -2\pi i \log(1+\omega)\theta(\omega-1)\,. \tag{5.40}$$

The corresponding analytic structure is displayed in fig. 5.10b. The question is how to find $\widehat{f}(\omega)$.

Note that there is no unique answer to this question. Indeed, any constant (or smooth function, for that matter) may be added without changing the discontinuity. This ambiguity is lifted by

imposing the constraint $\widehat{f}(0) = 0$, which reflects the physical property of scattering cross-sections that they vanish in the limit of zero center-of-mass energy. This constraint, together with the analyticity of $\widehat{f}(\omega)$ around the origin, allows us to write down a series representation

$$\widehat{f}(\omega) = \sum_{n=1}^{\infty} \widehat{c}_n \, \omega^n \, . \tag{5.41}$$

The coefficients $\widehat{c}_n$ can be obtained from the Cauchy integral formula, taking a small contour enclosing the origin. Inflating the contour such that it wraps around the branch cut, the contour integral becomes the integration of the discontinuity along the real line, analogous to the discussion for DIS in section 5.1. Subsequently changing variables to the reciprocal $z = 1/\omega$ leads to the following Mellin-transform integral

$$\widehat{c}_n = -\int_0^1 \mathrm{d}z \, z^{n-1} \log(1 + \tfrac{1}{z}) \, . \tag{5.42}$$

This standard integral transform may be performed (for more complicated cases one may use the MT package [133]) and the resulting coefficients are

$$\widehat{c}_n = -\frac{1}{n^2} + \frac{(-1)^n S_{-1}(n)}{n} - \frac{\log 2}{n} + \frac{(-1)^n \log 2}{n} \, . \tag{5.43}$$

In the analogy with perturbative computations, these coefficients correspond to the Mellin moments of the sum of cut diagrams obtained from the forward $\widetilde{f}(\omega)$ by taking all possible physical cuts. Considering the aim of this paper, these moments therefore provide a satisfactory answer.

For completeness, let us mention that it is also possible to reconstruct the function $\widehat{f}(\omega)$ in eq. (5.41). Using algorithm B.2 in appendix B, one first rewrite the harmonic numbers in a convenient form. Based on the fact that the generating function of harmonic sums are harmonic polylogarithms, one subsequently constructs the function $\widehat{f}(\omega)$ by means of the formulas in appendix B.3. The result, which indeed has the branch cut structure in fig. 5.10b, is given by

$$\begin{aligned} \widehat{f}(\omega) &= -H_{-1,1}(\omega) - \log 2 \, H_{-1}(\omega) - \log 2 \, H_1(\omega) \\ &= -\operatorname{Li}_2\Big(\frac{1+\omega}{2}\Big) + \log 2 \, \log(1-\omega) - \frac{\log^2 2}{2} + \frac{\pi^2}{12} \, . \end{aligned} \tag{5.44}$$

The methods in example 5.5 for removing the unphysical branch cut can be applied more generally to master integrals for Drell-Yan forward amplitudes. Apart from branch cuts, one then also deals with poles, typically at $\omega = 1$. One simple way to implement the removal of the wrong branch cut is by deriving replacement rules for the individual harmonic numbers, which appear in the result of the shifting procedure eq. (5.30). For a given harmonic number $S_{\vec{\ell}}(n)$, one first evaluates the corresponding sum $\sum_n S_{\vec{\ell}}(n) \, \omega^n$ in closed form. This step is purely mathematical and is explained in appendix B.3. Based on similar analysis as in the previous example, one then constructs a function which has the unphysical branch cut removed and whose series coefficients define the replacement of $S_{\vec{\ell}}(n)$. For example, in

the case of $S_{1,-2}(n)$ we get

$$\sum_{n=1}^{\infty} S_{1,-2}(n)\,\omega^n \;=\; \frac{H_{-3}(\omega)+H_{1,-2}(\omega)}{\omega-1}$$
$$\to\; \frac{4\,\zeta_2\,H_1(\omega)+\omega\,\zeta_3}{8\,(\omega-1)} \;=\; \sum_{n=1}^{\infty}\Big(-\tfrac{1}{2}S_1(n)-\tfrac{1}{8}\zeta_3\Big)\,\omega^n\,, \qquad (5.45)$$

which is equivalent to the effective replacement rule $S_{1,-2}(n) \to -\frac{1}{2}S_1(n) - \frac{1}{8}\zeta_3$. Following these steps with all harmonic sums produces a list of replacement rules, in which alternating harmonic sums (sums with at least one negative index) are replaced by their asymptotic expansion at $n \to \infty$ [134]. The resulting 'dictionary' may be applied to any diagram. We shall use such replacement rules in section 5.4.2.

5.4. Application to two-loop diagrams

The procedures we developed in the previous section 5.3 have been put to practice, by applying them to various one- and two-loop diagrams [5]. In this thesis we show two examples, a two-loop self-energy diagram and a two-loop crossed-box diagram, which demonstrate all key aspects of the procedures. Referring back to the four types of non-vanishing cut amplitudes (see fig. 5.8), these two diagrams together cover all possible unphysical cuts, as shown in fig. 5.11.

We use the two-loop self energy diagram to demonstrate our shifting procedure and to provide details on the calculation of the Mellin moments to all orders in ϵ. The two-loop crossed-box diagram is a non-trivial example which requires the replacement rules as well as techniques to solve for the Mellin moments order-by-order in ϵ. The two examples are presented in turn below.

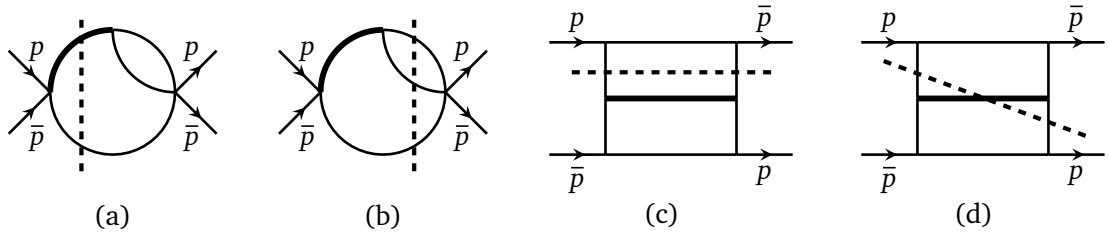

Figure 5.11: Examples of the non-vanishing cut diagrams: (a,b) massive and massless s-channel cuts of a self-energy diagram; (c,d) massless and massive u-channel cuts of a crossed-box diagram.

5.4.1. Two-loop self-energy diagram

In our first two-loop example we study a forward self-energy diagram, whose cutting equation is depicted in fig. 5.12. As illustrated in the figure, the forward diagram admits two cuts: a two- and a three-particle cut. The two-particle cut is physical, but the three-particle cut is an unphysical s-channel cut which needs to be removed from the forward. In this subsection we show how to compute the physical cut from the forward diagram and point out the differences with a direct calculation the cut diagram.

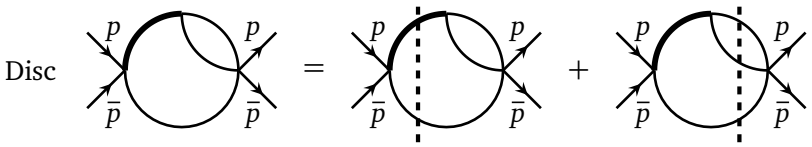

Figure 5.12: Cutting equation for a two-loop self-energy diagram.

Let us start by computing the forward diagram, before proceeding to remove the unphysical cut in order to extract the moments of the physical cut. The forward two-loop self-energy diagram is given by

$$S = \left(\mathscr{C}(\epsilon)Q^{2\epsilon}\right)^2 G_{1,1,1,1,0}\,, \tag{5.46}$$

where $\mathscr{C}(\epsilon) = (i\pi^{2-\epsilon}r_\Gamma)^{-1}$ and $G_{1,1,1,1,0}$ is embedded in the integral topology

$$G_{a_1,a_2,a_3,a_4,a_5} = \int \frac{\mathrm{d}^{4-2\epsilon}k\;\mathrm{d}^{4-2\epsilon}\ell}{(k^2-Q^2)^{a_1}\left((k+P)^2\right)^{a_2}\left(\ell^2\right)^{a_3}\left((\ell+k)^2\right)^{a_4}\left((\ell+P)^2\right)^{a_5}}\,, \tag{5.47}$$

where $P = p+\bar{p}$. We proceed to compute $G_{1,1,1,1,0}$ by establishing an appropriate differential equation. To this end, notice that raising the power of the massive propagator may be achieved by differentiation with respect to the mass Q^2, that is

$$G_{2,1,1,1,0} = \frac{\mathrm{d}}{\mathrm{d}Q^2}G_{1,1,1,1,0}\,. \tag{5.48}$$

Using IBP reduction, the integral on the left-hand side can be expressed in terms of simpler integrals

$$G_{2,1,1,1,0} = -\frac{\left(Q^2+(s-3Q^2)\epsilon\right)G_{1,1,1,1,0}}{Q^2\left(s-Q^2\right)} - \frac{(2-3\epsilon)G_{0,1,1,1,0}}{Q^2\left(s-Q^2\right)} + \frac{(1-\epsilon)G_{1,0,1,1,0}}{Q^2\left(s-Q^2\right)}\,. \tag{5.49}$$

The first integral on the right-hand side is the self-energy diagram at hand (up to a prefactor), the integral on the left-hand side is its derivative, and the last two integrals on the right-hand side are simpler bubble-type integrals. The latter can readily be computed

exactly in ϵ, and read

$$G_{0,1,1,1,0} = R_1(\epsilon) s^{1-2\epsilon} \qquad \text{with } R_1(\epsilon) = -\frac{\pi^{4-2\epsilon}\,\Gamma(1-\epsilon)^3\Gamma(-1+2\epsilon)}{\Gamma(3-3\epsilon)}\, e^{2i\pi\epsilon}\,, \tag{5.50}$$

$$G_{1,0,1,1,0} = R_2(\epsilon) (Q^2)^{1-2\epsilon} \quad \text{with } R_2(\epsilon) = \frac{\pi^{4-2\epsilon}\,\Gamma(1-\epsilon)^2\Gamma(\epsilon)\Gamma(-1+2\epsilon)}{\Gamma(2-\epsilon)}\,. \tag{5.51}$$

Here we have performed the analytic continuation $(-s)^{-2\epsilon} \equiv (-s - i0)^{-2\epsilon} = e^{2i\pi\epsilon} s^{-2\epsilon}$. Inserting eqs. (5.48), (5.50) and (5.51) into eq. (5.49) thus produces a first-order linear differential equation for the integral $G_{1,1,1,1,0}$. Exchanging the latter for S, see eq. (5.46), yields the following differential equation

$$\left((1-\epsilon-\epsilon\,\omega) - (1-\omega)Q^2\frac{\mathrm{d}}{\mathrm{d}Q^2}\right) S = -(2-3\epsilon)\,\mathscr{C}(\epsilon)^2 R_1(\epsilon)\,\omega^{1-2\epsilon} + (1-\epsilon)\,\mathscr{C}(\epsilon)^2 R_2(\epsilon)\,. \tag{5.52}$$

As discussed in the previous subsection, we now insert a series ansatz for S into this differential equation, so as to turn it into a difference equation for the series coefficients. From the inhomogeneous terms in eq. (5.52) one can infer that the forward diagrams will have the structure $S = g_0(\omega) + \omega^{-2\epsilon} g_2(\omega)$, where $g_0(\omega)$ and $g_2(\omega)$ are regular functions of ω close to the origin. We thus proceed to make the series ansatz

$$S = \sum_{n=0}^{\infty} c_n\,\omega^n + \sum_{n=0}^{\infty} e_n\,\omega^{n-2\epsilon}\,. \tag{5.53}$$

Inserting this into eq. (5.52) yields

$$\begin{aligned} 0 = &\sum_{n=1}^{\infty} c_{n-1}(n-1+\epsilon)\omega^n - \sum_{n=0}^{\infty} c_n(n+1-\epsilon)\omega^n \\ &+ \sum_{n=1}^{\infty} e_{n-1}(n-1-\epsilon)\omega^{n-2\epsilon} - \sum_{n=0}^{\infty} e_n(n+1-3\epsilon)\omega^{n-2\epsilon} \\ &- (2-3\epsilon)\mathscr{C}(\epsilon)^2 R_1(\epsilon)\omega^{1-2\epsilon} + (1-\epsilon)\mathscr{C}(\epsilon)^2 R_2(\epsilon)\,. \end{aligned} \tag{5.54}$$

Equating same powers of ω produces two recursions, complete with boundary conditions:

$$c_n = \left(\frac{n-1+\epsilon}{n+1-\epsilon}\right) c_{n-1} \quad \text{for } n>0\,, \quad c_0 = \mathscr{C}(\epsilon)^2 R_2(\epsilon)\,, \tag{5.55}$$

$$e_n = \left(\frac{n-1-\epsilon}{n+1-3\epsilon}\right) e_{n-1} \quad \text{for } n>1\,, \quad e_1 = -\mathscr{C}(\epsilon)^2 R_1(\epsilon)\,, \quad e_0 = 0\,. \tag{5.56}$$

The solutions to these elementary recursions are ratios of gamma functions,

$$c_n = \mathscr{C}(\epsilon)^2 R_2(\epsilon) \frac{\Gamma(2-\epsilon)}{\Gamma(\epsilon)} \frac{\Gamma(n+\epsilon)}{\Gamma(n+2-\epsilon)} \quad \text{for } n \geq 0 \,, \tag{5.57}$$

$$e_n = -\mathscr{C}(\epsilon)^2 R_1(\epsilon) \frac{\Gamma(3-3\epsilon)}{\Gamma(1-\epsilon)} \frac{\Gamma(n-\epsilon)}{\Gamma(n+2-3\epsilon)} \quad \text{for } n \geq 1 \,. \tag{5.58}$$

As a result, the forward self-energy diagram S is now known as a series expansion in ω around the origin:

$$S = -\frac{\Gamma(1-2\epsilon)^2\Gamma(-1+2\epsilon)}{\Gamma(1-\epsilon)^2\Gamma(1+\epsilon)^2} \left(\sum_{n=0}^{\infty} \frac{\Gamma(n+\epsilon)}{\Gamma(n+2-\epsilon)} \omega^n + e^{2i\pi\epsilon} \sum_{n=1}^{\infty} \frac{\Gamma(n-\epsilon)}{\Gamma(n+2-3\epsilon)} \omega^{n-2\epsilon} \right) . \tag{5.59}$$

These series can easily be recognized as representations of ${}_2F_1$-hypergeometric functions, but for our purposes the current form is actually more useful. Indeed, the aim of the remainder of this section is to extract the Mellin moments of the physical cut in fig. 5.12 from the forward amplitude diagram in eq. (5.59).

Extracting the Mellin moments of the physical cut from the forward is done in the following way. We construct a new function $\widetilde{S}$, which has the same branch cut discontinuity as S around $\omega \in [1, \infty)$, but does not possess a branch cut starting at the origin $\omega = 0$. In practice, we find such a function by means of the shifting procedure, as explained in section 5.3.5. Applied to the series in eq. (5.59) this produces

$$S \longrightarrow \widetilde{S} = -\left(1 + e^{2i\pi\epsilon}\right) \frac{\Gamma(1-2\epsilon)^2\Gamma(-1+2\epsilon)}{\Gamma(1-\epsilon)^2\Gamma(1+\epsilon)^2} \sum_{n=1}^{\infty} \frac{\Gamma(n+\epsilon)}{\Gamma(n+2-\epsilon)} \omega^n \,. \tag{5.60}$$

where we dropped an ω-independent term, without affecting the discontinuity. The series coefficients of this new function $\widetilde{S}$ (in contrast to S) are well-defined. If we write $\widetilde{S} = \sum_{n=1}^{\infty} \widetilde{c}_n \omega^n$, then its series coefficients $\widetilde{c}_n$ are equal to

$$\widetilde{c}_n = -\left(1 + e^{2i\pi\epsilon}\right) \frac{\Gamma(1-2\epsilon)^2\Gamma(-1+2\epsilon)}{\Gamma(1-\epsilon)^2\Gamma(1+\epsilon)^2} \frac{\Gamma(n+\epsilon)}{\Gamma(n+2-\epsilon)} \,. \tag{5.61}$$

Based on our arguments presented in the previous section we claim that these series coefficients provide the Mellin moments of the physical cut on the right-hand side of the cutting equation in fig. 5.12. The coefficients in eq. (5.61) therefore constitute the main result of this example.

Let us now verify our claim. To this end we shall compute the physical cut diagram explicitly. One way to proceed is by applying reverse unitarity [22] to the IBP reduction in eq. (5.49), in order to derive a differential equation for the cut diagram. Alternatively, one may actually perform the phase-space integration directly. In the latter approach one simply integrates a massless sub-bubble over a two-particle (one-mass) phase space. The

massless sub-bubble reads

$$\text{Bub} = i\pi^{2-\epsilon}\,\frac{\Gamma(1-\epsilon)^2\,\Gamma(\epsilon)}{\Gamma(2-2\epsilon)}\,\frac{1}{(-k^2)^\epsilon}\,. \tag{5.62}$$

Because the massive line is cut, $k^2 = Q^2$, the bubble can be pulled out of the phase-space integral. As a result, the cut diagram is given by

$$\text{Cut}_{\text{phys}}\,S = 2\pi i\,e^{i\pi\epsilon}\,z^\epsilon(1-z)^{1-2\epsilon}\frac{\Gamma(1-2\epsilon)^2\,\Gamma(\epsilon)}{\Gamma(2-2\epsilon)^2\,\Gamma(1-\epsilon)\,\Gamma(1+\epsilon)^2}\,. \tag{5.63}$$

The Mellin moments can be computed exactly in ϵ due to the simple dependence on z. They are given by

$$\mathscr{M}_n\Big[\text{Cut}_{\text{phys}}\,S\Big] = 2\pi i\,e^{i\pi\epsilon}\frac{\Gamma(1-2\epsilon)^2\,\Gamma(\epsilon)}{\Gamma(2-2\epsilon)\,\Gamma(1-\epsilon)\,\Gamma(1+\epsilon)^2}\frac{\Gamma(n+\epsilon)}{\Gamma(n+2-\epsilon)}\,. \tag{5.64}$$

Comparing this expression to the series coefficients in eq. (5.61), and making use of the identity $\Gamma(1-2\epsilon)\Gamma(1+2\epsilon)\left(1+e^{2i\pi\epsilon}\right) = 2\Gamma(1-\epsilon)\Gamma(1+\epsilon)e^{i\pi\epsilon}$, we can verify that

$$\widetilde{c}_n = \frac{1}{2\pi i}\mathscr{M}_n\Big[\text{Cut}_{\text{phys}}\,S\Big]\,. \tag{5.65}$$

This relation holds at all orders in ϵ, as claimed.

5.4.2. Two-loop crossed-box diagram

We turn to our second example: the two-loop crossed-box diagram, depicted in fig. 5.13. This diagram is distinguished from previous examples in two key aspects. First, it is sufficiently complicated so that it cannot be calculated exactly in ϵ, thereby providing a testing ground for the techniques of the previous subsection for computing the series coefficients of forward diagrams order-by-order in ϵ from differential equations. Second, the diagram is the first example to admit a massive u-channel cut, for which a new procedure was developed also in the previous subsection. In the example below we focus on these two aspects: first we compute the forward diagram, after which the moments of the physical cut are recovered by means of the shifting procedure and the replacement rules. We finally cross-check our results against the literature.

Our first task is to compute the crossed-box diagram in fig. 5.13. It may be written as

$$B_2 = \left(\mathscr{C}(\epsilon)Q^{2\epsilon}\right)^2 s^3\;G_{1,1,1,1,1,1,1}\,, \tag{5.66}$$

where $G_{1,1,1,1,1,1,1}$ is one of the integrals in the following two-loop double-box topology

$$G_{a_1,a_2,a_3,a_4,a_5,a_6,a_7} = \int\frac{\mathrm{d}^{4-2\epsilon}k\;\mathrm{d}^{4-2\epsilon}\ell}{D_1^{a_1}\,D_2^{a_2}\,D_3^{a_3}\,D_4^{a_4}\,D_5^{a_5}\,D_6^{a_6}\,D_7^{a_7}}\,, \tag{5.67}$$

where the denominators D_i are given by

$$\begin{aligned} &D_1 = k^2\,, && D_2 = (k+p)^2\,, && D_3 = (k+\bar{p})^2\,, && D_4 = (\ell+p)^2\,, \\ &D_5 = (\ell+\bar{p})^2\,, && D_6 = (\ell+p+\bar{p})^2\,, && D_7 = (k-\ell)^2 - Q^2\,. \end{aligned} \tag{5.68}$$

There are fourteen master integrals for the topology in eq. (5.67). We use the following set of master integrals, as provided by LiteRed [135, 136],

$$\begin{aligned} &M_1^B = G_{0,0,0,1,1,0,1}\,, && M_2^B = G_{0,0,1,0,0,1,1}\,, && M_3^B = G_{0,0,1,0,1,0,1}\,, \\ &M_4^B = G_{0,0,1,1,0,0,1}\,, && M_5^B = G_{1,0,0,0,0,1,1}\,, && M_6^B = G_{0,0,2,1,0,0,1}\,, \\ &M_7^B = G_{2,0,0,0,0,1,1}\,, && M_8^B = G_{0,1,1,1,1,0,0}\,, && \\ &M_9 = G_{0,1,1,0,0,1,1}\,, && M_{10} = G_{0,1,1,0,1,1,1}\,, && M_{11} = G_{0,1,1,1,1,0,1}\,, \\ &M_{12} = G_{0,2,1,0,0,1,1}\,, && M_{13} = G_{1,0,1,0,1,1,1}\,, && M_{14} = G_{1,1,1,1,1,1,1}\,. \end{aligned} \tag{5.69}$$

The integral of interest is the last (and most complicated) master integral M_{14}. Following the notation introduced in section 5.3.4, the first eight integrals are marked with the superscript "B" to indicate that they can be readily computed as iterated bubble integrals. These integrals are

$$\begin{aligned} M_1^B &= \frac{\pi^{4-2\epsilon} s^{1-2\epsilon} \omega^{-1+\epsilon} \Gamma(1-\epsilon)^2 \Gamma(-1+\epsilon)\Gamma(\epsilon)}{\Gamma(2-2\epsilon)}\,, \\ M_2^B &= \frac{\pi^{4-2\epsilon} s^{1-2\epsilon} \omega^{-1+2\epsilon} \Gamma(1-\epsilon)^2 \Gamma(\epsilon)\Gamma(-1+2\epsilon)}{\Gamma(2-\epsilon)}\,, \\ M_3^B &= \frac{\pi^{4-2\epsilon} s^{1-2\epsilon} \omega^{-1+2\epsilon} \Gamma(1-\epsilon)^2 \Gamma(\epsilon)\Gamma(-1+2\epsilon)}{\Gamma(2-\epsilon)}\,, \\ M_4^B &= \frac{\pi^{4-2\epsilon} s^{1-2\epsilon} \omega^{-1+2\epsilon} \Gamma(1-\epsilon)^2 \Gamma(\epsilon)\Gamma(-1+2\epsilon)\, {}_2F_1(\epsilon, -1+2\epsilon; 2-\epsilon; -\omega)}{\Gamma(2-\epsilon)}\,, \\ M_5^B &= \frac{\pi^{4-2\epsilon} s^{1-2\epsilon} \omega^{-1+2\epsilon} \Gamma(1-\epsilon)^2 \Gamma(\epsilon)\Gamma(-1+2\epsilon)\, {}_2F_1(\epsilon, -1+2\epsilon; 2-\epsilon; \omega)}{\Gamma(2-\epsilon)}\,, \\ M_6^B &= -\frac{\pi^{4-2\epsilon} s^{-2\epsilon} \omega^{2\epsilon} \Gamma(1-\epsilon)\Gamma(-\epsilon)\Gamma(2\epsilon)\Gamma(1+\epsilon)\, {}_2F_1(2\epsilon, 1+\epsilon; 2-\epsilon; -\omega)}{\Gamma(2-\epsilon)}\,, \\ M_7^B &= -\frac{\pi^{4-2\epsilon} s^{-2\epsilon} \omega^{2\epsilon} \Gamma(1-\epsilon)\Gamma(-\epsilon)\Gamma(2\epsilon)\Gamma(1+\epsilon)\, {}_2F_1(2\epsilon, 1+\epsilon; 2-\epsilon; \omega)}{\Gamma(2-\epsilon)}\,, \\ M_8^B &= -\frac{\pi^{4-2\epsilon} s^{-2\epsilon} \Gamma(1-\epsilon)^4 \Gamma(\epsilon)^2}{\Gamma(2-2\epsilon)^2}\,. \end{aligned} \tag{5.70}$$

Being exact in ϵ, these expressions are allowed to appear as inhomogeneous terms in differential equations for the six remaining unknown master integrals.

We proceed to derive decoupled differential equations for the master integrals M_9 through M_{14} of the form in eq. (5.23), using the Laporta reduction algorithm in FIRE [137, 138]. Inserting the series ansatz eq. (5.29) for the two-loop forward master integrals, the differential equations then transform into difference equations. It turns out that three of

$B_2 =$ 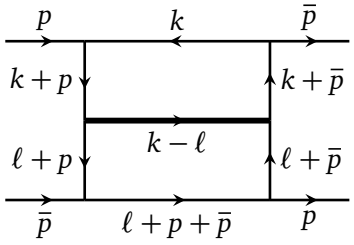

Figure 5.13: The forward two-loop crossed-box diagram B_2.

those equations can be solved exact in ϵ, producing series coefficients expressed as ratios of Gamma functions. As a result, the ansätze are easily recognized as series representations of hypergeometric functions:

$$\begin{aligned}
M_9 &= \frac{\pi^{4-2\epsilon} s^{-2\epsilon} \omega^{2\epsilon} \Gamma(1-\epsilon)^2 \Gamma(\epsilon) \Gamma(2\epsilon)\, {}_3F_2(1,1,2\epsilon;2,2-\epsilon;\omega)}{\Gamma(2-\epsilon)} \\
&\quad + \frac{\pi^{4-2\epsilon} s^{-2\epsilon} \omega^{\epsilon} \Gamma(1-\epsilon)^2 \Gamma(-1+\epsilon) \Gamma(\epsilon)\, {}_3F_2(1,1-\epsilon,\epsilon;2-2\epsilon,2-\epsilon;\omega)}{\Gamma(2-2\epsilon)} , \\
M_{12} &= -\frac{\pi^{4-2\epsilon} s^{-1-2\epsilon} \omega^{2\epsilon} (1-3\epsilon+2\epsilon^2) \Gamma(1-\epsilon)^2 \Gamma(\epsilon) \Gamma(-1+2\epsilon) \left({}_3F_2(1,1,2\epsilon;2,1-\epsilon;\omega) - 1 \right)}{\Gamma(2-\epsilon)} \\
&\quad + \frac{\pi^{4-2\epsilon} s^{-1-2\epsilon} \omega^{\epsilon} \Gamma(1-\epsilon)^2 \Gamma(-1+\epsilon) \Gamma(\epsilon)\, {}_3F_2(1,1-\epsilon,\epsilon;1-2\epsilon,2-\epsilon;\omega)}{\Gamma(1-2\epsilon)} , \\
M_{13} &= \frac{\pi^{4-2\epsilon} s^{-1-2\epsilon} \omega^{1+2\epsilon} \Gamma(-\epsilon)^2 \Gamma(2+\epsilon) \Gamma(1+2\epsilon)\, {}_4F_3(1,1,2+\epsilon,1+2\epsilon;2,2,2-\epsilon;\omega)}{\Gamma(2-\epsilon)} .
\end{aligned} \tag{5.71}$$

These expressions are useful because the corresponding integrals may appear as inhomogeneous terms in differential equations for the remaining unknown integrals: M_{10}, M_{11} and M_{14}.

In the remainder we focus on the computation of M_{14}, which is the forward crossed-box diagram. Inspecting the first-order differential equation for this integral reveals that it is coupled to all other master integrals, in particular to the unknown integrals M_{10} and M_{11}. After decoupling those two, as described in section 5.3.5, we obtain a third-order differential equation for M_{14}. As before we insert the series ansatz eq. (5.29) for the forward integral, which produces an eighth-order difference equation. The latter can be solved order-by-order in ϵ in terms of harmonic numbers (see eq. (5.28)). If the full diagram $B_2 = (\mathscr{C}(\epsilon) Q^{2\epsilon})^2 s^3 M_{14}$ is written as

$$B_2 = \sum_{n=1}^{\infty} c_n \, \omega^n + \sum_{n=1}^{\infty} d_n \, \omega^{n-\epsilon} + \sum_{n=1}^{\infty} e_n \, \omega^{n-2\epsilon} , \tag{5.72}$$

then its series coefficients are found to be

$$
\begin{aligned}
c_n = &\frac{-2S_{1,1}-4S_{-2}-2S_2}{\epsilon^2} + \frac{-16S_{-2,1}-8S_{1,-2}+4S_{1,2}+4S_{2,1}-18S_{1,1,1}+20S_{-3}+6S_3}{\epsilon} \\
&+ 80S_{-3,1}+40S_{-2,2}+40S_{1,-3}-8S_{1,3}+8S_{2,-2}-14S_{2,2}-6S_{3,1}-64S_{-2,1,1}-56S_{-4} \\
&- 32S_{1,-2,1}-16S_{1,1,-2}+52S_{1,1,2}+52S_{1,2,1}+48S_{2,1,1}-110S_{1,1,1,1}-14S_4-8\zeta_2 S_{1,1} \\
&- 16\zeta_2 S_{-2}-8\zeta_2 S_2+\mathcal{O}(\epsilon)\,, \\
d_n = &-\frac{2S_1}{\epsilon^3}+\frac{8S_2-10S_{1,1}}{\epsilon^2}+\frac{22S_{1,2}+20S_{2,1}-38S_{1,1,1}-6S_3-2\zeta_2 S_1}{\epsilon}-18S_{1,3}-28S_{2,2} \\
&- 14S_{3,1}+62S_{1,1,2}+58S_{1,2,1}+60S_{2,1,1}-130S_{1,1,1,1}+8S_4-10\zeta_2 S_{1,1}+8\zeta_2 S_2 \\
&- 4\zeta_3 S_1+\mathcal{O}(\epsilon)\,, \\
e_n = &-\frac{1}{\epsilon^4}-\frac{2S_1}{\epsilon^3}-\frac{4S_{1,1}+2S_2}{\epsilon^2}-\frac{4S_{1,2}+2S_{2,1}+8S_{1,1,1}+2S_3}{\epsilon}-4S_{1,3}-2S_{2,2}-2S_{3,1} \\
&- 8S_{1,1,2}-4S_{1,2,1}-2S_{2,1,1}-16S_{1,1,1,1}-2S_4+\mathcal{O}(\epsilon)\,,
\end{aligned}
\tag{5.73}
$$

where $S_{\vec{\ell}} \equiv S_{\vec{\ell}}(n-1)$. The validity of the representation eq. (5.72) for the forward crossed-box diagram has been checked by reconstructing the full diagram, from the infinite sums, in terms of harmonic polylogarithms and performing a numerical cross-check using SecDec [139–141]. These series coefficients now form the starting point for the next phase, which is to extract the Mellin moments of the corresponding physical s-channel cut diagram.

Inspecting the analytical structure of B_2 from its representation in terms of harmonic polylogarithms reveals three branch cuts. They are located along the real axis in the domains $\omega \in (-\infty, 0]$, $\omega \in (-\infty, -1]$ and $\omega \in [1, \infty)$, which correspond to massless u-channel cuts, massive u-channel cuts and the massive s-channel cut, respectively. The first and second types of branch cuts in the forward diagram are unphysical; they will be removed by performing the shifting procedure and applying replacement rules, respectively. Let us start with the shifting procedure. As we have seen in previous examples, this amount to the transformation

$$
B_2 \longrightarrow \widetilde{B}_2 = \sum_{n=1}^{\infty} (c_n + d_{n+\epsilon} + e_{n+2\epsilon})\,\omega^n \equiv \sum_{n=1}^{\infty} \widetilde{c}_n\,\omega^n\,. \tag{5.74}
$$

More explicitly, the newly defined coefficients $\widetilde{c}_n$ are given by

$$
\begin{aligned}
\widetilde{c}_n = &-\frac{1}{\epsilon^4}-\frac{4S_1}{\epsilon^3}+\frac{10S_2-16S_{1,1}-4S_{-2}-6\zeta_2}{\epsilon^2}+\frac{-20S_3+40S_{1,2}+40S_{2,1}-64S_{1,1,1}}{\epsilon} \\
&+\frac{20S_{-3}-16S_{-2,1}-8S_{1,-2}-20\zeta_2 S_1}{\epsilon}+40S_4-100S_{2,2}-80S_{3,1}+160S_{1,1,2} \\
&+160S_{1,2,1}+160S_{2,1,1}-256S_{1,1,1,1}-56S_{-4}+80S_{-3,1}+40S_{1,-3}-84S_{1,3} \\
&+40S_{-2,2}+8S_{2,-2}-64S_{-2,1,1}-32S_{1,-2,1}-16S_{1,1,-2}-16\zeta_2 S_{-2}+44\zeta_2 S_2 \\
&-72\zeta_2 S_{1,1}-4\zeta_3 S_1-55\zeta_4+\mathcal{O}(\epsilon)\,.
\end{aligned}
\tag{5.75}
$$

where again $S_{\vec{\ell}} \equiv S_{\vec{\ell}}(n-1)$. In order to arrive at this form for the series coefficients $\widetilde{c}_n$, we

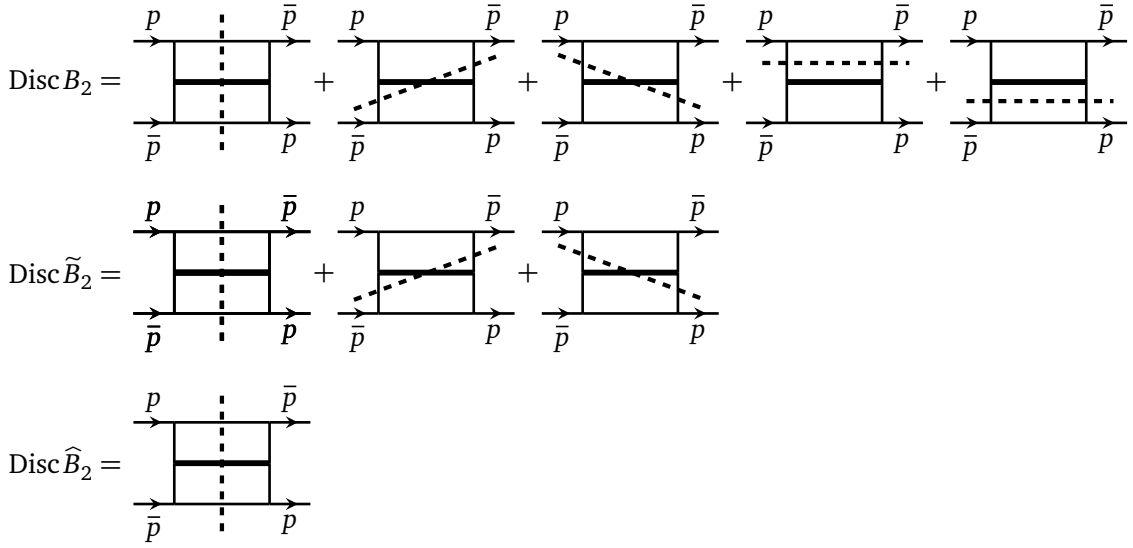

Figure 5.14: Cutting equation for the forward diagram B_2 (top line), for the modified forward diagram $\widetilde{B}_2$ which does not contain the unphysical branch cut along $\omega \in (-\infty, 0]$ (middle line), and for $\widehat{B}_2$ which does not contain the other unphysical branch cut along $\omega \in (-\infty, -1]$ either (bottom line). The series coefficient of $\widehat{B}_2$ are equal to the Mellin moments of the physical cut.

have made use of the package HARMONICSUMS to expand the harmonic numbers $S_{\vec{\ell}}(n+k\epsilon)$, which appear in the coefficients $d_{n+\epsilon}$ and $e_{n+2\epsilon}$ as a result of shifting, as a Taylor series in ϵ. From the formula in eq. (5.74) it is clear that $\widetilde{B}_2$ is regular at the origin, so we have successfully removed the branch cut along $\omega \in (-\infty, 0]$ from the forward diagram. Crucially, the discontinuities around the remaining two branch cuts are unchanged. This can be verified by explicitly computing and comparing the discontinuity of both B_2 and $\widetilde{B}_2$ using the HPL package [115, 116].[1] In terms of cutting equations, this elimination of unphysical branch cut in the forward diagram is to be interpreted as the elimination of cut diagrams on the right-hand side of the cutting equation, as indicated by the first two lines in fig. 5.14.

In the next stage we modify the forward diagram even further, in such a way that the second unphysical branch cut is removed as well. At the level of individual harmonic polylogarithms this task is performed simply along the lines of example 5.5. The results translate to replacement rules for the harmonic numbers. In particular, harmonic numbers with only positive indices do not need to be altered: the corresponding "resummed functions" do not contain unphysical branch cuts. The first two orders in ϵ of $\widetilde{c}_n$ therefore do not need to be modified. For the remaining harmonic numbers we apply the following replacement rules. We recall that these rules are derived in a diagram-independent way. At order ϵ^{-2} we need a single replacement rule:

$$S_{-2} \to -\tfrac{1}{2}\zeta_2 \,. \tag{5.76}$$

[1] Specifically, using the function `HPLAnalyticContinuation` in that package.

Replacement rules at order ϵ^{-1} are:

$$S_{-3} \to -\tfrac{3}{4}\zeta_3\,,\quad S_{-2,1} \to -\tfrac{5}{8}\zeta_3\,,\quad S_{1,-2} \to -\tfrac{1}{8}\zeta_3 - \tfrac{1}{2}\zeta_2 S_1\,. \tag{5.77}$$

And finally, replacement rules at order ϵ^0 are given by:

$$\begin{aligned}
S_{-4} &\to -\tfrac{7}{8}\zeta_4\,,\\
S_{-3,1} &\to -\tfrac{11}{4}\zeta_4 - \tfrac{1}{2}\zeta_2\log^2 2 + \tfrac{7}{4}\zeta_3\log 2 + 2\mathrm{Li}_4\left(\tfrac{1}{2}\right) + \tfrac{1}{12}\log^4 2\,,\\
S_{1,-3} &\to +\tfrac{15}{8}\zeta_4 + \tfrac{1}{2}\zeta_2\log^2 2 - \tfrac{7}{4}\zeta_3\log 2 - 2\mathrm{Li}_4\left(\tfrac{1}{2}\right) - \tfrac{1}{12}\log^4 2 - \tfrac{3}{4}\zeta_3 S_1\,,\\
S_{-2,2} &\to +\tfrac{51}{16}\zeta_4 + \zeta_2\log^2 2 - \tfrac{7}{2}\zeta_3\log 2 - 4\mathrm{Li}_4\left(\tfrac{1}{2}\right) - \tfrac{1}{6}\log^4 2\,,\\
S_{2,-2} &\to -\tfrac{65}{16}\zeta_4 - \zeta_2\log^2 2 + \tfrac{7}{2}\zeta_3\log 2 + 4\mathrm{Li}_4\left(\tfrac{1}{2}\right) + \tfrac{1}{6}\log^4 2 - \tfrac{1}{2}\zeta_2 S_2\,,\\
S_{-2,1,1} &\to +\tfrac{5}{16}\zeta_4 + \tfrac{1}{4}\zeta_2\log^2 2 - \tfrac{7}{8}\zeta_3\log 2 - \mathrm{Li}_4\left(\tfrac{1}{2}\right) - \tfrac{1}{24}\log^4 2\,,\\
S_{1,-2,1} &\to -\tfrac{3}{16}\zeta_4 - \tfrac{5}{8}\zeta_3 S_1\,,\\
S_{1,1,-2} &\to -\tfrac{13}{8}\zeta_4 - \tfrac{1}{4}\zeta_2\log^2 2 + \tfrac{7}{8}\zeta_3\log 2 + \mathrm{Li}_4\left(\tfrac{1}{2}\right) + \tfrac{1}{24}\log^4 2 - \tfrac{1}{8}\zeta_3 S_1 - \tfrac{1}{2}\zeta_2 S_{1,1}\,.
\end{aligned} \tag{5.78}$$

After making these replacements the series coefficients $\widetilde{c}_n$ become $\widehat{c}_n$, given by

$$\begin{aligned}
\widehat{c}_n = &-\frac{1}{\epsilon^4} - \frac{4S_1}{\epsilon^3} + \frac{10S_2 - 16S_{1,1} - 4\zeta_2}{\epsilon^2}\\
&+ \frac{-20S_3 + 40S_{1,2} + 40S_{2,1} - 64S_{1,1,1} - 16\zeta_2 S_1 - 4\zeta_3}{\epsilon}\\
&+ 40S_4 - 84S_{1,3} - 100S_{2,2} - 80S_{3,1} + 160S_{1,1,2} + 160S_{1,2,1}\\
&+ 160S_{2,1,1} - 256S_{1,1,1,1} + 40\zeta_2 S_2 - 64\zeta_2 S_{1,1} - 12\zeta_3 S_1 - 24\zeta_4 + \mathcal{O}(\epsilon)\,.
\end{aligned} \tag{5.79}$$

These coefficients $\widehat{c}_n$ constitute the main result of this example section. We have checked explicitly that resumming these coefficients yields an expression

$$\widehat{B}_2 = \sum_{n=1}^{\infty} \widehat{c}_n \omega^n\,, \tag{5.80}$$

which only has a branch cut along $\omega \in [1, \infty)$ and whose discontinuity along that branch cut is the same as for the original diagram B_2. This means that these series coefficients $\widehat{c}_n$ in eq. (5.79) must be equal to the Mellin moments of the sum of physical cuts of the forward diagram B_2, that is,

$$\frac{1}{2\pi i}\mathscr{M}_n\Big[\mathrm{Cut}_{\mathrm{phys}}\, B_2\Big] = \widehat{c}_n\,. \tag{5.81}$$

The validity of the above statement can be verified by comparing the coefficients $\widehat{c}_n$ against an explicit computation of the Mellin moments of the physical cut of the forward diagram B_2, depicted on the third line in fig. 5.14. An explicit result for this particular cut diagram was given in eq. (B.21) of ref. [22]. Correcting for small misprints (see appendix A of

ref. [142]) and adopting our normalisation convention, we have that

$$\begin{aligned}\mathrm{Cut}_{\mathrm{phys}}\, B_2 = &-2\pi i\, \mathcal{N}(\epsilon) z^{2\epsilon}(1-z)^{-1-4\epsilon}\bigg(-\frac{4}{\epsilon^3}+\frac{16}{\epsilon^2}+\frac{z(z-8)-89}{6\epsilon}\\ &+\tfrac{1}{9}(z-1)(1+2z)+\tfrac{2}{27}(z-1)(13z-16)\epsilon+\mathcal{O}(\epsilon^2)\bigg)\\ &-2\pi i\, \mathcal{N}(\epsilon) z^{2\epsilon}(1-z)^{-1-2\epsilon}\bigg(-\frac{2\log z}{\epsilon^2}+\frac{1}{\epsilon}\Big[2\log^2 z\\ &+\log z\left(4\log(1-z)+8\right)+\tfrac{1}{6}(1-z)(z-7)\Big]-\tfrac{4}{3}\log^3 z\\ &-\log^2 z\left(8+2\log(1-z)\right)+36\big(\mathrm{Li}_3(z)-\zeta_3\big)+\tfrac{1}{9}(z-2z^2+1)\\ &-\log z\left(20\zeta_2+16\,\mathrm{Li}_2(z)+16\log(1-z)+4\log^2(1-z)+8\right)\\ &+\tfrac{1}{3}(z-1)(z-7)\log(1-z)+\mathcal{O}(\epsilon)\bigg)\,. \end{aligned} \tag{5.82}$$

where $\mathcal{N}(\epsilon)=\frac{\Gamma(1-2\epsilon)^4}{\Gamma(1-4\epsilon)\Gamma(2-2\epsilon)^2\Gamma(1-\epsilon)^2\Gamma(1+\epsilon)^2}$.

After expanding the factors $(1-z)^{-1-k\epsilon}$ in terms of plus-distributions and taking the Mellin transform of this equation, we find perfect agreement with our formula in eq. (5.81), which expresses the Mellin moments in terms of series coefficients of the (modified) forward diagram.

5.5. Conclusions

In this chapter I have presented a method for computing Mellin moments of single-particle inclusive cross sections, such as Drell-Yan and Higgs production, directly from forward scattering amplitudes by invoking unitarity in the form of cutting equations. Due to the non-inclusive nature of these processes, the cutting equations contain unphysical cuts. This problem is solved by our prescription for removing such unphysical cut contributions to the discontinuity of a forward diagram, once expressed in the reciprocal $\omega = 1/z$ variable. The removal occurs through a complex shift in the summation index n, and through a replacement rule dictionary for harmonic sums in the results. The resulting modified series coefficients reproduce precisely the Mellin moments of the corresponding physical contribution to the Drell-Yan cross section.

The method thus provides a new means to compute semi-inclusive single-scale cross sections, which has been demonstrated on various one- and two-loop forward amplitudes. Since the main ingredients to the method are forward loop diagrams, as opposed to cut diagrams, it is particularly useful as an alternative means of computing real radiation corrections. Being exclusively expressed in terms of virtual diagrams, numerical cross-checks may be performed in a uniform way for all contributions to a scattering cross section.

Extending the method in this chapter to three-loop amplitudes requires a renewed analysis of unphysical branch cuts and of the assumption that the solution space is spanned by harmonic sums. After such preparatory work, progress can hopefully be made towards exact results for single-scale cross sections at N^3LO accuracy. In closing, this chapter has demonstrated once again the applicability of unitarity to practical computations of scattering cross section and the developed unitarity method should serve as a tool for future calculations.

Chapter 6

Conclusions

In this thesis I have presented new tools for the computation of scattering amplitudes. These tools have one common feature: the presence of on-shell intermediate particles. The act of constraining intermediate particles to their mass shell reduces the complexity of scattering amplitudes, a simplification that derives from the theory of unitarity. In chapter 2 I have reviewed the notion of unitarity in quantum field theory, along with the closely related concepts of cutting equations for Feynman diagrams and the optical theorem. Making optimal use of unitarity in practice, however, is not necessarily straightforward and therefore requires the development of additional techniques. These conclusions collect the main results that were obtained in chapters 3 to 5.

The first new tool described in this thesis is the computer program MadSpin for decaying unstable particles that have a small width-to-mass ratio, such as the top quark and the Higgs and electroweak vector bosons. As explained in chapter 3, MadSpin produces intermediate particles strictly on-shell and subsequently generates their decay products in a sophisticated manner that is designed to include an accurate description of spin correlations. For its implementation we have developed a method to estimate the maximum weight of particle scattering events numerically, which is an important step in the automation of the algorithm.

Making use of the MadSpin program, we have performed an extensive analysis of the validity of the method and its implementation. The analysis shows that the inherent narrow-width approximation is valid for many different processes. It also reveals two delicate quantities, namely the differential cross section with respect to the invariant mass of the decay products of an unstable particle, or with respect to the center-of-mass energy. In the former case, the results will be unreliable in regions far away from the resonance, where the validity of the narrow-width approximation tends to break down. In the latter case, the differential distribution incorrectly vanishes below the threshold for on-shell production of the intermediate state particles when there exist other production mechanisms with lighter intermediate particles, for example γ^* instead of Z. Apart from these isolated circumstances, MadSpin is a widely applicable tool.

Crucially, we have demonstrated that MadSpin is capable of taking spin-correlation effects into account, a key feature of the program. We obtained differential cross sections for $t\bar{t}$ production with respect to spin-correlation sensitive observables and found excellent agreement with the results of MCFM. After extending the aforementioned analysis to the process of $t\bar{t}H$ production, we illustrated how spin correlations are instrumental to the study of properties of elementary particles, such as the parity of the Higgs boson.

In chapter 4 we have extended the 'unitarity toolbox' by introducing a cutting prescription for eikonal Feynman diagrams in their position-space representation. The resulting cutting equation, given in eq. (4.42), provides a physical interpretation of the imaginary part of eikonal diagrams as the consequence of lightlike soft gluon exchanges between causally connected hard particles. We have contrasted this interpretation with the more familiar momentum-space picture, in which the imaginary part arises from transverse gluon exchanges between on-shell asymptotic states. Furthermore, we have elucidated a connection between the imaginary part of the cusp anomalous dimension and the non-relativistic Coulomb potential.

In several examples we have worked out the explicit evaluation of cut diagrams in position space and verified the validity of our cutting equation. The first example, the non-planar two-loop ladder diagram, illustrates how the principal value integrals in multi-loop cut diagrams can be computed in practice in terms of multiple polylogarithms. We have shown explicitly that the polylogarithmic function, produced by the sum of cut diagrams, equals the imaginary part of the original two-loop diagram with timelike external kinematics.

The second example, a three-loop ladder diagram, confirms that the cutting equation involves multiple cut contributions, in this case a cut diagram with all three exchanged gluons simultaneously on-shell. The relative simplicity of the three-loop cut diagrams in position space, with respect to the analogous phase-space cuts in momentum space, is perhaps the best illustration of the computational advantage of our cutting prescription.

In the third example, a two-loop web diagram, we have reconciled the apparent discrepancy between the limitation of the cutting equation to the leading order in the dimensional regularization parameter ϵ, on the one hand, and the cancellation of the leading divergences in ϵ within web diagrams on the other hand. The resulting prescription is to perform first the cancellation of poles in ϵ among the constituents of the web and to apply subsequently the cutting equation in order to obtain the imaginary part of the web.

Finally, we have provided evidence that the position-space cutting equation is equally valid for more complicated classes of eikonal diagrams involving internal gluon vertices. In the example of a three-gluon vertex connected to three Wilson lines, we have computed the cut diagrams semi-analytical and obtained perfect numerical agreement with the imaginary part of the original diagram. Based on these promising results, we anticipate an important role for the position-space cutting rules in the development of generalized unitarity methods for eikonal Feynman diagrams, which allow to reconstruct complete scattering amplitudes in the limit of soft gluon radiation.

Turning to more traditional applications of unitarity, one can calculate total cross sections for fully inclusive processes, such as deep inelastic scattering, from forward amplitudes using the optical theorem. In a similar spirit, non-inclusive processes may be studied by invoking cutting equations rather than the optical theorem. In chapter 5 we have taken a first step in this direction by showing how the Drell-Yan cross section can be obtained from forward loop amplitudes.

Due to the non-inclusive nature of the Drell-Yan process, the cutting equation is insufficient to derive an expression for the cross section. To resolve this problem, we have formulated two prescriptions for removing unphysical cut contributions to the discontinuity of the forward Drell-Yan amplitude. Both prescriptions apply to the series coefficients c_n in the series expansion of forward loop integrals in ω, the ratio of the center-of-mass energy and the invariant mass of the final state lepton pair. The first prescription shifts the Mellin moments n in the series such that the powers of ω become integer, which has the effect of eliminating the unphysical cuts with a branch point at $\omega = 0$. The second prescription replaces the alternating harmonic sums in the series coefficients by their asymptotic expansion at infinity and thereby removes the last unphysical branch cut. As a result, the modified series coefficients yield exactly the Mellin moments of the cross section.

We have applied our method to two-loop forward diagrams which correspond to the Drell-Yan cross section at next-to-next-to-leading order in QCD. The two examples provided, a self-energy diagram and a crossed-box diagram, demonstrate that our prescriptions are indeed capable of removing all types of unphysical branch cut from the forward diagram. For these calculations we have also developed the necessary tools for computing the series coefficients of forward loop integrals, which form the input for the two prescriptions.

The great benefit of this method is that it requires only the computation of forward loop integrals and thereby avoids the (challenging) computation of phase-space integrals. It is also worth emphasizing that the method is not limited to the Drell-Yan process, but immediately extends to any single-particle exclusive one-scale process, including Higgs boson production in the large top quark mass limit.

In conclusion, we have witnessed that unitarity is a powerful concept in the computation of scattering amplitudes. We have also seen that the actual fruitful application of unitarity may call for the development of new tools and techniques. The tools that have been developed in this thesis extend the range of applicability of unitarity and are, I believe, valuable for ongoing and future research in the field of scattering amplitudes.

APPENDIX A

MULTIPLE POLYLOGARITHMS

A.1. Definitions and properties

Definition A.1. *Multiple Polylogarithms (MPLs) are defined recursively by*

$$G(a_1,\ldots,a_n;x)=\int_0^x \frac{\mathrm{d}t}{t-a_1}G(a_2,\ldots,a_n;t) \qquad \text{for} \quad (a_1,\ldots,a_n)\neq\vec{0}_n\,, \tag{A.1}$$

starting from

$$G(;0)\equiv 0\,, \qquad G(;x)\equiv 1\,, \qquad G(\vec{0}_n;x)\equiv\frac{1}{n!}\log^n x\,, \tag{A.2}$$

where $\vec{a}_n=(a,\ldots,a)$ denotes a vector with n equal indices. The transcendental weight of an MPL is given by the number of indices n (i.e. the number of integrations).

Multiple polylogarithms satisfy a variety of properties. They form a shuffle algebra, with the shuffle product

$$G(a_1,\ldots,a_{n_1};x)\,G(a_{n_1+1},\ldots,a_{n_1+n_2};x)=\sum_{\sigma\in\Sigma(n_1,n_2)}G(a_{\sigma(1)},\ldots,a_{\sigma(n_1+n_2)};x)\,. \tag{A.3}$$

They are invariant under a common rescaling of all arguments,

$$G(k\,\vec{a};k\,x)=G(\vec{a};x) \qquad \text{for} \quad a_i\neq 0 \quad \text{and} \quad k\in\mathbb{C}^*\,. \tag{A.4}$$

where $\vec{a}=(a_1,\ldots,a_n)$. They reduce to classical polylogarithms in certain cases,

$$\begin{aligned} G(\vec{0}_n;x)&=\frac{1}{n!}\log^n x\,, & G(\vec{0}_{n-1},a;x)&=-\mathrm{Li}_n\left(\frac{x}{a}\right)\,,\\ G(\vec{a}_n;x)&=\frac{1}{n!}\log^n\left(1-\frac{x}{a}\right)\,, & G(\vec{0}_n,\vec{a}_p;x)&=(-1)^p\,S_{n,p}\left(\frac{x}{a}\right)\,, \end{aligned} \tag{A.5}$$

or to harmonic polylogarithms (see ref. [143]),

$$G(\vec{a};x) = (-1)^k H_{\vec{a}}(x) \qquad \text{if} \quad \forall a_i \in \vec{a}\colon \;\; a_i \in \{\pm 1, 0\}\,, \tag{A.6}$$

where k denotes the number of $+1$'s in $\vec{a}$. More details on MPLs may be found in ref. [112].

A slightly different notation for MPLs, in which the base point of integration may be freely chosen, can be more convenient sometimes.

Definition A.2. *Multiple polylogarithms with free base point of integration are defined by*

$$I(a_0; a_1, \ldots, a_n; a_{n+1}) = \int_{a_0}^{a_{n+1}} \frac{\mathrm{d}t}{t - a_n} I(a_0; a_1, \ldots, a_{n-1}; t) \quad \text{with} \quad I(a_0; \,; a_{n+1}) \equiv 1\,. \tag{A.7}$$

Setting the base point a_0 to zero we obviously recover the multiple polylogarithms defined in eq. (A.1), up to a conventional reversal of the order of the indices.

A.2. Real and imaginary parts of multiple polylogarithms

Multiple polylogarithms generally have a real and an imaginary part. The real part of an MPL can be obtained by subtracting the imaginary part from the original function,

$$\operatorname{Re} G(\vec{a};x) = G(\vec{a};x) - i \operatorname{Im} G(\vec{a};x)\,. \tag{A.8}$$

The imaginary part of a multiple polylogarithms, in turn, can be written recursively in terms of lower weight functions. A simple example is given by a power of logarithms,

$$\operatorname{Im} G(\vec{0}_n; x \pm i\eta) = \frac{1}{n!} \operatorname{Im} \log^n(x \pm i\eta) = \frac{1}{n!} \operatorname{Im} \Big[\big(\log|x| \pm i\pi\theta(-x) \big)^n \Big]\,. \tag{A.9}$$

In the case of more general indices $\vec{a}$, the corresponding relation is more involved. Below, we list results for the imaginary part of multiple polylogarithms up to weight 4, in terms of (real and imaginary parts of) lower weight functions.

First we introduce generalized step functions $\theta(a_1, \ldots, a_n)$, which may be thought of as enforcing $a_1 \leq \cdots \leq a_n$.

Definition A.3. *The generalized step function $\theta(a_1, \ldots, a_n)$ is defined in terms of ordinary single-variable step functions,*

$$\theta(a_1, \ldots, a_n) \equiv \prod_{i=1}^{n-1} \theta(a_{i+1} - a_i) \quad \textit{for } n > 1 \quad \text{and} \quad \forall\, i\colon \;\; a_i \neq a_{i+1} \;\textit{and}\; a_i \in \mathbb{R}\,. \tag{A.10}$$

Equal adjacent arguments are dealt with using the following definition

$$\theta(\dots,a,\underbrace{b,\dots,b}_{n\,\text{times}},c,\dots)=\frac{1}{n!}\theta(\dots,a,b,c,\dots)\qquad \text{for real indices } a\neq b\neq c\,. \tag{A.11}$$

Infinitesimal imaginary parts produce an overall sign,

$$\theta(\dots,a\pm i\eta,\dots)=\pm\theta(\dots,a,\dots)\quad \text{for}\quad a\in\mathbb{R}\,. \tag{A.12}$$

In this notation, the imaginary part of multiple polylogarithms up to weight four are

$$\operatorname{Im}G(a;x)=\pi\,\theta(0,a,x)\,, \tag{A.13}$$

$$\operatorname{Im}G(a,b;x)=\pi\,\theta(0,a,x)\operatorname{Re}G(b;a)+\pi\,\theta(0,b,x)\operatorname{Re}I(b;a;x)\,, \tag{A.14}$$

$$\begin{aligned}\operatorname{Im}G(a,b,c;x)=\;&\pi\,\theta(0,a,x)\operatorname{Re}G(b,c;a)+\pi\,\theta(0,b,x)\operatorname{Re}\big[I(b;a;x)G(c;b)\big]\\&+\pi\,\theta(0,c,x)\operatorname{Re}I(c;b,a;x)+2\pi^3\theta(0,c,b,a,x)\,,\end{aligned} \tag{A.15}$$

$$\begin{aligned}\operatorname{Im}G(a,b,c,d;x)=\;&\pi\,\theta(0,a,x)\operatorname{Re}G(b,c,d;a)\\&+\pi\,\theta(0,b,x)\operatorname{Re}\big[I(b;a;x)G(c,d;b)\big]\\&+\pi\,\theta(0,c,x)\operatorname{Re}\big[I(c;b,a;x)G(d;c)\big]\\&+\pi\,\theta(0,d,x)\operatorname{Re}I(d;c,b,a;x)\\&+2\pi^3\theta(0,c,b,a,x)\operatorname{Re}G(d;c)\\&+2\pi^3\theta(0,d,b,a,x)\operatorname{Re}I(d;c;b)\\&+2\pi^3\theta(0,d,c,a,x)\operatorname{Re}I(c;b;a)\\&+2\pi^3\theta(0,d,c,b,x)\operatorname{Re}I(b;a;x)\,,\end{aligned} \tag{A.16}$$

where $a,b,c,d,x\in\mathbb{R}$, x is positive, and in each case the last index must be non-zero. The suppressed Feynman $i\eta$'s may be reinstated by replacing the indices with $a\to a\pm i\eta$. A proof of these formulas can be found in ref. [4].

A.3. Multiple polylogarithms in canonical form

In this section we describe an algorithm to cast multiple polylogarithms in canonical form, which is extensively used in the computations in section 4.4. In order to describe the algorithm, we start by setting up our notation. We denote by $g(\vec{x})$ some function which is not in canonical form, but is given by a linear combination of MPLs of the form $G(\vec{a}(\vec{x});z(\vec{x}))$, depending on $\vec{x}$ through both the indices and the argument. To simplify the following presentation, we will assume that $g(\vec{x})$ has uniform transcendental weight w. Then, the following algorithm writes $g(\vec{x})$ in canonical form.

Algorithm A.4 (Multiple polylogarithms in canonical form)**.**

1. *Compute the symbol $S[g(\vec{x})]$ of the function $g(\vec{x})$.*

2. *Apply a map $M_{\vec{x}}$ to the symbol $S[g(\vec{x})]$, whose purpose is to construct a polylogarithm in canonical form with the same symbol as the original function. The resulting expression differs only from the original function by terms proportional to transcendental constants (which are in the kernel of the symbol map).*

3. *Compute subsequently the coproducts $\Delta_{2,1,\ldots,1}$, $\Delta_{3,1,\ldots,1}$, $\ldots$, $\Delta_{w-1,1}$ to reconstruct any missing terms proportional to constants with transcendental weight $2,3,\ldots,w-1$ respectively.*

The output of this algorithm is a new function $h(\vec{x})$ in canonical form, which is numerically equal to the original function $g(\vec{x})$. In the remainder of this section contains the definitions of the symbol S, the map $M_{\vec{x}}$ and the coproduct Δ.

The first step of the algorithm involves computing the symbol of multiple polylogarithms, first introduced in ref. [144]. Analogous to the total differential,

$$\mathrm{d}G(a_{n-1},\ldots,a_1;a_n) = \sum_{i=1}^{n-1} G(a_{n-1},\ldots,a_{i+1},a_{i-1},\ldots,a_1;a_n)\,\mathrm{d}\log\left(\frac{a_i-a_{i+1}}{a_i-a_{i-1}}\right), \tag{A.17}$$

the symbol of a multiple polylogarithm is defined as follows (see ref. [110]).

$$S\big[G(a_{n-1},\ldots,a_1;a_n)\big] = \sum_{i=1}^{n-1} S\big[G(a_{n-1},\ldots,a_{i+1},a_{i-1},\ldots,a_1;a_n)\big]\otimes\left(\frac{a_i-a_{i+1}}{a_i-a_{i-1}}\right), \tag{A.18}$$

in the case where the indices a_i are generic; i.e., non-zero and mutually different. The formula for the symbol in eq. (A.18), augmented with formulas for special cases and the rules of symbol calculus (see refs. [112, 113]), allows the symbol $S[g(\vec{x})]$ to be computed.

The second step of the algorithm takes the resulting symbol as input and maps it to an expression of multiple polylogarithms in canonical form, whose symbol is the same as the symbol of the original function. A procedure that achieves this goal was given in appendix D of ref. [114]. The exposition below presents their procedure in the form of an explicit map and provides a slight generalisation in order to deal with functions of more than two variables that have a sufficiently factorized form.

Definition A.5. *The map $M_{\vec{x}}$ is defined recursively in the number of variables. Starting with the case of a single variable, we define the map M_x which takes tensors to functions,*

$$M_x(T) = \begin{cases} G\left(-\frac{b_1}{a_1},\ldots,-\frac{b_w}{a_w};x\right) & \text{if } T=(a_w x+b_w)\otimes\cdots\otimes(a_1x+b_1)\,, \\ 0 & \text{otherwise}\,, \end{cases} \tag{A.19}$$

where a_i and b_i are independent of x.

The map M_x is linear in the space of tensors: given a symbol $S=\sum_i c_i T_i$, with rational numbers c_i and tensors T_i, one has $M_x(S)=\sum_i c_i M_x(T_i)$. The map $M_x(T)$ is designed to

construct a function in canonical form, such that its symbol is given by T plus possibly other tensors which have at least one entry independent of x. The proof of this statement was given in ref. [114].

Definition A.6. *Generalising to the multivariate case, we let $\vec{x} = \{x_1, \ldots, x_n\}$ denote a collection of at least two variables, and define the multivariate map*

$$\begin{aligned} M_{\vec{x}}(S) &= \left(P^{(w)}_{\vec{x},S} \circ P^{(w-1)}_{\vec{x},S} \circ \cdots \circ P^{(1)}_{\vec{x},S} \circ M^{(0)}_{\vec{x}}\right)(S) \\ &\equiv P^{(w)}_{\vec{x},S}\left(P^{(w-1)}_{\vec{x},S}\left(\cdots P^{(1)}_{\vec{x},S}\left(M^{(0)}_{\vec{x}}(S)\right)\cdots\right)\right), \end{aligned} \tag{A.20}$$

where the projectors P map functions to functions according to

$$P^{(r)}_{\vec{x},S}(h) = h + M^{(r)}_{\vec{x}}(S - S[h])\,. \tag{A.21}$$

The maps $M^{(r)}_{\vec{x}}(S)$ which occur on the right-hand sides of eqs. (A.20) and (A.21) are linear in the space of tensors (as in the case of a single variable) and are defined to act on elementary tensors T by recursion in the number of variables,

$$M^{(r)}_{\vec{x}}(T) = \begin{cases} M_{x_1}(T) & \text{for } r = 0\,, \\ M_{x_2,\ldots,x_n}(T^{(1)} \otimes \cdots \otimes T^{(r)})\, M_{x_1}(T^{(r+1)} \otimes \cdots \otimes T^{(w)}) & \text{for } r = 1, 2, \ldots, w-1\,, \\ M_{x_2,\ldots,x_n}(T) & \text{for } r = w\,. \end{cases} \tag{A.22}$$

For the map $M^{(r)}_{\vec{x}}(T)$ to be non-vanishing, the last $w - r$ indices must depend on x_1. Its output is then given by a canonical function with argument x_1 and weight $w-r$, multiplied by an x_1-independent function of weight r. The projectors $P^{(r)}_{\vec{x},S}(h)$ add such functions to their input, thus gradually constructing a function in canonical form, starting with functions of x_1 with weight w down to weight 1 and repeating the process for the remaining variables $x_2, x_3, \ldots, x_n$. As a result, the multivariate map $M_{\vec{x}}(S)$ generates a function of the form

$$\sum_{(i_1,\ldots,i_n)} c_{i_1,\ldots,i_n} G(\vec{a}_{i_n}; x_n) \cdots G(\vec{a}_{i_1}; x_1)\,, \tag{A.23}$$

where the $\vec{a}_{i_k}$ are independent of $x_1, \ldots, x_k$. This expression is by definition in canonical form. For a single variable, the indices are in fact constants and as slight abuse of terminology this is what we occasionally refer to as canonical form, bearing in mind that eq. (A.23) is the proper definition of canonical form in the multivariate case.

As a result, the second step of the algorithm produces a function that differs from the original $g(\vec{x})$ only by terms proportional to transcendental constants, because such terms are in the kernel of the symbol map.

The third step in the algorithm requires the coproduct of multiple polylogarithms, which generalizes the concept of the symbol. Before describing how it may be used to construct

missing terms proportional to transcendental constants, let us first define the required coproducts of the form $\Delta_{p,q,\ldots,r}$. They are derived from the general coproduct Δ, which is defined by its action on iterated integrals with a freely specified base point of integration, see eq. (A.7).

Definition A.7. *The coproduct is defined by (see ref. [109])*

$$\Delta\big[I(a_0;a_1,\ldots,a_n;a_{n+1})\big] = \sum_{k=0}^{n} \sum_{0=i_0<i_1<\cdots<i_k<i_{k+1}=n+1} I(a_0;a_{i_1},\ldots,a_{i_k};a_{n+1}) \otimes \prod_{p=0}^{k} I(a_{i_p};a_{i_p+1},\ldots,a_{i_{p+1}-1};a_{i_{p+1}}). \quad \text{(A.24)}$$

The right-hand side of eq. (A.24) consists of tensors with two entries, each entry having a weight between 0 and n, such that the two weights add up to n, the weight of the original function[1]. All possible pairs of weights are thus $(0,n),(1,n-1),\ldots,(n,0)$. Grouping the tensors by those pairs of weights decomposes the coproduct into

$$\Delta = \sum_{p+q=n} \Delta_{p,q} \,. \quad \text{(A.25)}$$

In other words, the action of $\Delta_{p,q}$ on $I(a_0;a_1,\ldots,a_n;a_{n+1})$ yields the subset of terms in eq. (A.24) of tensors with weight (p,q). Besides the operator $\Delta_{p,q}$, the third step of our algorithm also uses operators with multiple indices $\Delta_{p,q,\ldots,r}$. Those are defined recursively in terms of $\Delta_{p,q}$. For example, $\Delta_{p,q,r}$ is defined by application of $\Delta_{q,r}$ to the second entry of all tensors obtained from $\Delta_{p,q+r}$. These are the definitions of the coproducts which are needed in the third step of the algorithm. For more details, see ref. [113].

The coproducts thus defined may be employed to construct missing terms proportional to transcendental constants, starting with the lowest-weight constants (see ref. [114]). To be specific, in the previous step of the algorithm we constructed a function $h(\vec{x})$ such that $S[g(\vec{x})-h(\vec{x})]=0$. This means that the difference $g(\vec{x})-h(\vec{x})$ must be proportional to transcendental constants. Following the recipe in the third step of the algorithm we act on this difference with the coproduct $\Delta_{2,1,\ldots,1}$ to first find terms proportional to ζ_2. The coproduct takes the form

$$\Delta_{2,1,\ldots,1}\big[g(\vec{x})-h(\vec{x})\big] = \sum_{(i_3,\ldots,i_w)} L_{i_3,\ldots,i_w}(\vec{x}) \otimes \log R_{i_3}(\vec{x}) \otimes \cdots \otimes \log R_{i_w}(\vec{x}), \quad \text{(A.26)}$$

where $L_{i_3,\ldots,i_w}$ is a linear combination of weight-two multiple polylogarithms, and $R_{i_3},\ldots,R_{i_w}$ are rational functions. Since the weight-two object $L_{i_3,\ldots,i_w}$ must be proportional to ζ_2, we write $L_{i_3,\ldots,i_w} = k\,\zeta_2$ for some rational number k. This constant of proportionality can be determined by numerical evaluation at some specific values for $\vec{x}$ using GiNaC [145] and running the PSLQ algorithm [146, 147]. The hereby obtained transcendental constant $k\,\zeta_2$

[1] The weight of $I(a_0;a_1,\ldots,a_n;a_{n+1})$ is equal to its number of indices, n. Likewise, a pair of weights (p,q) is attributed to a tensor $T_p \otimes T_q$ where the weights of T_p and T_q are p and q, respectively.

multiplies a polylogarithmic function, whose symbol is given by $R_{i_3} \otimes \cdots \otimes R_{i_w}$, arising from the tail of the arguments of eq. (A.26). Feeding this symbol back into the first step of this algorithm and collecting the resulting multiple polylogarithms from the output of step two produces a function $h_2(\vec{x})$ in canonical form, which is to multiply the constant $k\,\zeta_2$. As a consequence we have that

$$\Delta_{2,1,\ldots,1}\left[g(\vec{x}) - h(\vec{x}) - k\,\zeta_2\,h_2(\vec{x})\right] = 0\,, \tag{A.27}$$

and we conclude that the difference $g(\vec{x}) - h(\vec{x}) - k\,\zeta_2\,h_2(\vec{x})$ is equal to terms proportional to transcendental constants of weight three and higher, which are in the kernel of $\Delta_{2,1,\ldots,1}$. Iterating this procedure with the coproducts $\Delta_{3,1,\ldots,1}$, …, $\Delta_{w-1,1}$ allows us to reconstruct the other missing constants with transcendental weight $3,\ldots,w-1$, respectively. The final output of the third step in the algorithm is thus a rewritten version of the original function in canonical form.

An illustration of this algorithm, as applied to a practical example, may be found in appendix B of ref. [4]. The algorithm has also been used to derive eqs. (4.65), (4.81), (4.85) and (4.106) in this thesis.

Appendix B

Harmonic sums

Harmonic sums arise naturally in the context of loop corrections, for example in the expansion of the Gamma function [132],

$$\Gamma(-n+\epsilon) = \frac{\Gamma(1+\epsilon)}{\epsilon}\frac{(-1)^n}{n!}\left(1+\epsilon S_1(n)+\epsilon^2 S_{1,1}(n)+\epsilon^3 S_{1,1,1}(n)+\cdots\right) . \tag{B.1}$$

This appendix collects properties of harmonic sums, which are mainly used in chapter 5.

B.1. Definitions and properties

Definition B.1. *Harmonic sums are defined recursively in the number of indices,*

$$S_{\ell_1}(n) = \sum_{i=1}^{n} \frac{\mathrm{sign}(\ell_1)^i}{i^{|\ell_1|}} , \qquad S_{\ell_1,\ell_2,\ldots,\ell_k}(n) = \sum_{i=1}^{n} \frac{\mathrm{sign}(\ell_1)^i}{i^{|\ell_1|}} S_{\ell_2,\ldots,\ell_k}(i) , \tag{B.2}$$

for non-zero integer ℓ_1. The weight is given by $w = \sum_{i=1}^{k} |\ell_i|$. At a given weight there are $2\cdot 3^{w-1}$ harmonic numbers. It is often convenient to write $S_{\vec{\ell}}(n) \equiv S_{\ell_1,\ell_2,\ldots,\ell_k}(n)$.

Harmonic sums have several useful properties. They form a quasi shuffle algebra: a product of harmonic sums that depend on the same variable n can be written as a linear combination of sums [131]. For the product of two harmonic sums with a single index,

$$S_\ell(n) S_m(n) = S_{\ell,m}(n) + S_{m,\ell}(n) - S_{\ell\oplus m}(n) , \tag{B.3}$$

where $\ell \oplus m = \mathrm{sign}(\ell)\,\mathrm{sign}(m)\big(|\ell| + |m|\big)$. Starting from this case, a formula for harmonic sums with multiple indices is constructed recursively in the number of indices.

Harmonic sums provide a basis of functions for single-scale processes in Mellin space [148]. Rational functions of n, possibly multiplied by harmonic sums, may be expressed entirely in terms of harmonic sums. Such a conversion to a basis of harmonic sums is achieved through the following algorithm.

Algorithm B.2. *Conversion to a basis of harmonic sums [132]*

1. *Make the argument of each sum equal to n, by recursively applying*

$$S_{\vec{\ell}}(n+a) = \begin{cases} S_{\vec{\ell}}(n+a-1) + \text{sign}(\ell_1)^{n+a} \dfrac{S_{\ell_2,\ldots,\ell_k}(n+a)}{(n+a)^{|\ell_1|}} & \text{for } a > 0 \,, \\ S_{\vec{\ell}}(n+a+1) - \text{sign}(\ell_1)^{n+a+1} \dfrac{S_{\ell_2,\ldots,\ell_k}(n+a+1)}{(n+a+1)^{|\ell_1|}} & \text{for } a < 0 \,, \end{cases} \tag{B.4}$$

2. *Write products of sums as linear combination of single sums by means of the shuffle algebra, see eq.* (B.3).

3. *Synchronize the argument of each sum with the denominator (if present) by iteratively applying partial fractioning and*

$$\frac{S_{\vec{\ell}}(n+a)}{(n+b)^p} = \begin{cases} \dfrac{S_{\vec{\ell}}(n+a-1)}{(n+b)^p} + \text{sign}(\ell_1)^{n+a} \dfrac{S_{\ell_2,\ldots,\ell_k}(n+a)}{(n+b)^p\,(n+a)^{|\ell_1|}} & \text{for } a > b \,, \\ \dfrac{S_{\vec{\ell}}(n+a+1)}{(n+b)^p} - \text{sign}(\ell_1)^{n+a+1} \dfrac{S_{\ell_2,\ldots,\ell_k}(n+a+1)}{(n+b)^p\,(n+a+1)^{|\ell_1|}} & \text{for } a < b \,, \end{cases} \tag{B.5}$$

   for integers a, b and positive integer p.

4. *Absorb denominators into sums by applying*

$$\begin{aligned} \frac{S_{\vec{\ell}}(n+b)}{(n+b)^p} &= S_{p,\vec{\ell}}(n+b) - S_{p,\vec{\ell}}(n+b-1) \,, \\ (-1)^{n+b}\,\frac{S_{\vec{\ell}}(n+b)}{(n+b)^p} &= S_{-p,\vec{\ell}}(n+b) - S_{-p,\vec{\ell}}(n+b-1) \,, \end{aligned} \tag{B.6}$$

   for integer b and positive integer p.

5. *Write remaining fractions as differences of sums, using*

$$\begin{aligned} \frac{1}{(n+b)^p} &= S_p(n+b) - S_p(n+b-1) \,, \\ \frac{(-1)^{n+b}}{(n+b)^p} &= S_{-p}(n+b) - S_{-p}(n+b-1) \,, \end{aligned} \tag{B.7}$$

   for integer b and positive integer p.

This algorithm for conversion to a basis of harmonic sums has been used, for example, to derive eqs. (5.44), (5.73), (5.75) and (5.79) in this thesis.

For numerical implementations a different basis of functions may be more suitable. Using the algebraic relations among harmonic numbers, results may be expressed in terms of (products of) as few harmonic numbers as possible [149, 150]. For example, harmonic

numbers with any number of equal indices can be traded for harmonic numbers with a single index, using identities such as $S_{1,1}(n) = \frac{1}{2}\left(S_1(n)^2 + S_2(n)\right)$.

Harmonic sums are closely related to harmonic polylogarithms (HPLs, see eq. (A.6)). One particular connection is provided by the Mellin transform.

Definition B.3. *The Mellin transform of a function $f(x)$ is defined by*

$$\mathscr{M}_n\left[f(x)\right] = \int_0^1 \mathrm{d}x\, x^{n-1} f(x)\,. \tag{B.8}$$

In particular, the set of $2 \cdot 3^w$ Mellin transforms of weight w Harmonic Polylogarithms (HPLs) multiplied by two different integration kernels, $\frac{1}{1-x}$ and $\frac{1}{1+x}$, are in one-to-one correspondence with the set of weight $w+1$ harmonic sums. Another connection is that HPLs appear in the generating function of harmonic sums, as described in appendix B.3.

B.2. Analytic continuation of harmonic sums

The definition of harmonic numbers in eq. (B.2) only makes sense for positive integers n. However, one may also encounter harmonic numbers evaluated at non-integer values, like $S_{\vec{\ell}}(n + j\epsilon)$, see the discussion in section 5.3.5. This requires analytic continuation from the integers to the real line. One approach uses a basis of functions consisting of harmonic numbers with a single index $S_\ell(n)$ augmented with inverse Mellin transforms, both of which have a known analytic continuation [148]. A lightening review:

Consider the simplest harmonic sum $S_1(n)$. Its primary definition is

$$S_1(n) = \sum_{i=1}^{n} \frac{1}{i}\,, \tag{B.9}$$

for integer n. This function appears in the result of the Mellin transform

$$\mathscr{M}_n\left[\left(\frac{1}{1-z}\right)_+\right] = -S_1(n-1)\,. \tag{B.10}$$

Solving for $S_1(n)$ and writing out the definition of the Mellin transform, we arrive at another representation of the harmonic number, which is valid for real $n > -1$,

$$S_1(n) = \int_0^1 \mathrm{d}z\, \frac{1-z^n}{1-z}\,. \tag{B.11}$$

Using this formula we can easily shift $n \to n - j\epsilon$. Subsequently expanding in ϵ yields

$$\begin{aligned} S_1(n - j\epsilon) &= S_1(n) - \sum_{i=1}^{\infty} \frac{(-j\epsilon)^i}{i!} \int_0^1 \mathrm{d}z \, \frac{z^n \log^i z}{1-z} \\ &= S_1(n) + \sum_{i=1}^{\infty} (j\epsilon)^i \left[S_{i+1}(n) - \zeta_{i+1} \right] . \end{aligned} \tag{B.12}$$

Generalising to higher weight harmonic numbers with a single index, $S_\ell(n)$ for $\ell > 1$, is most conveniently done in terms of (derivatives of) the polygamma function,

$$S_\ell(n) = \frac{(-1)^{\ell-1}}{(\ell-1)!} \psi^{(\ell-1)}(n+1) + \zeta_\ell \, . \tag{B.13}$$

This formula provides the analytic continuation of $S_\ell(n)$ to complex argument and can be used to derive an expansion analogous to eq. (B.12), namely

$$S_\ell(n - j\epsilon) = S_\ell(n) + \sum_{i=1}^{\infty} \binom{i+\ell-1}{i} (j\epsilon)^i \left[S_{i+\ell}(n) - \zeta_{i+\ell} \right] . \tag{B.14}$$

Note that for $\ell = 1$ this formula reproduces the expansion of $S_1(n)$. For the case of a single *negative* index a similar construction is possible, using the Mellin transform of $1/(1+x)$ instead [148]. The result is rather similar,

$$S_{-\ell}(n - j\epsilon) = S_{-\ell}(n) + \sum_{i=1}^{\infty} \binom{i+\ell-1}{i} (j\epsilon)^i \left[S_{-(i+\ell)}(n) + \zeta_{i+\ell}\left(1 - \frac{1}{2^{i+\ell-1}}\right) \right] , \tag{B.15}$$

where $\ell > 1$.

Harmonic sums with multiple indices have analytic continuations in terms of inverse Mellin transforms [148]. That allows to derive ϵ-expansions of all harmonic sums, analogous to eqs. (B.12), (B.14) and (B.15). The `Mathematica` package `HarmonicSums` provides a practical implementation [131, 134, 143, 148, 151–153].

B.3. Generating function of harmonic sums

Harmonic sums can appear themselves inside another sum. For example, they are series coefficients of master integrals $\sum_{n=1}^{\infty} S_{\vec{a}}(n)\, \omega^n$ in section 5.3.4. This begs the question what such sums evaluate to. In other words, what is the generating function of harmonic sums?

The answer is that the generating function of a harmonic sum is given by a linear combinations of harmonic polylogarithms weighted by the rational function $\frac{1}{1-x}$. This section provides a motivation for this statement and collects explicit formulae for the generating function of harmonic sums up to weight two.

To start, consider HPLs with a single index. These functions are equal to classical polylogarithms, which have a well-known sum representation:

$$H_k(x) = \mathrm{Li}_k(x) = \sum_{n=1}^{\infty} \frac{x^n}{n^k} \,. \tag{B.16}$$

Writing $\frac{1}{n^k} = S_k(n) - S_k(n-1)$ and shifting n in the second term, one obtains

$$\sum_{n=1}^{\infty} S_k(n)\, x^n = \frac{\mathrm{Li}_k(x)}{1-x} = \frac{H_k(x)}{1-x} \,. \tag{B.17}$$

Thus, the generating function of $S_k(n)$ is given by the right-hand side of eq. (B.17).

The non-alternating harmonic sums (i.e. only positive indices) have a similar simple formula for the generating function,

$$G_{\vec{a}}(x) \equiv \sum_{n=1}^{\infty} S_{\vec{a}}(n)\, x^n = \frac{1}{1-x} \sum_{\vec{b}\,(\vec{a})} H_{\vec{b}}(x) \,, \tag{B.18}$$

where the sum on the right-hand side is over vectors $\vec{b}$ obtained by all possible ways of "merging" consecutive indices in $\vec{a}$. For example,

$$\sum_{n=1}^{\infty} S_{1,1,1}(n)\, x^n = \frac{H_{1,1,1}(x) + H_{2,1}(x) + H_{1,2}(x) + H_3(x)}{1-x} \,. \tag{B.19}$$

The alternating sums have the same structure, but with minus signs here and there. Explicit formulae can be obtained most easily by making an ansatz for each generating function,

$$\sum_{n=1}^{\infty} S_{\vec{a}}(n)\, x^n = \frac{1}{1-x} \sum_{i=1}^{2\cdot 3^{w-1}} c_i\, H_{\vec{b}_i}(x) \,, \tag{B.20}$$

where the weight of $\vec{a}$ is w and $\vec{b}_i$ label all index vectors of weight w, and where the unknown coefficients $c_i \in \{-1, 1\}$ are determined by equating the first $2 \cdot 3^{w-1}$ series coefficients on both sides of eq. (B.20). The complete results are, at weight one,

$$\begin{aligned} \sum_{n=1}^{\infty} S_1(n)\, x^n &= \frac{H_1(x)}{1-x} \,, \\ \sum_{n=1}^{\infty} S_{-1}(n)\, x^n &= \frac{-H_{-1}(x)}{1-x} \,. \end{aligned} \tag{B.21}$$

At weight two,

$$\begin{aligned}
\sum_{n=1}^{\infty} S_2(n)\,x^n &= \frac{H_2(x)}{1-x}\,,\\
\sum_{n=1}^{\infty} S_{-2}(n)\,x^n &= \frac{-H_{-2}(x)}{1-x}\,,\\
\sum_{n=1}^{\infty} S_{1,1}(n)\,x^n &= \frac{H_2(x)+H_{1,1}(x)}{1-x}\,,\\
\sum_{n=1}^{\infty} S_{1,-1}(n)\,x^n &= \frac{-H_{-2}(x)-H_{1,-1}(x)}{1-x}\,,\\
\sum_{n=1}^{\infty} S_{-1,1}(n)\,x^n &= \frac{-H_{-2}(x)+H_{-1,-1}(x)}{1-x}\,,\\
\sum_{n=1}^{\infty} S_{-1,-1}(n)\,x^n &= \frac{H_2(x)-H_{-1,1}(x)}{1-x}\,.
\end{aligned} \tag{B.22}$$

Formulae for higher weight are constructed along the same lines.

If the argument of the harmonic sum is shifted by an integer, then the sum should be slightly rewritten according to

$$\begin{aligned}
\sum_{n=1}^{\infty} S_{\vec{\ell}}(n+k)\,x^n &= x^{-k}\left(\sum_{n=1}^{\infty} S_{\vec{\ell}}(n)\,x^n\right) - \sum_{n=1}^{k} S_{\vec{\ell}}(n)\,x^{n-k}\,,\\
\sum_{n=1}^{\infty} S_{\vec{\ell}}(n-k)\,x^n &= x^{k}\left(\sum_{n=1}^{\infty} S_{\vec{\ell}}(n)\,x^n\right) + \sum_{n=1}^{k} S_{\vec{\ell}}(n-k)\,x^n\,.
\end{aligned} \tag{B.23}$$

where $k > 0$. Here, the infinite sums on the right-hand sides can be written in terms of HPLs, while the finite sums are to be evaluated explicitly term-by-term.

S

SAMENVATTING

Dit proefschrift gaat over de wereld van de allerkleinste deeltjes en beschrijft mijn promotieonderzoek over het rekenen aan hun gedrag. Hier geef ik een beknopte en enigszins vereenvoudigde uitleg over dat onderzoek. Dat begint met een geschiedenis van het kijken naar heel kleine dingen.

De zeventiende-eeuwse textielhandelaar Antoni van Leeuwenhoek was een pionier op het gebied van de microscopie. Om de kwaliteit van zijn textiel te inspecteren vervaardigde hij sterke vergrootglazen. Daar werd hij zó goed in dat hij veruit de beste in de wereld maakte, in staat tot honderden malen vergroting. Uit nieuwsgierigheid richtte hij zijn microscoop ook op andere voorwerpen behalve textiel. Zodoende ontdekte hij een wereld van organismen die niet met het blote oog zichtbaar zijn.

Als wij in gedachte nogmaals een factor duizend vergroten, dan zien we menselijk DNA van dichtbij en beginnen we zelfs individuele watermoleculen (H_2O) te onderscheiden. Op deze schaal, een miljoenste van een millimeter, speelt de elektromagnetische kracht een zeer belangrijke rol. Deze kracht is verantwoordelijk voor het bijeenhouden van moleculen, die zijn opgebouwd uit atomen. Water, bijvoorbeeld, bestaat uit twee waterstof atomen (H) en één zuurstof atoom (O). Zo zijn er nog ruim honderd andere soorten atomen bekend.

Atomen bestaan op hun beurt uit een kern gemaakt van protonen en neutronen, en ver daarbuiten een wolk van elektronen. Voor de elektronen stopt hier de reductie, het zijn *elementaire deeltjes*. De protonen en neutronen in de atoomkern hebben wél een substructuur, gemaakt van quarks die bijeengehouden worden door de sterke kernkracht. Daarnaast is er een tweede kracht die een rol speelt in de atoomkern: de zwakke kernkracht. Alle fenomenen die gerelateerd zijn aan radioactiviteit worden veroorzaakt door deze kracht. Hierbij worden neutrino's geproduceerd, elementaire deeltjes die maar amper wisselwerking vertonen; ze gaan met gemak dwars door de aarde heen. Kort samengevat kunnen we dus stellen dat quarks, elektronen en neutrino's tezamen alle zichtbare materie vormen.

In de loop van de vorige eeuw zijn er echter nog meer elementaire deeltjes ontdekt, veelal dankzij experimenten met deeltjesversnellers. We hebben drie 'families' gevonden van de materiedeeltjes (quarks, elektron en neutrino), die onderling slechts in massa verschillen.

De zwaardere families zijn echter instabiel en komen slechts kortstondig voor, wat verklaart waarom ze geen normale materie vormen. Een tweede klasse van elementaire deeltjes zijn de krachtdragers: het foton voor de elektromagnetische kracht, de gluonen voor de sterke kernkracht en de W en Z bosonen voor de zwakke kernkracht. Materiedeeltjes ondervinden krachten door het uitwisselen van deze krachtdragers. Het Higgs boson, een deeltje dat wordt geassocieerd met een mechanisme voor het genereren van massa, vormt een aparte categorie. Het bestaan ervan is in 2012 op spectaculaire wijze experimenteel vastgesteld. Dit zijn alle bekende elementaire deeltjes.

Deze wereld van elementaire deeltjes wordt nauwkeurig beschreven door een bepaalde wiskundige kwantumveldentheorie, die bekend staat als het standaardmodel van de deeltjesfysica. Om deze theorie te toetsen, om de juistheid te verifiëren dan wel falsificeren, worden voorspellingen gedaan voor meetbare grootheden (zoals werkzame doorsneden) bij botsingen in deeltjesversnellers. Een belangrijke stap hierbij is het berekenen van de *verstrooiingsamplitude*, een wiskundige functie die alle mogelijke interacties tijdens een botsingsproces beschrijft. Hierbij maken we gebruik van *storingstheorie*, een benaderingsmethode waarbij de verstrooiingsamplitude geschreven word als een eerste schatting plus een reeks van almaar kleinere correctietermen. Met steeds meer van deze correcties wordt de uitkomst steeds nauwkeuriger, maar wordt tegelijkertijd de berekening ook ontzettend veel ingewikkelder. Het is dus een heuse uitdaging om hogere-orde correctietermen te berekenen.

Mijn onderzoek gaat over dergelijke correcties aan verstrooiingsamplitudes. De specifieke interacties in deze bijdragen worden getekend met behulp van Feynman diagrammen. Deze diagrammen bevatten interne en externe lijnen die deeltjes voorstellen. De externe deeltjes zijn fysisch (meetbaar) en moeten voldoen aan Einstein's relatie tussen energie, impuls en massa. We zeggen dat de impuls van een fysische deeltje op de massaschil ligt, of kortweg *on-shell*. Interne deeltjes hoeven echter niet te voldoen aan deze relatie en zijn in het algemeen off-shell. Sterker nog, de kwantummechanica schrijft voor dat alle mogelijke configuraties van interne deeltjes op toepasselijke wijze bij elkaar opgeteld moeten worden. Zo dragen de interne deeltjes sterk bij aan de complexiteit van verstrooiingsamplitudes.

In sommige gevallen is het daarom zinvol om een vereenvoudiging te bedenken voor deze verstrooiingsamplitudes, bijvoorbeeld door een bepaalde restrictie op te leggen. Het doel hiervan kan zijn om een redelijke benadering van het antwoord te geven of om specifieke informatie uit de verstrooiingsamplitude te verkrijgen. Een voor de hand liggende restrictie is om (sommige) interne deeltjes op de massaschil te leggen, waardoor het fysische deeltjes worden. Hierdoor hebben de interne deeltjes minder vrijheidsgraden en kan hun bijdrage aan een verstrooiingsamplitude gemakkelijker worden bepaald. Deze restrictie is, in feite, de rode draad door dit proefschrift. Het wordt op gevarieerde wijze gebruikt in de verschillende hoofdstukken, zoals ik nu duidelijk zal maken.

Zoals gezegd zijn veel elementaire deeltjes instabiel en vervallen snel in een aantal lichtere deeltjes. Dit komt regelmatig voor in hoge-energie deeltjesbotsingen. Instabiele deeltjes

hebben de vrijheid om van de massaschil af te wijken met een hoeveelheid die gekarakteriseerd word door de verval breedte. Een instabiel deeltje wiens verval breedte klein is (in vergelijking met zijn massa), zal typisch vlakbij de massaschil zitten. We noemen zulke deeltjes *smalle resonanties*. Een aantal zeer interessante deeltjes, waaronder het Higgs boson, zijn zulke smalle resonanties. Door in een berekening aan te nemen dat smalle resonanties exact op de massaschil liggen, worden ze effectief beschouwd als stabiele deeltjes. Deze *smalle-breedte benadering* splitst een verstrooiingsproces in twee deelprocessen, productie en verval van een smalle resonantie, die elk eenvoudiger te berekenen zijn dan het volledige oorspronkelijke proces dat beiden bevat.

Het derde hoofdstuk van dit proefschrift beschrijft een implementatie van de smalle-breedte benadering in het computerprogramma MADSPIN voor het simuleren van het verval van smalle resonanties. De naam van dit programma staat voor twee belangrijke aspecten. "MAD" verwijst naar MADGRAPH, de oorspronkelijke naam van het grotere raamwerk waar het is ingebouwd. Een kenmerk van dit raamwerk is de *algemene toepasbaarheid* op een grote klasse van verstrooiingsprocessen en daarom is MADSPIN ook zó gemaakt dat het algemeen toepasbaar is op alle smalle resonanties. "SPIN" refereert naar *spin correlaties*, die een verstrengeling veroorzaken tussen deeltjes die uit deeltjesbotsingen tevoorschijn komen. Dit meetbare fenomeen moet uiteraard worden meegenomen in theoretische voorspellingen. Het programma MADSPIN combineert de smalle-breedte benadering met informatie over spin correlaties afkomstig uit de voorgaande term in de storingsreeks. Dat dit een uitstekende beschrijving van spin correlaties geeft, heb ik gedemonstreerd met een voorbeeld.

In zekere zin vormt dit programma een sluitstuk in de verzameling van theoretische voorspellingen waarbij de eerste-orde correctie in storingstheorie wordt meegenomen. Dit niveau van precisie is in veel gevallen echter niet voldoende, zeker niet naarmate er steeds nauwkeurigere experimentele metingen worden verricht. De rest van dit proefschrift begeeft zich daarom op het gebied van hogere-orde correcties, een onderzoeksterrein waar nog veel te doen is.

Eén van de aspecten van hogere-orde correcties waar ik onderzoek naar gedaan heb is *infrarode straling*. Deze straling van fotonen of gluonen met zeer lange golflengte kan tot gevolg hebben dat Feynman diagrammen 'oneindig' opleveren. In de juiste som van diagrammen vallen oneindigheden tegen elkaar weg, maar blijft er wel een spoor achter van de infrarode straling. Dit effect kan bestudeerd worden met behulp van versimpelde Feynman diagrammen, zogenaamde *eikonale diagrammen*. Het eenvoudigste type eikonale diagrammen beschrijft de uitwisseling van infrarode straling tussen twee energetische deeltjes. In een bepaalde limiet wordt de interactiepotentiaal tussen de twee deeltjes gegeven door het imaginaire deel van de eikonale diagrammen. Ik heb een berekeningsmethode ontwikkeld, waarbij de on-shell restrictie wordt opgelegd aan de infrarode straling, om deze informatie op een heel directe manier uit eikonale diagrammen te verkrijgen. Dit heb ik vervolgens ook met succes toegepast op zeer ingewikkelde diagrammen uit tweede- en derde-orde correctietermen in storingstheorie.

Het laatste deel van dit proefschrift richt zich op de berekening van specifieke tweede-orde correcties in storingstheorie. Daarbij maakte ik gebruik van *unitariteit*, de stelling dat de kansen op alle mogelijke uitkomsten van een deeltjesbotsing samen moeten optellen tot één. Deze logische vereiste is ingebouwd in de theorie in de vorm van een unitaire verstrooiingsmatrix. Een goede vraag is: valt deze eigenschap uit te buiten om berekeningen te vereenvoudigen? Voor sommige botsingsprocessen blijkt dit inderdaad het geval te zijn, met name wanneer de uitkomst weinig specifiek gedefinieerd is. Dit valt uit te leggen met de volgende analogie. Gooi twee dobbelstenen. Wat is de kans dat de twee dobbelstenen een verschillend aantal ogen tonen? Dit kan op veel manieren: ⚀⚁, ⚀⚂, ⚀⚃, ⚀⚄, ⚀⚅, ⚁⚂, enzovoorts. Gemakkelijker is het in dit geval om te kijken naar de complementaire gebeurtenis dat de twee dobbelstenen hetzelfde aantal ogen tonen, ⚀⚀, ⚁⚁ tot ⚅⚅, en de kans daarop af te trekken van één. Een klassiek voorbeeld hiervan vinden we in de deeltjesfysica bij de diep-inelastische verstrooiing van een elektron aan een proton. De kans op dit proces is te verkrijgen uit het 'complementaire' proces waarbij de deeltjes onafgebogen uit de botsing tevoorschijn komen. Dit is wiskundig omschreven in de *optische stelling*, welke in het verleden is gebruikt om op efficiënte wijze de totale werkzame doorsnede van diep-inelastische verstrooiing te bepalen.

In hoofdstuk 5 bestudeer ik een ander type proces: de botsing tussen twee protonen, waarbij een lepton-antilepton deeltjespaar wordt geproduceerd (het Drell-Yan proces). Dit proces is interessant omdat het vaak voorkomt in huidige deeltjesversnellers. Maar er is een probleem als we hier unitariteit willen gebruiken: in dit proces is de optische stelling niet van toepassing. Dit komt doordat de eindtoestand van het proces vrij specifiek is (er zijn ook andere eindtoestanden mogelijk), waardoor het 'complementaire' proces ook niet eenvoudig is. Door algemenere technieken te ontwikkelen, heb ik toch weten te inventariseren welke bijdragen van één afgetrokken moeten worden. Daarmee heb ik laten zien dat het mogelijk is om ook van het Drell-Yan proces de werkzame doorsnede te bepalen via unitariteit; dit belooft dat nog ingewikkeldere correcties wellicht berekenbaar worden.

Zoals Antoni van Leeuwenhoek door zijn microscoop een wereld van onzichtbaar kleine dingen ontdekte, zo heb ik op deze onderwerpen gefocust om nog weer een stukje kennis bloot te leggen op het gebied van de elementaire deeltjesfysica.

S

SUMMARY

This thesis is about the world of the smallest particles and describes my research on calculating their behaviour. Here I present a brief and somewhat simplified explanation of that research. It starts with a history of looking at very small things.

The seventeenth-century textile trader Antoni van Leeuwenhoek was a pioneer in the area of microscopy. In order to inspect the quality of his textiles he manufactured strong magnifying glasses. He became such a skilled craftsman that he was able to make the best in the world by far, capable of hundredfold magnification. Out of curiosity he started to point his microscopes at other objects besides textiles. This led him to discover a world of organisms that cannot be seen with the naked eye.

If we imagine to continue magnifying another one thousand times, we would see human DNA in close-up and we would start to distinguish individual water molecules (H_2O). At this scale, one millionth of a millimetre, the electromagnetic force plays a very important role. This force is responsible for holding together molecules, which are built up of atoms. Water, for instance, consists of two hydrogen atoms (H) and one oxygen atom (O). Over a hundred types of atoms like these are known to exist.

Atoms consist in turn of a nucleus made up of protons and neutrons, and far away around it a cloud of electrons. For the electrons the reduction stops here, they are *elementary particles*. The protons and neutrons in the atomic nucleus do however have a substructure, made of quarks bound together by the strong nuclear force. Moreover, there is a second force that plays a role in the nucleus: the weak nuclear force. All phenomena related to radioactivity are caused by this force. Such processes create neutrinos, elementary particles which hardly undergo any interactions; they easily travel through the entire earth. In summary we can therefore say that quarks, electrons and neutrinos together form all visible matter.

Yet more elementary particles have been discovered during the last century, mostly in particle accelerator experiments. We have found three 'families' of the matter particles (quarks, electron and neutrino), which differ from each other by their mass. The heavier families are unstable and short-lived, which explains why they do not make up ordinary matter. A

second class of elementary particles consists of force carriers: the photon for the electromagnetic force, the gluons for the strong nuclear force and the W and Z bosons for the weak nuclear force. Matter particles experience forces by interchanging these force carriers. The Higgs boson, a particle associated to the mechanism that generates mass, forms a separate category. Its existence was spectacularly experimentally established in 2012. These are all known elementary particles.

This world of elementary particles is accurately described by a certain quantum field theory, known as the Standard Model of particle physics. In order to test this theory, either to verify or falsify its correctness, predictions are made for measurable quantities (such as cross sections) in collisions at particle accelerators. An important step in this process is the calculation of a *scattering amplitude*, a mathematical function which describes all possible interactions during a collision process. For this task we make use of *perturbation theory*, an approximation method which expresses the scattering amplitude as a first estimate plus a series of increasingly smaller corrections. Including ever more of these corrections makes the outcome ever more accurate, but at the same time the calculation becomes tremendously more complicated. So it is a real challenge to compute higher-order corrections in perturbation theory.

My research is concerned with such corrections to scattering amplitudes. The specific interactions in these contributions are drawn by means of Feynman diagrams. These diagrams contain internal and external lines which represent particles. The external particles are physical (measurable) and must satisfy Einstein's relationship between energy, momentum and mass. We say that the momentum of a physical particle is on the mass-shell, or *on-shell* for short. Internal particles, on the other hand, do not need to satisfy this relationship and are generally off-shell. In fact, quantum mechanics prescribes that all possible configurations of internal particles are to be added up appropriately. In this way, the internal particles contribute much to the complexity of scattering amplitudes.

In some cases it is therefore useful to come up with a simplification for these scattering amplitudes, for example by imposing a certain restriction. The purpose of this can be to obtain a reasonable approximation of the answer or to extract some specific information from the scattering amplitude. An obvious restriction could be to place (some of the) internal particles on their mass shell, so that they become physical particles. This limits the degrees of freedom of the internal particles, so that their contribution to a scattering amplitude can be more readily determined. This restriction is, in fact, the common thread in this thesis. It is used in various ways in the different chapters, as I will now clarify.

As mentioned, many elementary particles are unstable and decay rapidly into lighter particles. This occurs frequently in high-energy particle collisions. Unstable particles have the freedom to be off their mass shell by an amount characterized by the decay width. An unstable particle whose decay width is small (in comparison to its mass), will typically be close to the mass shell. We call such particles *narrow resonances*. A number of very interesting particles, including the Higgs boson, are such narrow resonances. By assuming in a calculation that narrow resonances are exactly on-shell, they are effectively treated as

stable particles. This *narrow-width approximation* splits a scattering process into two subprocesses, production and decay of a narrow resonance, each of which can be computed more easily than the original process featuring both.

The third chapter of this thesis describes an implementation of the narrow-width approximation in the computerprogram MADSPIN for simulating the decay of narrow resonances. The name of this program points to two of its features. "MAD" is adopted from MADGRAPH, the original name of the framework into which the program is embedded. A key feature of this framework is its *general applicability* to a large class of scattering processes. Likewise, MADSPIN was created in such a way that it generally applies to all narrow resonances. Secondly, "SPIN" refers to *spin correlations*, which cause entanglement among particles that emerge from particle collisions. This measurable phenomenon should be accounted for in theoretical predictions. The program MADSPIN combines the narrow-width approximation with spin correlation information from the previous term in the perturbative series. This yields an excellent description of spin correlations, as I demonstrated with an example.

In a certain sense this program forms a concluding piece in the set of theoretical predictions that include first-order corrections in perturbation theory. This level of precision may however not be sufficient in the presence of increasingly accurate experimental measurements. The remainder of this thesis ventures therefore into the territory of higher-order corrections, where much is still to be done.

One aspect of higher-order corrections that I have investigated is *infrared radiation*. This radiation of photons or gluons with extremely large wavelength can have the consequence that Feynman diagrams yield the outcome 'infinity'. In a correct sum of diagrams the infinities cancel, but a trace of the infrared radiation is still left behind. This effect can be studied with the help of simplified Feynman diagrams, so-called *eikonal diagrams*. The simplest type of eikonal diagram describes the exchange of infrared radiation between two energetic particles. In a certain limit, the interaction potential for those two particles is given by the imaginary part of the eikonal diagram. I have developed a method of calculation that imposes the on-shell restriction on the infrared radiation, in order to extract this information from eikonal diagrams in a very direct way. Subsequently I successfully applied this method to highly complex diagrams from second- and third-order corrections in perturbation theory.

The last part of this thesis focuses on the calculation of specific second-order corrections in perturbation theory. For this I made use of *unitarity*, the statement that the probabilities for all possible outcomes of a particle collision must add up to one. This sensible requirement is built into the theory in the form of a unitary scattering matrix. A good question is: can this property be exploited to simplify calculations? For some processes this turns out to be the case, especially if the outcome of the process is not very specific. This can be explained with the following analogy. Roll two dice. What is the probability of obtaining two different numbers? This can happen in many ways: ⚀⚁, ⚀⚂, ⚀⚃, ⚀⚄, ⚀⚅, ⚁⚂, and so on. It is actually easier in this case to consider the complementary event in which both dice display the same numbers, ⚀⚀, ⚁⚁ up to ⚅⚅, and to subtract the probability

of this event from one. A classical example of this idea is found in particle physics in the case of deep-inelastic scattering of an electron off a proton. The probability of this process to occur can be extracted from the 'complementary' process in which the colliding particles emerge undeflected from the collision. This is described mathematically in the *optical theorem*, which has been used in the past to determine the total cross section of deep-inelastic scattering in an efficient way.

In chapter 5, I study a different type of process: a collision between two protons that produces a lepton-antilepton particle pair (the Drell-Yan process). This process is interesting because it occurs frequently in current particle accelerators. But there is a problem if we wish to use unitarity here: in this reaction the optical theorem is not valid. The reason is that the final state of the process is quite specific (other final states are also possible), which means that the 'complementary' process is not simple either. By developing general techniques, I have nevertheless identified which contributions are to be subtracted from one. Thereby I have demonstrated that it is in fact possible to determine the cross section of the Drell-Yan process via unitarity; this promises that even more complicated corrections may become calculable.

Like Antoni van Leeuwenhoek discovered a world of invisibly small things through his microscope, I have focused on these selected topics to uncover yet another bit of knowledge in the field of elementary particle physics.

A

Acknowledgements

First of all I would like to thank my supervisor Eric Laenen for giving me the opportunity to carry out a PhD research over the past four years. It has been a great pleasure to be working together and I have learned countless things from you in the process. I gratefully acknowledge all your guidance and support, which have been essential to the completion of this thesis.

Secondly, I wish to thank my collaborators. Thanks to Pierre Artoisenet, Rikkert Frederix and Olivier Mattelaer for their work on MadSpin, and in particular to Pierre for teaching me the ropes during his time as a postdoc at Nikhef. I am also grateful to Stefano Frixione and Tom Melia for an inspiring collaboration and for their hospitality during my visits to CERN. Although our work did not made it into this thesis, I sincerely hope that we will publish it in the future. Many thanks to Domenico Bonocore for the pleasant way of working together and for sharing many years as fellow PhD students and officemates. A special thanks to my copromotor Kasper Larsen for the stimulating collaboration that we started at Nikhef and for the valued coaching with great attention to details. Finally, I thank Einan Gardi and Andries Waelkens at the Higgs Centre for Theoretical Physics in Edinburgh for their hospitality and for giving me the opportunity to learn more about webs, and thanks to Andries for visiting Amsterdam in return to work together.

I would also like to thank all the members of the reading committee, Jan de Boer, Stefano Frixione, Paul de Jong, Ronald Kleiss, Bernard Nienhuis and Jos Vermaseren, for evaluating this manuscript. In addition, I thank Bernard for monitoring the progress of my research as second supervisor and Jos for insightful discussions.

Then there are many people who were not directly involved in this thesis, but who did contribute to a positive work environment during the past four years. Thanks to the people at the Institute of Physics at the University of Amsterdam, in particular the various people with whom I had the pleasure to teach and the staff at the secretariat for their help. A special thanks to all the staff, postdocs and students in the Nikhef theory group for the stimulating atmosphere and for all the pleasant conversations during lunch and coffee breaks. In particular I would like to mention my officemates over the past four years, Rob, Kristof, Domenico, Satish and Jorinde, as well as the neighbours, Sander, Maarten,

Giuseppe, Andrea and Sabrina, whose door was always open. Thanks for sharing the daily life as a PhD student.

Finally, I want to extend a more personal ‘thank you’ to some people. Thanks to my friends from Almere, Utrecht and Amsterdam. In particular Philip, Matthijs, Jeroen, Hessel, Gerben, Daniëlle, Hannah, Ineke and Benjamin, thanks for meeting up and sharing times in our lives. Thanks to my housemates for their good company. Eline, Bert, Andrei, Elisa and Jacopo, I have really enjoyed living together with you.

Ik ben mijn familie zeer dankbaar voor hun liefde en steun. Eline, Bert en Annelies, ik kan enorm genieten van jullie als broer en zussen. Papa en mama, bedankt voor jullie onophoudelijke liefde en voor alles wat jullie voor mij gedaan hebben. Jullie hebben deze prestatie mogelijk gemaakt.

I was fortunate to share the last year with one person in particular. Elisa, thank you so much for believing in me and for providing encouragement and distraction when I needed them. Thank you for painting the beautiful cover of this book and for continuing to add colour to my life.

Robbert Rietkerk

G

Glossary

aMC@NLO Automated Monte Carlo at Next-to-Leading Order 18, 24–26
BRIDGE Branching Ratio Inquiry/Decay Generated Events 18
BSM Beyond the Standard Model (physics) 1, 3, 13, 26
DIS Deep Inelastic Scattering 67, 68, 70, 72, 83
FIRE Feynman Integral Reduction 89
GiNaC Ginac is Not a CAS 106
GSL GNU Scientific Library 65
HERA Hadron Electron RingAnlage 70
HERWIG Hadron Emission Reactions With Interfering Gluons 18, 22, 24–26
HPL Harmonic Polylogarithm 111, 113, 114
IBP Integration-By-Parts identity 3, 76–79, 85, 87
LHC Large Hadron Collider 1, 13, 21, 24, 26, 67, 70
LiteRed Loop Integral Reduction 89
$\mathscr{M}_n$ Mellin transform 70, 73, 88, 93, 111
MC@NLO Monte Carlo at Next-to-Leading Order 18
MCFM Monte Carlo for Femtobarn processes 22, 24, 98
MPL Multiple Polylogarithm 101–103
MSSM Minimal Supersymmetric Standard Model 16
NLO Next-to-Leading Order 2, 14, 24–26
NNLO Next-to-Next-to-Leading Order 2, 3, 67, 99
POWHEG Positive Weight Hardest Emission Generator 18
PSLQ Partial sum of Squares LQ matrix factorization 106
PV Principal Value 38, 41, 46, 47, 51, 57, 63
QCD Quantum Chromodynamics 2, 3, 14, 17, 24–26, 30, 36, 67, 68, 71, 99
QED Quantum Electrodynamics 27, 34
SecDec Sector Decomposition 91

B

Bibliography

[1] P. Artoisenet, R. Frederix, O. Mattelaer, and R. Rietkerk, JHEP **03**, 015 (2013), arXiv:1212.3460.

[2] LHC Higgs Cross Section Working Group, J. R. Andersen *et al.*, (2013), arXiv:1307.1347.

[3] E. Laenen, K. J. Larsen, and R. Rietkerk, Phys. Rev. Lett. **114**, 181602 (2015), arXiv:1410.5681.

[4] E. Laenen, K. J. Larsen, and R. Rietkerk, JHEP **07**, 083 (2015), arXiv:1505.02555.

[5] D. Bonocore, E. Laenen, and R. Rietkerk, JHEP **05**, 079 (2016), arXiv:1603.05252.

[6] R. Eden, P. Landshoff, D. Olive, and J. Polkinghorne, *The Analytic S-Matrix* (Cambridge University Press, 1966).

[7] L. D. Landau, Nucl. Phys. **13**, 181 (1959).

[8] R. E. Cutkosky, J. Math. Phys. **1**, 429 (1960).

[9] M. J. G. Veltman, *Intermediate particles in S-Matrix theory and calculation of higher order effects in the production of intermediate vector bosons*, PhD thesis, Utrecht U., 1963.

[10] G. P. Korchemsky and A. V. Radyushkin, Nucl. Phys. **B283**, 342 (1987).

[11] A. Denner and J.-N. Lang, Eur. Phys. J. **C75**, 377 (2015), arXiv:1406.6280.

[12] W. Beenakker and A. Denner, Nucl. Phys. **B338**, 349 (1990).

[13] Z. Bern, L. J. Dixon, D. C. Dunbar, and D. A. Kosower, Nucl. Phys. **B425**, 217 (1994), arXiv:hep-ph/9403226.

[14] Z. Bern, L. J. Dixon, D. C. Dunbar, and D. A. Kosower, Nucl. Phys. **B435**, 59 (1995), arXiv:hep-ph/9409265.

[15] R. Britto, F. Cachazo, and B. Feng, Nucl. Phys. **B725**, 275 (2005), arXiv:hep-th/0412103.

[16] R. Britto, F. Cachazo, and B. Feng, Nucl. Phys. **B715**, 499 (2005), arXiv:hep-th/0412308.

[17] R. Britto, F. Cachazo, B. Feng, and E. Witten, Phys. Rev. Lett. **94**, 181602 (2005), arXiv:hep-th/0501052.

[18] W. T. Giele, Z. Kunszt, and K. Melnikov, JHEP **04**, 049 (2008), arXiv:0801.2237.

[19] C. F. Berger *et al.*, Phys. Rev. **D78**, 036003 (2008), arXiv:0803.4180.

[20] K. G. Chetyrkin and F. V. Tkachov, Nucl. Phys. **B192**, 159 (1981).

[21] S. Laporta, Int. J. Mod. Phys. **A15**, 5087 (2000), arXiv:hep-ph/0102033.

[22] C. Anastasiou and K. Melnikov, Nucl. Phys. **B646**, 220 (2002), arXiv:hep-ph/0207004.

[23] T. Gehrmann and E. Remiddi, Nucl. Phys. **B580**, 485 (2000), arXiv:hep-ph/9912329.

[24] J. M. Henn, J. Phys. **A48**, 153001 (2015), arXiv:1412.2296.

[25] K. J. Larsen and Y. Zhang, Phys. Rev. **D93**, 041701 (2016), arXiv:1511.01071.

[26] S. D. Drell, Electrodynamic Interactions, in *Proc. of the Int. Conf. on High Energy Physics, 13th, Berkeley, 1966. Berkeley, Univ. of Calif. Press, 1967. p. 85-99*, pp. 85–99, 1966.

[27] J. Alwall *et al.*, JHEP **07**, 079 (2014), arXiv:1405.0301.

[28] G. J. van Oldenborgh, (1993), arXiv:hep-ph/9311223.

[29] E. N. Argyres *et al.*, Phys. Lett. **B358**, 339 (1995), arXiv:hep-ph/9507216.

[30] S. Dittmaier, Standard Model Theory, in *27th Rencontres de Blois on Particle Physics and Cosmology Blois, France, May 31-June 5, 2015*, 2015, arXiv:1509.06261.

[31] B. C. Allanach *et al.*, Eur. Phys. J. **C25**, 113 (2002), arXiv:hep-ph/0202233.

[32] Particle Data Group, K. A. Olive *et al.*, Chin. Phys. **C38**, 090001 (2014).

[33] P. Falgari, F. Giannuzzi, P. Mellor, and A. Signer, Phys. Rev. **D83**, 094013 (2011), arXiv:1102.5267.

[34] A. S. Papanastasiou, R. Frederix, S. Frixione, V. Hirschi, and F. Maltoni, Phys. Lett. **B726**, 223 (2013), arXiv:1305.7088.

[35] G. Heinrich, A. Maier, R. Nisius, J. Schlenk, and J. Winter, JHEP **06**, 158 (2014), arXiv:1312.6659.

[36] V. del Duca and E. Laenen, Int. J. Mod. Phys. **A30**, 1530063 (2015), arXiv:1510.06690.

[37] G. Mahlon and S. J. Parke, Phys. Rev. **D81**, 074024 (2010), arXiv:1001.3422.

[38] A. Brandenburg, Z. G. Si, and P. Uwer, Phys. Lett. **B539**, 235 (2002), arXiv:hep-ph/0205023.

[39] K. Melnikov and M. Schulze, JHEP **08**, 049 (2009), arXiv:0907.3090.

[40] ATLAS, G. Aad *et al.*, Phys. Lett. **B716**, 1 (2012), arXiv:1207.7214.

[41] P. Nath *et al.*, Nucl. Phys. Proc. Suppl. **200-202**, 185 (2010), arXiv:1001.2693.

[42] S. Frixione, E. Laenen, P. Motylinski, and B. R. Webber, JHEP **04**, 081 (2007), arXiv:hep-ph/0702198.

[43] S. Frixione and B. R. Webber, JHEP **06**, 029 (2002), arXiv:hep-ph/0204244.

[44] S. Frixione, E. Laenen, P. Motylinski, and B. R. Webber, JHEP **03**, 092 (2006), arXiv:hep-ph/0512250.

[45] S. Frixione, P. Nason, and G. Ridolfi, JHEP **09**, 126 (2007), arXiv:0707.3088.

[46] S. Alioli, P. Nason, C. Oleari, and E. Re, JHEP **09**, 111 (2009), arXiv:0907.4076, [Erratum: JHEP02,011(2010)].

[47] S. Alioli, P. Nason, C. Oleari, and E. Re, JHEP **06**, 043 (2010), arXiv:1002.2581.

[48] S. Hoeche, F. Krauss, M. Schonherr, and F. Siegert, JHEP **09**, 049 (2012), arXiv:1111.1220.

[49] SM MC Working Group, SM and NLO MULTILEG Working Group, J. Alcaraz Maestre *et al.*, The SM and NLO Multileg and SM MC Working Groups: Summary Report, in *Proceedings, 7th Les Houches Workshop on Physics at TeV Colliders*, pp. 1–220, 2012, arXiv:1203.6803.

[50] R. Frederix *et al.*, JHEP **02**, 048 (2012), arXiv:1110.5502.

[51] C. Degrande *et al.*, Comput. Phys. Commun. **183**, 1201 (2012), arXiv:1108.2040.

[52] P. de Aquino, W. Link, F. Maltoni, O. Mattelaer, and T. Stelzer, Comput. Phys. Commun. **183**, 2254 (2012), arXiv:1108.2041.

[53] P. Meade and M. Reece, (2007), arXiv:hep-ph/0703031.

[54] T. Sjostrand, S. Mrenna, and P. Z. Skands, JHEP **05**, 026 (2006), arXiv:hep-ph/0603175.

[55] T. Sjostrand, S. Mrenna, and P. Z. Skands, Comput. Phys. Commun. **178**, 852 (2008), arXiv:0710.3820.

[56] G. Corcella *et al.*, JHEP **01**, 010 (2001), arXiv:hep-ph/0011363.

[57] F. Maltoni and T. Stelzer, JHEP **02**, 027 (2003), arXiv:hep-ph/0208156.

[58] J. M. Campbell, R. K. Ellis, and F. Tramontano, Phys. Rev. **D70**, 094012 (2004), arXiv:hep-ph/0408158.

[59] J. M. Campbell and F. Tramontano, Nucl. Phys. **B726**, 109 (2005), arXiv:hep-ph/0506289.

[60] S. Badger, J. M. Campbell, and R. K. Ellis, JHEP **03**, 027 (2011), arXiv:1011.6647.

[61] J. M. Campbell, R. Frederix, F. Maltoni, and F. Tramontano, Phys. Rev. Lett. **102**, 182003 (2009), arXiv:0903.0005.

[62] A. D. Martin, W. J. Stirling, R. S. Thorne, and G. Watt, Eur. Phys. J. **C63**, 189 (2009), arXiv:0901.0002.

[63] A. D. Martin, W. J. Stirling, R. S. Thorne, and G. Watt, Eur. Phys. J. **C70**, 51 (2010), arXiv:1007.2624.

[64] R. Frederix, E. Re, and P. Torrielli, JHEP **09**, 130 (2012), arXiv:1207.5391.

[65] M. Cacciari, G. P. Salam, and G. Soyez, JHEP **04**, 063 (2008), arXiv:0802.1189.

[66] W. Bernreuther, A. Brandenburg, Z. G. Si, and P. Uwer, Nucl. Phys. **B690**, 81 (2004), arXiv:hep-ph/0403035.

[67] G. Mahlon and S. J. Parke, Phys. Rev. **D55**, 7249 (1997), arXiv:hep-ph/9611367.

[68] R. Frederix *et al.*, Phys. Lett. **B701**, 427 (2011), arXiv:1104.5613.

[69] M. V. Garzelli, A. Kardos, C. G. Papadopoulos, and Z. Trocsanyi, Europhys. Lett. **96**, 11001 (2011), arXiv:1108.0387.

[70] S. Dittmaier *et al.*, (2012), arXiv:1201.3084.

[71] T. Becher and M. Neubert, JHEP **06**, 081 (2009), arXiv:0903.1126, [Erratum: JHEP11,024(2013)].

[72] S. G. Naculich, H. Nastase, and H. J. Schnitzer, JHEP **04**, 114 (2013), arXiv:1301.2234.

[73] J. G. M. Gatheral, Phys. Lett. **B133**, 90 (1983).

[74] J. Frenkel and J. C. Taylor, Nucl. Phys. **B246**, 231 (1984).

[75] E. Gardi, J. M. Smillie, and C. D. White, JHEP **06**, 088 (2013), arXiv:1304.7040.

[76] Z. Bern, L. J. Dixon, and V. A. Smirnov, Phys. Rev. **D72**, 085001 (2005), arXiv:hep-th/0505205.

[77] L. J. Dixon, L. Magnea, and G. F. Sterman, JHEP **08**, 022 (2008), arXiv:0805.3515.

[78] G. P. Korchemsky and A. V. Radyushkin, Phys. Lett. **B171**, 459 (1986).

[79] J. R. Forshaw, A. Kyrieleis, and M. H. Seymour, JHEP **08**, 059 (2006), arXiv:hep-ph/0604094.

[80] J. R. Forshaw, A. Kyrieleis, and M. H. Seymour, JHEP **09**, 128 (2008), arXiv:0808.1269.

[81] G. P. Korchemsky and G. Marchesini, Nucl. Phys. **B406**, 225 (1993), arXiv:hep-ph/9210281.

[82] E. Gardi, JHEP **02**, 053 (2005), arXiv:hep-ph/0501257.

[83] S. Catani, D. de Florian, and G. Rodrigo, JHEP **07**, 026 (2012), arXiv:1112.4405.

[84] J. R. Forshaw, M. H. Seymour, and A. Siodmok, JHEP **11**, 066 (2012), arXiv:1206.6363.

[85] E. Laenen, G. Stavenga, and C. D. White, JHEP **03**, 054 (2009), arXiv:0811.2067.

[86] C. D. White, J. Phys. **G43**, 033002 (2016), arXiv:1507.02167.

[87] A. Grozin, J. M. Henn, G. P. Korchemsky, and P. Marquard, Phys. Rev. Lett. **114**, 062006 (2015), arXiv:1409.0023.

[88] A. Grozin, J. M. Henn, G. P. Korchemsky, and P. Marquard, JHEP **01**, 140 (2016), arXiv:1510.07803.

[89] J. M. Henn, A. V. Smirnov, V. A. Smirnov, and M. Steinhauser, JHEP **05**, 066 (2016), arXiv:1604.03126.

[90] S. M. Aybat, L. J. Dixon, and G. F. Sterman, Phys. Rev. Lett. **97**, 072001 (2006), arXiv:hep-ph/0606254.

[91] S. M. Aybat, L. J. Dixon, and G. F. Sterman, Phys. Rev. **D74**, 074004 (2006), arXiv:hep-ph/0607309.

[92] T. Becher and M. Neubert, Phys. Rev. **D79**, 125004 (2009), arXiv:0904.1021, [Erratum: Phys. Rev.D80,109901(2009)].

[93] A. Ferroglia, M. Neubert, B. D. Pecjak, and L. L. Yang, Phys. Rev. Lett. **103**, 201601 (2009), arXiv:0907.4791.

[94] A. Ferroglia, M. Neubert, B. D. Pecjak, and L. L. Yang, JHEP **11**, 062 (2009), arXiv:0908.3676.

[95] N. Kidonakis, Phys. Rev. Lett. **102**, 232003 (2009), arXiv:0903.2561.

[96] A. Mitov, G. F. Sterman, and I. Sung, Phys. Rev. **D82**, 034020 (2010), arXiv:1005.4646.

[97] E. Gardi, JHEP **04**, 044 (2014), arXiv:1310.5268.

[98] G. Falcioni, E. Gardi, M. Harley, L. Magnea, and C. D. White, JHEP **10**, 10 (2014), arXiv:1407.3477.

[99] O. Almelid, C. Duhr, and E. Gardi, (2015), arXiv:1507.00047.

[100] E. Gardi, J. M. Smillie, and C. D. White, JHEP **09**, 114 (2011), arXiv:1108.1357.

[101] G. F. Sterman, *An Introduction to quantum field theory* (Cambridge University Press, 1993).

[102] D. R. Yennie, S. C. Frautschi, and H. Suura, Annals Phys. **13**, 379 (1961).

[103] Y.-T. Chien, M. D. Schwartz, D. Simmons-Duffin, and I. W. Stewart, Phys. Rev. **D85**, 045010 (2012), arXiv:1109.6010.

[104] D. Correa, J. Henn, J. Maldacena, and A. Sever, JHEP **05**, 098 (2012), arXiv:1203.1019.

[105] D. Correa, J. Maldacena, and A. Sever, JHEP **08**, 134 (2012), arXiv:1203.1913.

[106] M. Beneke and V. M. Braun, Nucl. Phys. **B454**, 253 (1995), arXiv:hep-ph/9506452.

[107] Y. Schroder, Phys. Lett. **B447**, 321 (1999), arXiv:hep-ph/9812205.

[108] J. C. Collins, D. E. Soper, and G. F. Sterman, Phys. Lett. **B134**, 263 (1984).

[109] A. B. Goncharov, Duke Math. J. **128**, 209 (2005), arXiv:math/0208144.

[110] A. B. Goncharov, M. Spradlin, C. Vergu, and A. Volovich, Phys. Rev. Lett. **105**, 151605 (2010), arXiv:1006.5703.

[111] F. Brown, (2011), arXiv:1102.1310.

[112] C. Duhr, H. Gangl, and J. R. Rhodes, JHEP **10**, 075 (2012), arXiv:1110.0458.

[113] C. Duhr, JHEP **08**, 043 (2012), arXiv:1203.0454.

[114] C. Anastasiou, C. Duhr, F. Dulat, and B. Mistlberger, JHEP **07**, 003 (2013), arXiv:1302.4379.

[115] D. Maitre, Comput. Phys. Commun. **174**, 222 (2006), arXiv:hep-ph/0507152.

[116] D. Maitre, Comput. Phys. Commun. **183**, 846 (2012), arXiv:hep-ph/0703052.

[117] E. Gardi, E. Laenen, G. Stavenga, and C. D. White, JHEP **11**, 155 (2010), arXiv:1008.0098.

[118] A. Mitov, G. Sterman, and I. Sung, Phys. Rev. **D82**, 096010 (2010), arXiv:1008.0099.

[119] E. Gardi and C. D. White, JHEP **03**, 079 (2011), arXiv:1102.0756.

[120] M. Dukes, E. Gardi, E. Steingrimsson, and C. D. White, J. Comb. Theory Ser. **A120**, 1012 (2013), arXiv:1301.6576.

[121] M. Dukes, E. Gardi, H. McAslan, D. J. Scott, and C. D. White, JHEP **01**, 024 (2014), arXiv:1310.3127.

[122] A. Mitov, G. F. Sterman, and I. Sung, Phys. Rev. **D79**, 094015 (2009), arXiv:0903.3241.

[123] M. Galassi *et al.*, *Gnu Scientific Library Reference Manual*, 3rd ed. (Network Theory Ltd, 2009).

[124] S. Moch and J. A. M. Vermaseren, Nucl. Phys. **B573**, 853 (2000), arXiv:hep-ph/9912355.

[125] S. Moch, J. A. M. Vermaseren, and A. Vogt, Nucl. Phys. **B688**, 101 (2004), arXiv:hep-ph/0403192.

[126] A. Vogt, S. Moch, and J. A. M. Vermaseren, Nucl. Phys. **B691**, 129 (2004), arXiv:hep-ph/0404111.

[127] J. A. M. Vermaseren, A. Vogt, and S. Moch, Nucl. Phys. **B724**, 3 (2005), arXiv:hep-ph/0504242.

[128] Deutsche Elektronen-Synchrotron DESY, HERA - Particle physics experiments H1, ZEUS and HERMES, `http://www.desy.de/research/facilities__projects/hera/index_eng.html`, 2015, Accessed on 2016-04-18.

[129] A. V. Smirnov and A. V. Petukhov, Lett. Math. Phys. **97**, 37 (2011), arXiv:1004.4199.

[130] R. N. Lee and A. A. Pomeransky, JHEP **11**, 165 (2013), arXiv:1308.6676.

[131] J. A. M. Vermaseren, Int. J. Mod. Phys. **A14**, 2037 (1999), arXiv:hep-ph/9806280.

[132] J. A. M. Vermaseren and S. Moch, Nucl. Phys. Proc. Suppl. **89**, 131 (2000), arXiv:hep-ph/0004235.

[133] M. Höschele, J. Hoff, A. Pak, M. Steinhauser, and T. Ueda, Comput. Phys. Commun. **185**, 528 (2014), arXiv:1307.6925.

[134] J. Ablinger, J. Blumlein, and C. Schneider, J. Math. Phys. **52**, 102301 (2011), arXiv:1105.6063.

[135] R. N. Lee, (2012), arXiv:1212.2685.

[136] R. N. Lee, J. Phys. Conf. Ser. **523**, 012059 (2014), arXiv:1310.1145.

[137] A. V. Smirnov, JHEP **10**, 107 (2008), arXiv:0807.3243.

[138] A. V. Smirnov and V. A. Smirnov, Comput. Phys. Commun. **184**, 2820 (2013), arXiv:1302.5885.

[139] J. Carter and G. Heinrich, Comput. Phys. Commun. **182**, 1566 (2011), arXiv:1011.5493.

[140] S. Borowka, J. Carter, and G. Heinrich, Comput. Phys. Commun. **184**, 396 (2013), arXiv:1204.4152.

[141] S. Borowka *et al.*, Comput. Phys. Commun. **196**, 470 (2015), arXiv:1502.06595.

[142] A. Pak, M. Rogal, and M. Steinhauser, JHEP **09**, 088 (2011), arXiv:1107.3391.

[143] E. Remiddi and J. A. M. Vermaseren, Int. J. Mod. Phys. **A15**, 725 (2000), arXiv:hep-ph/9905237.

[144] A. B. Goncharov, (2009), arXiv:0908.2238.

[145] C. W. Bauer, A. Frink, and R. Kreckel, J. Symb. Comput. **33**, 1 (2000), arXiv:cs/0004015.

[146] H. R. P. Ferguson and D. H. Bailey, RNR Techn. Rept. **RNR-91-032**, 01 (1992).

[147] H. R. P. Ferguson, D. H. Bailey, and S. Arno, Math. Comput. **68**, 351 (1999).

[148] J. Blumlein, Comput. Phys. Commun. **180**, 2218 (2009), arXiv:0901.3106.

[149] J. Blumlein, Comput. Phys. Commun. **159**, 19 (2004), arXiv:hep-ph/0311046.

[150] J. Blumlein and V. Ravindran, Nucl. Phys. **B716**, 128 (2005), arXiv:hep-ph/0501178.

[151] J. Ablinger, *A Computer Algebra Toolbox for Harmonic Sums Related to Particle Physics*, PhD thesis, Linz U., 2009, arXiv:1011.1176.

[152] J. Ablinger, *Computer Algebra Algorithms for Special Functions in Particle Physics*, PhD thesis, Linz U., 2012-04, arXiv:1305.0687.

[153] J. Ablinger, J. Blümlein, and C. Schneider, J. Math. Phys. **54**, 082301 (2013), arXiv:1302.0378.